# Multiresponsive Synthetic Cells, Precise Protein Micropatterns and Streptavidin-Biotin Conjugates Using the Interaction Between $Ni^{2+}$-NTA and His-tagged Proteins

Dissertation

Zur Erlangung des Grades

**Doktor der Naturwissenschaften**

Chemie, Pharmazie, Geographie und Geowissenschaften (FB 09)

der Johannes Gutenberg-Universität Mainz


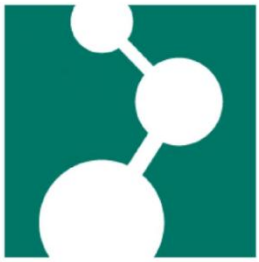

vorgelegt von

**Dongdong Xu**

geboren in Henan, P.R. China

Mainz, 2020

## Affidavit

I hereby declare that I wrote the dissertation submitted without any unauthorized external assistance and used only sources acknowledged in the work. All textual passages which are appropriated verbatim or paraphrased from published and unpublished texts as well as all information obtained from oral sources are duly indicated and listed in accordance with bibliographical rules. In carrying out this research, I complied with the rules of standard scientific practice as formulated in the statutes of Johannes Gutenberg-University Mainz to insure standard scientific practice.

(Place, Date) (Signature)

## Publications

1. **Xu, D.**; Bartelt, S. M.; Rasoulinejad, S.; Chen, F.; Wegner, S. V., Green light lithography: a general strategy to create active protein and cell micropatterns. *Materials Horizons* **2019**, *6*, 1222-1229.

2. Chen, F.; Ricken, J.; **Xu, D.**; Wegner, S. V., Bacterial Photolithography: Patterning Escherichia coli Biofilms with High Spatial Control Using Photocleavable Adhesion Molecules. *Advanced Biosystems* **2019**, *3*, 1800269.

3. **Xu, D.**; Wegner, S. V., Multifunctional streptavidin-biotin conjugates with precise stoichiometries. *Chemical Science*, **2020**, *11*, 4422-4429.

4. **Xu, D.**; Ricken, J.; Wegner, S. V., Turning Cell Adhesions ON or OFF with High Spatiotemporal Precision using the Green Light Responsive Protein CarH. *Chemistry- A European Journal*, **2020**, 26, 9859-9863.

5. **Xu, D.**; Kleineberg, C.; Vidakovic´-Koch, T.; Wegner, S. V., Multistimuli sensing adhesion unit for the self-positioning of minimal synthetic cells. *Small*, **2020**, *16*, 2002440.

6. **Xu, D.**; Heck, A. J.; Kuan, S. L.; Weil, T.; Wegner, S. V., Precise tetrafunctional streptavidin bioconjugates towards multifaceted drug delivery systems. *Chemical Communications*, **2020**, *56*, 9858-9861.

## Contents

## Abstract

The binding of polyhistidine tags (His-tags) in proteins to $Ni^{2+}$-NTA complexes is widely used in proteins purification, biofunctionalization of surfaces and protein modification. The small size of the tag, the mild conditions of the interaction (neutral pH and in the presence of salts) as well as reversibility in the presence of chelators and lowered pH allow preserving protein activity. In this thesis, these advantageous properties of the interaction between His-tags and $Ni^{2+}$-NTA complexes were used to produce multiresponsive minimal synthetic cells, precise protein micropatterns and stoichiometrically well-defined streptavidin-biotin conjugates.

Minimal synthetic cells are cell-like compartments, which have been assembled from molecular building blocks and mimic certain functions of living cells. In chapter 2, a minimal synthetic cell which combines a multistimuli sensitive adhesion unit with an energy conversion module is developed, such that it can adhere to places that have the right environmental parameters for its ATP production. The multistimuli sensitive adhesion unit can sense environmental stimuli including light, pH, oxidative stress and the presence of metal ions and can regulate the adhesion of the synthetic cell to a substrate in response to these stimuli following a chemically coded logic. The adhesion unit is composed of the light and redox responsive protein interaction of iLID and Nano as well as the pH sensitive and metal ion mediated binding of protein His-tags to $Ni^{2+}$-NTA complexes. The multistimuli responsive adhesion unit allows synthetic cells to self-position themselves in places under blue light illumination and no oxidative stress, with neutral pH and the presence of metal ions and carry out their light to ATP conversion function. Introducing such multiresponsive self-positioning module to synthetic cell is an important step towards their autonomy and transferable to other types synthetic cells.

The precise micropatterns provide structural and functional advantages in vast technological applications as well as fundamental research. In chapter 3, I developed a method of surface patterning proteins and cells with high spatiotemporal control using green light. A layer-by-layer (LbL) protein film with a green light cleavable protein, CarH, in the first layer is produced based on $Ni^{2+}$-NTA-His-tag interaction. This enables the remote release of proteins in the upper layers by exposing the film to green light with 1 μm spatial and 10 s temporal resolution. The use of green light and the specific protein interactions overcome the current limitations of UV-light and unspecific protein immobilization, which can lead to protein

denaturation. Green light lithography is successfully used to produce complex patterns of different functional His-tagged proteins including fluorescent proteins as well as the cell adhesion protein fibronectin.

In chapter 4, as a further step, two approaches for regulating cell adhesions in space and time with high precision have been developed based on the photocleavable CarH and the cell adhesion peptide, RGD. In the first design, which is call GREEN-ON, a protein layer of CarH was used to mask RGD, which is exposed upon green light illumination. In the second design, GREEN-OFF, the RGD sequence was integrated into the CarH protein and the protein CarH-RGD was used in the research of cell adhesion. Both designs allow for photoregulation and open new possibilities to investigate the dynamical regulation of cell adhesions.

Streptavidin-biotin conjugates with precise stoichiometries are powerful for the study of molecular biology, drug delivery and biotechnology. In chapter 5, I developed an approach to form monofunctional streptavidin conjugates with precise stoichiometries and number of open binding pockets. This method relies on an iminobiotin-polyhistidine tag, which allows separating streptavidin conjugates with different numbers of tags on a $Ni^{2+}$-NTA column, and later reopening binding pockets at lowered pH to introduce a second functionality. Pure fluorescently labelled mono-, di- and trivalent streptavidin-biotin conjugates prepared in this way were used for imaging biotinylated cell surface molecules with controlled clustering. Moreover, these conjugates were functionalized with a second biotinylated molecule, folic acid-biotin, to investigate the importance of multivalent binding in targeted delivery of cells.

Building on this chemistry, I prepared stoichiometrically precise tetrafunctional streptavidin conjugates in chapter 6. An exemplary streptavidin conjugate with exactly one fluorescent label, one cell targeting group, one cell penetrating peptide and one drug demonstrates how each functionality contributed to overall efficacy of the drug. Such precise tetrafunctional streptavidin conjugates opens the door for combinatorial multifunctional libraries based on the well-established biotin-streptavidin interaction.

In summary, the interaction between $Ni^{2+}$-NTA and His-tagged proteins is a reliable chemistry, which can be applied in many contexts as shown here in the design of stimuli-responsive synthetic cells, precise protein micropatterns and streptavidin-biotin conjugates. Our work provides a potential approach for the study of chemical biology, synthetic biology and cell biology.

## Zusammenfassung

Die Bindung von Polyhistidin-Tags (His-Tags) in Proteinen an $Ni^{2+}$-NTA-Komplexe wird häufig bei der Proteinreinigung, Biofunktionalisierung von Oberflächen und Proteinmodifikation eingesetzt. Die geringe Größe des Tags, die milden Bedingungen der Wechselwirkung (neutraler pH-Wert und in Gegenwart von Salzen) sowie die Reversibilität in Gegenwart von Chelatoren und der verringerte pH-Wert ermöglichen die Erhaltung der Proteinaktivität. In dieser Arbeit wurden diese vorteilhaften Eigenschaften der Wechselwirkung zwischen His-Tags und $Ni^{2+}$-NTA-Komplexen verwendet, um multiresponsive minimale synthetische Zellen, präzise Proteinmikromuster und stöchiometrisch gut definierte Streptavidin-Biotin-Konjugate herzustellen

Minimale synthetische Zellen sind zellähnliche Kompartimente, die aus molekularen Bausteinen zusammengesetzt werden und bestimmte Funktionen lebender Zellen nachahmen. In Kapitel 2 wird eine minimale synthetische Zelle entwickelt, die eine multistimuli-empfindliche Adhäsionseinheit mit einem Energieumwandlungsmodul kombiniert, so dass sie an Orten haften kann, die die richtigen Umgebungsparameter für ihre ATP-Produktion aufweisen. Die multistimuli-empfindliche Adhäsionseinheit kann Umweltreize wie Licht, pH-Wert, oxidativen Stress und das Vorhandensein von Metallionen erfassen und die Adhäsion der synthetischen Zelle an ein Substrat als Reaktion auf diese Reize nach einer chemisch codierten Logik regulieren. Die Adhäsionseinheit besteht aus der auf Licht und Redox-reagierenden Proteinwechselwirkung von iLID und Nano sowie der pH-sensitiven und Metallionen-vermittelten Bindung von Protein-His-Tags an $Ni^{2+}$-NTA-Komplexe. Die auf Multistimuli ansprechende Adhäsionseinheit ermöglicht es synthetischen Zellen, sich an Orten unter Blaulichtbeleuchtung und ohne oxidativen Stress mit neutralem pH-Wert und Vorhandensein von Metallionen selbst zu positionieren und ihre Licht-ATP-Umwandlungsfunktion auszuführen. Die Einführung eines solchen multiresponsiven Selbstpositionierungsmoduls in synthetische Zellen ist ein wichtiger Schritt in Richtung ihrer Autonomie und auf andere Arten synthetischer Zellen übertragbar.

Die präzisen Mikromuster bieten strukturelle und funktionelle Vorteile in großen technologischen Anwendungen sowie in der Grundlagenforschung. In Kapitel 3 entwickelte ich eine Methode zur Oberflächenstrukturierung von Proteinen und Zellen mit hoher räumlich-zeitlicher Kontrolle unter Verwendung von grünem Licht. Ein Schicht-für-Schicht (LbL)-Proteinfilm mit einem durch grünes Licht spaltbaren Protein, CarH, in der ersten

Schicht wird basierend auf der $Ni^{2+}$-NTA-His-Tag-Wechselwirkung hergestellt. Dies ermöglicht die Fernfreisetzung von Proteinen in den oberen Schichten, indem der Film grünem Licht mit einer räumlichen Auflösung von 1 µm und einer zeitlichen Auflösung von 10 s ausgesetzt wird. Die Verwendung von grünem Licht und die spezifischen Proteinwechselwirkungen überwinden die derzeitigen Einschränkungen von UV-Licht und unspezifischer Proteinimmobilisierung, die zur Denaturierung von Proteinen führen können. Die Grünlichtlithographie wird erfolgreich verwendet, um komplexe Muster verschiedener funktioneller His-markierter Proteine zu erzeugen.

In Kapitel 4 wurden als weiterer Schritt zwei Ansätze zur hochpräzisen Regulierung von Zelladhäsionen in Raum und Zeit entwickelt, die auf dem photospaltbaren CarH und dem Zelladhäsionspeptid RGD basieren. In dem ersten Design, das als GREEN-ON bezeichnet wird, wurde eine Proteinschicht aus CarH verwendet, um RGD zu maskieren, die bei Beleuchtung mit grünem Licht belichtet wird. Im zweiten Design, GREEN-OFF, wurde die RGD-Sequenz in das CarH integriert und das Protein CarH-RGD wurde zur Erforschung der Zelladhäsion verwendet. Beide Designs ermöglichen eine Photoregulation und eröffnen neue Möglichkeiten zur Untersuchung der dynamischen Regulation von Zelladhäsionen.

Streptavidin-Biotin-Konjugate mit präzisen Stöchiometrien eignen sich hervorragend für das Studium der Molekularbiologie, Arzneimittelabgabe und Biotechnologie. In Kapitel 5 entwickelte ich einen Ansatz zur Bildung monofunktioneller Streptavidin-Konjugate mit präzisen Stöchiometrien und der Anzahl offener Bindungstaschen. Dieses Verfahren beruht auf einer Iminobiotin-Polyhistidin-Markierung, die es ermöglicht, Streptavidin-Konjugate mit unterschiedlicher Anzahl von Markierungen auf einer $Ni^{2+}$-NTA-Säule abzutrennen und später Bindungstaschen bei gesenktem pH wieder zu öffnen, um eine zweite Funktionalität einzuführen. Reine fluoreszenzmarkierte mono-, di- und dreiwertige Streptavidin-Biotin-Konjugate, die auf diese Weise hergestellt wurden, wurden zur Abbildung biotinylierter Zelloberflächenmoleküle mit kontrollierter Clusterbildung verwendet. Darüber hinaus wurden diese Konjugate mit einem zweiten biotinylierten Molekül, Folsäure-Biotin, funktionalisiert, um die Bedeutung der multivalenten Bindung für die gezielte Abgabe von Zellen zu untersuchen.

Aufbauend auf dieser Chemie habe ich in Kapitel 6 stöchiometrisch präzise tetrafunktionelle Streptavidin-Konjugate hergestellt. Ein beispielhaftes Streptavidin-Konjugat mit genau einer fluoreszierenden Markierung, einer Zellzielgruppe, einem zellpenetrierenden Peptid und

einem Arzneimittel zeigt, wie jede Funktionalität zur Gesamtwirksamkeit des Arzneimittels beitrug. Solche präzisen tetrafunktionellen Streptavidin-Konjugate öffnen die Tür für kombinatorische multifunktionale Bibliotheken, die auf der gut etablierten Biotin-Streptavidin-Wechselwirkung basieren.

Zusammenfassend lässt sich sagen, dass die Wechselwirkung zwischen $Ni^{2+}$-NTA und His-markierten Proteinen eine zuverlässige Chemie, die in vielen Zusammenhängen angewendet werden kann, wie hier beim Design von auf Reize ansprechenden synthetischen Zellen, präzisen Proteinmikromustern und Streptavidin-Biotin-Konjugaten gezeigt wird. Unsere Arbeit bietet einen möglichen Ansatz für das Studium der chemischen Biologie, synthetischen Biologie und Zellbiologie.

# Chapter 1. Introduction

## 1.1 Synthetic cells

The rapidly growing molecular understanding of cell biology, is enabled by *in vitro* studies with reduced complexity. Yet, their translation to *in vivo* scenario is not always granted. On the other hand, the inherent complexity of cells bares an immense challenge for understanding cells in their entirety *in vitro*. Even in the simplest living cells, many life processes are still difficult to study due to their inherent complexity and the ambiguity gained over the course of evolution.[1-3] Therefore, the term minimal synthetic cell is proposed to create a well-defined and controlled minimal functioning unit that can perform one or many functions of biological cells.[1, 4]

Synthetic cells are usually bound by biomimetic or polymeric membranes, which enclose active materials such as genes, vaccines, hormones, proteins, drugs and peptides.[5] They are similar in size to natural cells, which can be a few to a couple hundred micrometers and based on liposomes,[6-8] polymersomes,[9-11] microcapsules,[12-13] and a number of other particles. Through modular synthesis from well characterized functional molecular entities, parts, and modules, those synthetic cells can be used to mimic some life processes, like energy supply, metabolism, cell growth, replication and division, signaling and motility, which are very important for the proliferation of living cells.[14] The ultimate goal is to construct a basic living unit, which is as powerful as living cells, entirely from non-living components. In the coming sections, two important cellular functions that are of relevance to the thesis; stimuli responsiveness and energy conversion will be considered.

### 1.1.1 Stimuli responsive synthetic cells

Living cells have the ability to sense different environmental signals, which allows them to react and position themselves accordingly in order to support their survival. Introducing analogous capabilities to the synthetic cells is an important step forward in their autonomy. Thus, in minimal synthetic cells different triggers such as temperature,[15-16] pH,[17-21] metal ions (e.g. $Mg^{2+}$,[22-23] $Mn^{2+}$,[24] and $Ca^{2+}$[25]), redox potential,[26-28] chemicals (e.g. oleic anhydride,[29] theophylline,[30] clay montmorillonite[31]) and light[32-34] have been used to regulate their functions. For instance, a temperature responsive bio-orthogonally proteinosome membrane has been assembled by using bovine serum albumin (BSA) and poly(N-isopropylacrylamide-co-methacrylic acid) (PNIPAM-co-MAA). The adhesion of these densely packed

proteinosomes under different environment produces membrane-caged or uncaged prototissue spheroids that are typically 40-100 μm in size and consist of 10-30 semipermeable protein-polymer microcapsules. The prototissue spheroids are capable of housing proteinosome-encapsulated enzyme cascade reactions, and show enhanced volume contractions compared with caged assemblies of unbound non-bio-orthogonal proteinosomes or individual proteinosomes when heated above 35 °C.[16] Another example is a pH controlled dynamically protein-ligand interactions in giant unilamellar vesicle (GUV). GUVs are used as a cell mimicking platform where the semipermeable nature of the lipid membrane allows small molecules to passively diffuse into the vesicle lumen and trigger a response inside. An alcohol dehydrogenase was employed to increase or decrease the interior pH upon conversion of two different small-molecule substrates, thereby modulating the pH-sensitive interaction between a Ni-NTA ligand on the vesicle membrane and an oligohistidine-tagged protein in the lumen. Through enzymatic conversion of the small molecule, a pH change can be induced that allows for the selectively triggered assembly and disassembly of a protein-ligand complex.[20] These designs open the door for a "smart" synthetic cell, while they represent systems that only respond to one parameter in their environment, the challenge remains to construct more "smart" synthetic cells which can sense and integrate multiple signals to perform their function, analogous to natural cells.

### 1.1.2 ATP production in minimal synthetic cells

ATP (adenosine triphosphate), which is usually synthesized in the cytosol, mitochondria or chloroplasts of living cells, is the most commonly used energy currency of cells for all organisms.[10] ATP is synthesized by ATP synthase using ADP (adenosine diphosphate) and $P_i$ (inorganic phosphate) under a proton gradient across a membrane. ATP synthase is a rotary motor protein which contains a membrane spanning domain ($F_o$ subunit) and a knobby protrusion that extends into the matrix ($F_1$ subunit).[35-36] The $F_o$ subunit functions to conduct protons through the membrane by a rotational mechanism of the intramembrane subunits (rotor), resulting in a torque which is transmitted to the catalytic sites by the rotor stalk. The $F_1$ subunit is responsible for the catalytic activity driving the synthesis and hydrolysis of ATP using mechanical energy. Coupling activity between the $F_o$ and $F_1$ complexes drives proton movement toward the $F_1$ side of the membrane, resulting in the ATP synthesis.[10]

As a key feature of life, the synthesis of ATP has been implemented into minimal synthetic cells.[32-33, 37-39] For instance, the synthesis of ATP can be controlled by chemicals. Otrin and

coworkers showed that the synthesis of ATP can be performed on a hybrid containers which were prepared with natural lipid soy phosphatidylcholine (soy PC) and graft copolymer PDMS-g-PEO (poly(dimethylsiloxane)-graft-poly(ethylene oxide)) in various polymer to lipid ratios. In these compartments, the $bo_3$ oxidase, a chemical energy-driven proton pump was used to establish a proton gradient and $F_oF_1$-ATP synthase used this gradient into ATP.[40] In another examples the synthesis of ATP was driven by light. Feng and coworkers imitate the light-to-ATP conversion process occurring in the thylakoid membrane by construction of $F_oF_1$-ATPase proteoliposome-coated PSII (Photosystem II, light activation protein)-based microspheres with well-defined core/shell structures using molecular assembly. Under light illumination, PSII can split water into protons, oxygen, and electrons and can generate a proton gradient for the ATP synthase to produce ATP. Thus, in this reductionist setup an artificial equivalent of chloroplast for PSII-driven ATP synthesis was realized.[33] Similarly, also the light-driven transmembrane proton pump, bacteriorhodopsin (bR), can be reconstituted in a triblock copolymer PEtOz-PDMS-PEtOz (poly(2-ethyl-2-oxazoline)-b-poly(dimethylsiloxane)-b-poly(2-ethyl-2-oxazoline)) membrane together with $F_oF_1$-ATP synthase. In the compartment, the functionality of ATP production is driven by the light-induced build-up of a proton motive force across the membrane.[10] Furthermore, Lee and coworkers designed a switchable, light-harvesting organelle that provides both a sustainable energy source and a means of directing intravesicular reactions. Two photoconverters, PSII and proteorhodopsin (PR), were reconstituted in an organelle with ATP synthase to enable the ATP synthesis. Inside the two photoconverters, blue and red light activates electron transport chains in the PSII reaction center, whereas mainly green light initiates direct proton pumping in PR. Moreover, PR exhibits pH-dependent bidirectional proton-pumping ability. At a higher pH, both PR and PSII work in conjunction to increase the proton motive force (PMF), but at lower pH, PR changes its pumping direction, counteracting the action of PSII. Thus, ATP synthesis can be dynamically facilitated or impeded by stimulation of PSII and PR with red or green light, respectively. They then encapsulated the photosynthetic organelles in a giant vesicle to form a protocellular system and demonstrated optical control of two ATP-dependent reactions, carbon fixation and actin polymerization, with the latter altering outer vesicle morphology (**Figure 1.1**).[32]

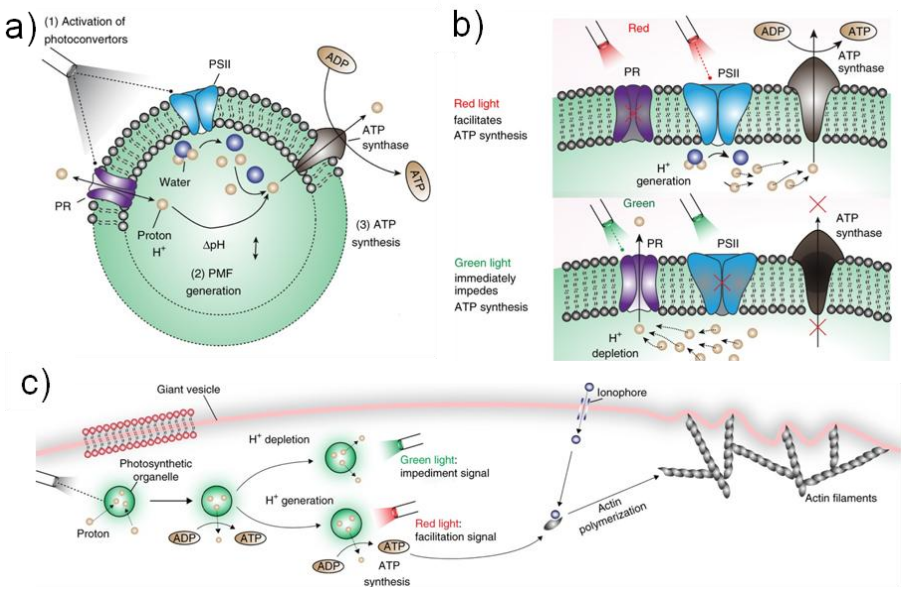


**Figure 1.1** a) Artificial organelle is prepared by the constitution of PSII (photosystem II), PR (proteorhodopsin) and ATP synthase. Upon optical stimulation, the artificial organelle synthesizes ATP by the coordinated activation of two complementary photoconverters (PSII and PR) and an ATP synthase reconstituted into the organelle's membrane. b) Activation of PSII with red light facilitates ATP synthesis by generating protons inside the organelle, while activation of PR with green light impedes ATP synthesis by depleting protons. c) After organelle energy modules are encapsulated in a giant vesicle, optical stimulation couples ATP synthesis with ATP-dependent actin polymerization and morphological change of the vesicle. Adapted with permission from reference.[32] Copyright 2018 Springer Nature.

## 1.2 Protein films

Functionalizing surfaces with protein become more and more important in the fundamental research field of biology, chemistry, material and biotechnological applications including biosensor chips,[41] enzyme reactors,[42] protein microarrays,[43] diagnostics[44] and biomedicine.[45] The biofunctionalized surface provides people a scaffold to study the functions of proteins under different environments, and for a further step, some biological process *in vivo* through an *in vitro* methodology. For example, in the field of cell biology, the interaction between cells and the extracellular matrix (ECM) is crucial for the regulation of cellular processes such as migration,[46] adhesion,[47] proliferation,[48] differentiation,[47] and apoptosis.[49] Cell adhesion proteins, such as fibronectin, vitronectin, collagen, and laminin[50] can be functionalized on a substrate, form protein films on the surface. Cells can be immobilized on the protein film without any damage and protein film, in reverse, influences and modulates cellular behavior. Ricken and coworkers integrated cell adhesion peptide RGD (arginine, glycine, aspartic acid) into the light responsive domain so that the RGD sequence is hidden in

the folded protein in the dark. Upon noninvasive light illumination, RGD is exposed for integrin binding resulting in cell adhesion and spreading.[51] This design allows one to reversibly and noninvasively control integrin-mediated cell adhesion.

### 1.2.1 Layer by layer protein films

The layer-by-layer (LbL) assembly is a prevalent method for coating substrates with functional thin films, which was initially developed by the group of Moehwald, Lvov and Decher.[52-54] Since, many LbL assembly methods have been introduced using hydrogen bonds, electrostatic interactions, sol-gel processes, step-by-step reactions, molecular recognition, stepwise stereocomplex assembly, charge-transfer, and electrochemistry to combine layers with complementary reactivities.[55-56] These methods allow for the introduction of a large variety of building blocks and functionalities into multilayer thin films with great facility. For example, electrostatic interactions, which are one of the main driving forces for LbL assembly, require merely the building blocks to be water-soluble and multi-charged species of opposite sign, such as proteins, enzymes, polyelectrolytes, oligo-charged organic compounds and colloid particles.[56] The process of the multilayer formation is in many cases simply based on electrostatic attraction and an exact positional matching of the charged groups are not required. Thus, more than one building block can be incorporated into the multilayers, and if necessary, different building blocks can be incorporated in a designed layer sequence. The electrostatic LbL assembly is usually performed in aqueous solution, such that they are conveniently fabricated an automated fashion by using a LbL deposition machines.

The powerful LbL surface coating technique has emerged in lots of applications including protein purification,[57] ultrastrong materials,[58] biomedicine,[59] drug delivery,[60-61] tissue engineering,[62-63] cell seeding,[64-67] wound healing[68-69] and customizable microreactors.[70] LbL films can be used for regulating cell-material interactions since cells are extremely sensitive to the spatial organization of the biochemical and mechanical cues of their microenvironment.[71-72] Taking advantage of the spatial control provided by the LbL films, cell-cell and cell-material interactions can be optimized towards biomedical applications such as tissue engineering, biosensors, and diagnostic devices.[59] For example, Akashi and coworkers[73] developed a LbL coating to prepare tissue like films. In this study, first a monolayer of fibroblasts was seeded on a fibronectin-functionalized cover glass, followed by the adsorption of seven fibronectin and gelatin bilayers. The preparation of this multilayer

provided an interface similar to the natural extracellular matrix to seed a second layer of cells. Following this pattern, they were able to construct four cell layers intercalated by fibronectin-gelatin bilayers with controlled thickness. Furthermore, the fibroblasts could be intercalated with umbilical vascular endothelial cells to evaluate their stability and function.[74] These results demonstrated that the LbL structure was enough to provide a protective and biomimetic environment for the cells and the great flexibility that assembling LbL films with functional proteins provides.

Multilayer assemblies of functional proteins are attractive due to the nanoscale organization of different proteins also found in natural systems and the versatile architectures to create chemical responsive biointerfaces or even biomimetic signal transfer systems. For instance, Pallarola and co-workers assemblies multiprotein LbL structure to build up a chemoresponsive bioelectrochemical interface based on multivalent supramolecular carbohydrate-lectin interactions between horseradish peroxidase (HRP), glucose oxidase (GOx) and concanavalin A (Con A) derivatives (**Figure 1.2**).[75] In this multiprotein film, the precise layering of the different proteins resulted in the effective transfer of electrons and substrates leading to the detection of glucose as an electronic signal. Likewise, enzyme-responsive LbL films have been designed and opens an avenue for developing biosensing and drug delivery systems.[59, 76-78]

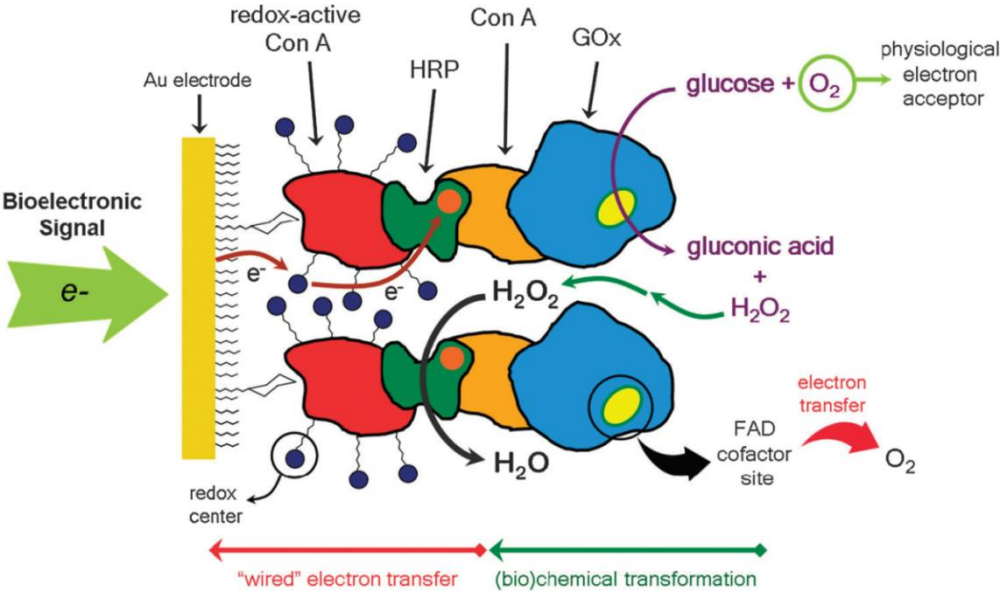


**Figure 1.2** Illustrative schematic of the glucose-responsive LbL-grown film spontaneously assembled via molecular recognition processes. The figure describes the constituting building blocks participating in the generation of the bioelectronic signal in the presence of glucose: redox-active Con A, HRP, Con A and Gox. Adapted with permission from reference.[75] Copyright 2012 The Royal Society of Chemistry.

### 1.2.2 Patterning surfaces with proteins

The patterning of surfaces with functional proteins is of relevance for many disciplines in fundamental research such as in neuronal guidance, membrane protein function, biological recognition and for technological purposes such as sensor development, photonics, organic electronics, medical applications and many more.[79-84] Especially, the patterning of cell adhesion proteins has been used to define where cells adhere on a material and to determine which specific signaling pathways are activated in the cell.[85] Such *in vitro* protein micropatterns mimic the patterns and their dynamics observed in tissues and during tissue formation *in vivo* and provide a great tool to study them.[86]

Approaches for patterning include lithography,[87-88] microfluidics,[89-90] chemical vapour deposition[91-92] and micro-contact printing.[93] For instance, microfluidics allows for the selective deposition of LbL films on surfaces at the microscale, with channel widths or diameters ranging from 50 to 800 μm.[59] On the other hand, lithography allows the preparation of features from micrometers to nanometers.[94-98] The patterning of surfaces with proteins requires very mild conditions and most of these technologies are not suitable since they require multiple steps under harsh conditions (e.g. electron beam for lithography, high temperature, nonphysiological pH) and non-biocompatible chemicals.[93, 99-101] Therefore, approaches for protein patterning with high spatial and temporal control that are scalable, cost efficient, noninvasive and tunable are still rate.

### 1.2.3 Protein patterning using photolithography

Among the above listed approaches for surface patterning, photolithography, which requires projecting a pattern of light onto a light responsive surface, is of particular interest when it comes to patterning proteins. Photolithography provides precise control of the shape and size of the patterns it creates and allows patterning a large surface cost-effectively. Many photopatterning schemes use light switchable (e.g. azobenzenes)[86-88, 102] and light cleavable (e.g. nitrobenzenes)[83-84, 103] moieties to produce light responsive surfaces.

Azobenzene groups contain two phenyl rings linked by a N=N double bond, which undergo *trans* to *cis* photoisomerization under ultraviolet (UV) light and reverse from *cis* to *trans* in dark. The light driven reversible isomerization of azobenzenes makes them excellent candidates to control the presentation of different moieties and consequently the photopatterning of liked molecules. Wang and coworkers fabricated a potoresponsive

azobenzene/silica nanoparticles film by elelctrostatic self-assembly technique. The silica nanoparticle was used to increase the roughness so that the surface wettability of film will change significantly upon UV (*trans*) and visible-light irradiation (*cis*). Results indicated that the more hydrophobic surface with *trans* form could adsorb more proteins and the less hydrophobic surface with *cis* form could only adsorb a few proteins.[87]

Nitrobenzene groups, can be photocleaved by the UV light and allow the selective removal of linked functionalities from the substrate.[104] For example, Tirrell and coworkers prepared a polymeric hydrogels including a 2-nitrophenyl group. After incubated with fluorescent labelled protein and irradiated of UV light by mask, patterns of alternating lines was prepared because of the nitrobenzene groups. This study illustrated one strategy for gaining spatial and temporal control of protein patterning *in vitro*. For a further step, they use this approach to pattern the extracellular matrix protein vitronectin, and the reversible differentiation of human mesenchymal stem cells to osteoblasts in a spatially defined manner was accomplished.[84]

However, both azobenzenes and nitrobenzenes require the use of UV light, which is damaging to biomolecules including proteins as well as cells.[105] Recently, near infrared light was used to protein photopatterning based on the simultaneous two-photon absorption.[106] Even though two-photo activation provides excellent resolution, it is time-consuming as each point needs to be illuminated sequentially. Besides, two-photon absorption requires high-intensity light, makes it only occurs at the focus of a powerful pulsed laser.[107]

An alternative for the above mentioned UV-light based methods for protein patterning is visible light photolithography. Beside the high biocompatibility, visible light photolithography is easy to implement into a conventional fluorescence microscope, versatile regarding the wavelength range and inoffensive to proteins. Towards this end, blue and red light have been used to specifically photopatterned proteins on lipid vesicles and supported lipid bilayer using photoswitchable protein pairs that respond to blue light such as iLID-Nano[108] and that respond to red light such as PhyB (phytochrome B)-PIF6 (phytochrome interacting factor).[109] It should be noted that these protein patterns were reversible in the dark and far-red light, respectively. The PhyB-PIF6 protein was further engineered to spatiotemporally target proteins onto model membranes and sequentially guide structural assembly *in vitro* from the bottom up. In this way, complex micrometer-sized protein patterns can be printed on time scales of seconds and the protein density can be precisely controlled

by protein concentration, laser power, and activation time. Moreover, when printing self-assembling proteins such as the bacterial cytoskeleton protein FtsZ, the targeted assembly into filaments and large-scale structures such as artificial rings can be accomplished. An alternative to light responsive proteins is to pattern proteins through a light-to-heat conversion using green light on a poly(N-isopropylacrylamide) (PNIPAM) layer.[110] Similarly, also in this case reversible protein patterns form and are suitable for studying protein dynamics. Yet, until now options to photopattern proteins permanently with visible light are still missing and other light responsive proteins should be discovered to prepare permanent protein patterns in this respect.

### 1.3 Light responsive proteins for optogenetic control

The term optogenetic describes photo-responsive genetically encoded proteins. The first generation optogenetics concentrated on the use of light to control neurons that have been genetically modified to express light-sensitive ion channels.[111] Over the last decade, the field of non-neuronal optogenetics has been growing, offering powerful tools to investigate intracellular processes using light.[119,120] A variety of different proteins, which respond to distinct wavelengths, covering the whole visible range of the electromagnetic spectrum,[119] provide a rich toolbox for regulating cellular processes with light as an external stimulus,[112-113] including receptor activation, gene expression, enzyme activity, protein clustering and protein localization both in mammalian and bacterial cells.[114-117] In this thesis, two photo-responsive proteins were employed: green light photocleavable protein CarH and blue light photoswitchable protein pair iLID/Nano.

#### 1.3.1 Green light photocleavable protein CarH

The protein CarH from *Thermus thermophilus* forms a tetramer in the dark when it binds to its cofactor adenosylcobalamin (AdoCbl, coenzyme $B_{12}$, $AdoB_{12}$ or vitamin $B_{12}$) and this tetramer dissociates into its monomers under green light illumination.[118-120] The analysis of the crystal structure demonstrates that the CarH tetramer is a dimer-of-dimers in the dark, where each CarH monomer has an N-terminal DNA binding domain followed by a C-terminal the light-sensing cobalamin (Cbl)-binding domain (**Figure 1.3a**).[121]

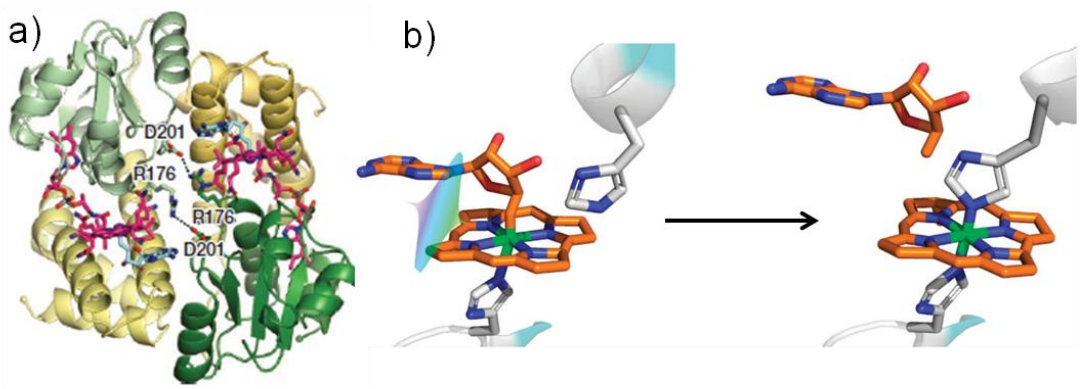


**Figure 1.3** a) CarH protomers arranged in a head-to-tail dimer, coloured by domain (helix bundle: yellow; Cbl-binding domain: green) with left protomer shown in lighter colours. Adapted with permission from reference.[121] Copyright 2015 Springer Nature. b) Proposed photochemical conversion of base-off AdoCbl in CarH to a cobalamin adduct with an active-site residue (likely either H132 or H142). Adapted with permission from reference.[122] Copyright 2015 Springer Nature.

CarH tetramer is formed when AdoCbl coordinates to a histidine (H177) in the active-site. The photoconversion of CarH involves changes at the AdoCbl centre (**Figure 1.3b**).[122-123] More specifically, a histidine residues (likely H132 or H142) in CarH above the AdoCbl replaces the adenosyl as a ligand at the cobalt center. Removal of this ligand produces a significant structural change in the protein and the photo-conversion of CarH from tetramer to monomer. The ligand exchange and the conformational switch is irreversible and the photochemical process takes place within femtoseconds to seconds.[122]

The light triggered photocleavage of CarH has been used for the optogenetic gene regulations,[120, 124-125] protein release[126] and controlled cell signals.[127] Even in the bacterium *Myxococcus xanthus* CarH down-regulates the biosynthesis of photoprotecting carotenoids.[124-125, 128] CarH has also been implemented into protein-based photoresponsive hydrogels, which are covalently polymerized into genetically encoded SpyTag-SpyCatcher hydrogels under mild physiological conditions. In these SpyTag/SpyCatcher hydrogels, AdoCbl induced assembly of CarH tetramers leads to a network formation and a hydrogel in dark. Upon green light illumination, the CarH tetramer decomposes and the hydrogel liquefies. This light dependent decomposition of the hydrogel was used to release 3T3 fibroblasts and human mesenchymal stem cells (hMSCs) in a light dependent manner without compromising cell viability.[118] Unlike other known optogenetic proteins, CarH is unique in its sensitivity to green light and fills a gap in the electromagnetic spectrum of optogenetic tools. Moreover, CarH undergoes an irreversible change upon illumination, making it a

unique optogenetic building block among the other light responsive proteins. Considering such applications of CarH, over 200 CarH-like proteins identified in various bacterial genomes are a likely source of new light responsive proteins.[122]

### 1.3.2 Blue light switchable protein pair iLID and Nano

The proteins iLID and Nano are an engineered protein pair, which bind to each other under blue light.[129-131] The improved light-inducible dimer (iLID) was engineered from a naturally occurring LOV2 domain (light-oxygen-voltage domain 2) of phototropin1 from the plant *Avena sativa* (*As*LOV2). The *As*LOV2 consists of a core per-arnt-sim (PAS) fold with an α-helix on each of the N- and C-termini. Under blue light, the cofactor flavin mononucleotide (FMN) is excited from a single into a triplet state.[123] This step enables the formation of a covalent bond between a cysteine in the LOV2 domain and the cofactor FMN.[122] The formation of this bond alters the conformation of the entire protein and results in the unwinding of the C-terminal Jα-helix.[124–126] The unfolding of the Jα-helix in iLID can be separated into a two-step process: First, the covalent bond formation of FMN to the cystein 450 (Cys450) and the breaking of the hydrogen bonds formed by glutamine 513 (Gln513) within 10 µs. Secondly, the unwinding of the Jα-helix which takes another 240 µs and makes it available for other interactions (**Figure 1.4a**).[127]

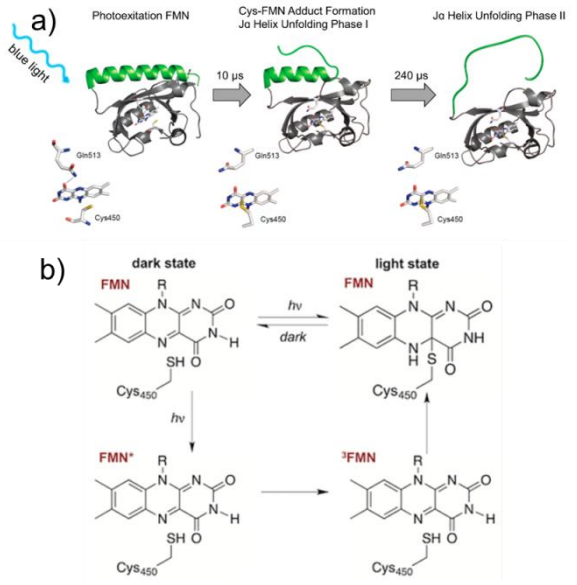


**Figure 1.4** a) Mechanism of the blue light activation of AsLOV2 domain. By excitation with blue light the cofactor FMN changed from a singlet to a triplet state and forms a covalent bind with the Cys450 of the protein. This binding leads to a conformation change and is unwinding the Jα-helix shown in green. This unfolding that allows SspB to interact with iLID. Adapted with permission from reference.[127] Copyright 2012 Elsevier. b)

Schematic depiction of the LOV domain's photocycle showing the involvement of a central cysteine residue. Adapted with permission from reference.[132] Copyright 2018 American Chemical Society.

In detail, the formation of the covalent bond between the cysteine in the LOV2 domain and the cofactor FMN can be dissected into a sequence of processes.[132-133] The absorbed light, initiates a chemical reaction during which a metastable covalent adduct is formed between a flavin cofactor and a conserved cysteine residue of the LOV2 domain. The reaction proceeds via excitation of FMN with blue light[134] to a singlet state, FMN*, that rapidly interconverts to a triplet state, $^{3}$FMN, which then reacts with the sulfur of a neighbored cysteine side chain, resulting in the "light state" of the protein (**Figure 1.4b**).[135-136]

When blue light illumination is stopped, the covalent bond between the FMN cofactor and the cysteine breaks within seconds and the Jα-helix rewinds.[125,128] It was shown that different protein domains can be fused to the end of the Jα-helix[129] and that their activity can be regulated with blue light.[129] The re-engineered version of *As*LOV2 domain, iLID, contains a naturally occurring seven amino acid peptide, SsrA, from *Escherichia coli* in its Jα-helix that can bind an adaptor protein, SspB. In the dark the SsrA peptide is hidden in the Jα-helix of *As*LOV2, and the binding of SspB is sterically hindered. Blue light irradiation (488 nm) results in the unfolding of the Jα helix and enables the binding of SspB. The binding affinity of iLID to the wild type SspB peptide, called Micro changes from 800 nM under blue light to 47 μM in the dark. A point mutation in the SspB at the arginine 73 to a glutamine, called Nano, change the binding affinity from 132 nM under blue light to 4.7 μM in the dark (36-fold change). The iLID/Nano interaction pair reverts to dark state within minutes.

iLID with its interaction partners have been used to control protein localization[137-141], activate signaling pathways[142] and transcription[143], induce cell migration[144-145] as well as to self-assemble oligomeric enzymes[146] and mimic RNA granules by forming protein hydrogels[147]. For example, iLID/Micro dimerization has been used to regulate the GTPase signaling through the translocation of guanine nucleotide exchange factors (GEFs) to the plasma membrane.[141]

### 1.4 Streptavidin-biotin interaction

Streptavidin is a tetrameric protein with a molecular weight of 52.8 kDa, purified from the bacterium *Streptomyces avidinii* and it has an extraordinarily high affinity for biotin. The dissociation constant ($K_d$) of the streptavidin biotin complex is on the order of $10^{-14}$ mol/L,[148] which makes it to be one of the strongest non-covalent interactions known in nature.

The femtomolar affinity between streptavidin and biotin is owing to a high shape complementarity between the binding pocket of streptavidin and biotin. There is an extensive network of hydrogen bonds formed to biotin when it is in the binding site (eight hydrogen bonds made to residues in the binding site, involving residues Asn23, Tyr43, Ser27, Ser45, Asn49, Ser88, Thr90 and Asp128). Besides, there are also hydrophobic interactions between the streptavidin and biotin, which means there are numerous van der Waals force-mediated contacts made to the biotin when it is in the pocket of streptavidin (**Figure 1.5**). The hydrophobic contribution is also thought to significantly account for the high affinity.[149-150]

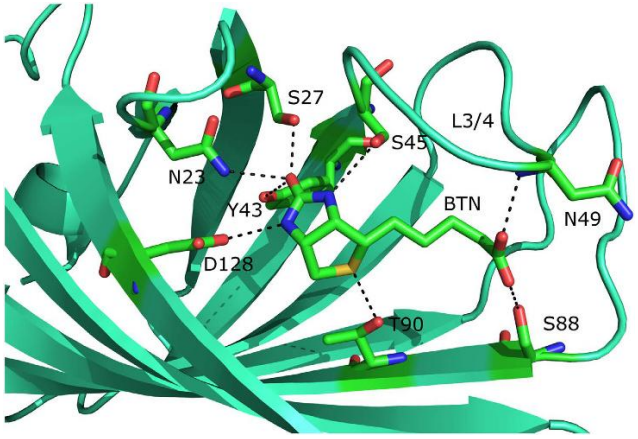


**Figure 1.5** Binding of biotin to streptavidin. The hydrogen bonds are marked as dashed lines. Adapted with permission from reference.[149] Copyright 2016 Springer Nature.

Streptavidin-biotin interaction is used extensively in molecular biology and bionanotechnology including labelling,[151-152] therapeutics, biosensing and biofunctionalization,[153-155] protein and nucleic acid detection, due to the high affinity, slow exchange rate and good specificity.[156] Nowadays, the large repertoire of biotinylated small molecules, proteins, peptides, nucleic acids and antibodies as well as materials add to the diversity of the biotin-streptavidin chemistry. Moreover, streptavidin-biotin complexes are resistance to proteolytic enzymes, detergents (e.g. SDS or Triton), denaturants (e.g. guanidinium chloride), organic solvents and extremes of temperature and pH, which can also be used for the development of artificial metalloenzymes,[157] probes,[158] protein delivery,[159] robust and highly sensitive assays.[160]

### 1.4.1 Streptavidin-biotin conjugates with precise structure

Each streptavidin tetramer has four independent biotin binding sites, which allows streptavidin to be used as a linker between a wide variety of biotinylated molecules with targeting, sensing, diagnostic and therapeutic functionalities and assembling them into one

molecule in a modular fashion. However, in some cases, the tetravalence can also be a disadvantage as it leads to statistical mixtures of conjugates when multiple biotinylated molecules are coupled to one streptavidin as well as unwanted cross-linking and aggregation. Thus, streptavidin-biotin conjugates with precise stoichiometries are highly needed.

One popular idea to solve the problem has been the design of monomeric streptavidins.[161] A tetrameric but monovalent streptavidin was been prepared by the assembly of one 'alive' subunit of wild-type streptavidin and 3 'dead' subunits of mutant streptavidin that include point mutations in the biotin binding pocket which abolish the biotin binding. The refolded streptavidin thus is monovalent and has been successfully used for cell receptor labeling without artificial cross-linking (**Figure 1.6**).[161-162]

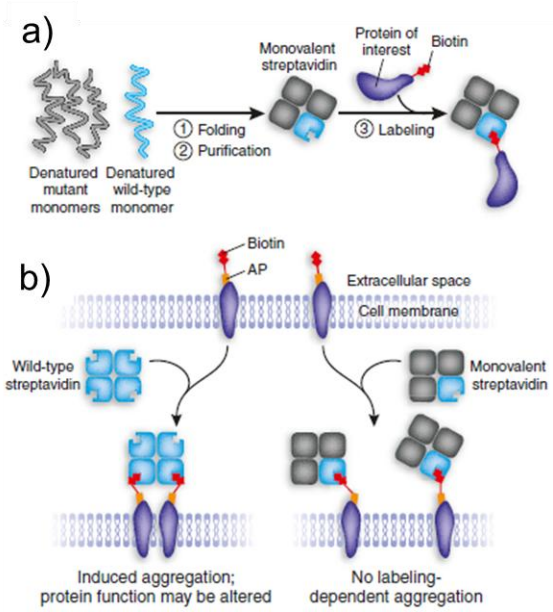


**Figure 1.6** Generation and application of monovalent streptavidin. a) Refolding and purification of mixtures of denatured mutant and wild-type streptavidin in a 3:1 ratio generates monovalent streptavidin. b) A cell-surface protein of interest is expressed as fusion with an acceptor peptide (AP) and then is selectively biotinylated by biotin ligase. Labeling with wild-type streptavidin potentially induces cross-linking and aggregation of the protein of interest, but such cross-linking should not be observed with monovalent streptavidin. Adapted with permission from reference.[162] Copyright 2006 Springer Nature.

Similarly, a rhizavidin monomer which has the same affinity for biotin conjugates as the multimeric avidin was developed from dimeric rhizavidin through the introduction of point mutations.[163] The rhizavidin has been used to form structurally defined biotin conjugates and image biotinylated cell surface receptors without the formation of artificial receptor clustering, which leads to unspecific cellular uptake.[161, 164-166] However, these methods are

unfit as linkers to assemble streptavidin conjugates with multiple functional groups, or with multiple copies of a functional group.

Assembly the multifunctional streptavidin-biotin conjugates provides the advantages of simple production, monodisperse size and structure,[167-168] and can be developed for specific targeting and delivery. Moreover, the mature biotin labelling technology provides a large repertoire of biotinylated molecules with targeting, sensing, diagnostic and therapeutic entities. Yet, it is still challenging to produce structurally defined streptavidin conjugates with more than one type of biotin labeled molecule and precise stoichiometry. One method to prepare multifunctional streptavidin-biotin conjugates is through competitive binders for the biotin pocket. Heck and coworkers prepared a avidin conjugate with one copy of specific Rho-inhibiting clostridial C3 enzyme and three copies of PMN (polymorphonuclear leukocytes)-binding peptides. To control the stoichiometry of peptides with terminal biotin bound to avidin, a competitive binding assay with 2-(4-hydroxyphenylazo)benzoic acid (HABA) was performed. HABA binds to avidin with lower affinity compared to biotin and shows absorbance at 500 nm in the complexed form. Thus, disappearance of the absorption peak indicates displacement of HABA by biotin and allows controlling the relative stoichiometry.[169] Another method for preparing multifunctional streptavidin/avidin conjugates takes advantage of the binding of iminobiotin, which is pH responsive. Iminobiotin binds with high affinity to streptavidin at a neutral or basic pH, while at acidic pH the affinity is low. Kuan and coworkers prepared pH responsive Janus-like supramolecular fusion proteins using iminobiotin-avidin interaction for functional protein delivery. In this study, avidin was first immobilized onto iminobiotin beads to mask one hemisphere of avidin, followed by the addition of biotinylated DHSA (dendronized human serum albumin) onto the toposelective avidin. The DHSA-avidin heterodimer is isolated by subsequent cleavage from the beads at acidic pH and finally purified by cation exchange chromatography. The resultant DHSA-avidin construct possesses a vacant site at the opposite hemisphere, formerly occupied by the solid phase, for the conjugation of a “cargo” protein.[159] Nevertheless, incorporating more than two functional entities using these methods without restriction on one streptavidin in a controlled fashion is still elusive. So far, only precise tetra -treptavidin conjugates with four different single stranded DNA have been prepared by Song and coworkers.[170] The basic idea of producing multivalent treptavidin-DNA conjugate (mTDC) is straightforward: First a statistical mixture of treptavidin conjugates with four DNA strands was formed and subsequently specific mTDCs were separated through

sequence specific hybridization between DNAs on treptavidin and capture DNAs on magnetic beads (MBs). For each bifurcation step, specific DNA-decorated magnetic beads are required to recognize and capture the target DNAs in the mTDCs. The capture DNAs are complementary to the target DNAs and bound to the surface of the MBs via highly stable covalent bonds based on maleimide-thiol chemistry. The mixture interacts with the capture (DNA-decorated) MBs at each step, and the TDCs with the target DNAs proceed to the next separation step, while those without target DNAs are discarded before the mixture being thermally dehybridized. This approach thus only works for the preparation of protein-DNA conjugates and further functionalization requires conjugates with complementary DNA as was demonstrated with nanoparticles. Thus, a general approach for the preparation of multifunctional streptavidin-biotin conjugates with precise stoichiometries is still needed.

### 1.5 $Ni^{2+}$-NTA-His-tag interaction

Proteins with exposed poly histidine sequences (His-tag) have a high affinity for open metal coordination sites. This property of His-tags has been widely used to separate proteins through a chromatography technique called the immobilized metal ion affinity chromatography.[171] The most commonly used metal ion complex for this purpose is the complex between nitrilotriacetic acid (NTA) and $Ni^{2+}$ ions.[172,173] In the complex of $Ni^{2+}$-NTA and His-tags, the $Ni^{2+}$ ion is in an octahedral coordination environment where four of the coordination sites are occupied by the NTA ligand and two sites by the His-tag, so the specific binding is formed based on the octahedral complex of $Ni^{2+}$ with His-tag (**Figure 1.7a**).[171]

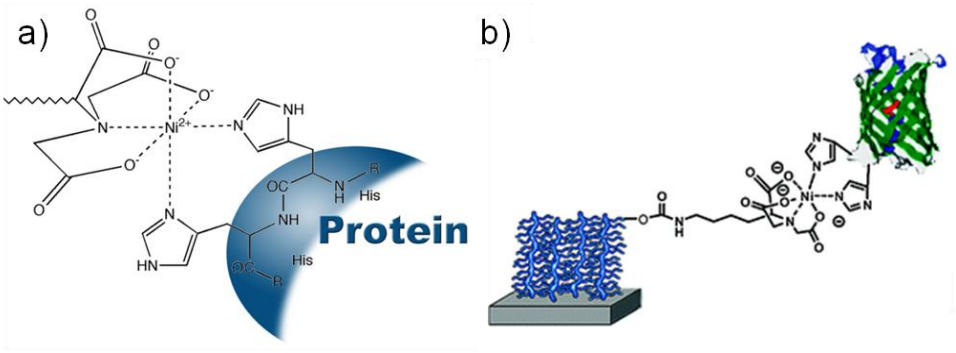


**Figure 1.7** a) $Ni^{2+}$-NTA-His-tag interaction. The $Ni^{2+}$ ion is in an octahedral coordination environment where four of the coordination sites are occupied by the NTA molecule and two sites by the His-tag. Copyright Nanoprobes, Inc. b) Structure and functionalization of polymer brushes with $Ni^{2+}$-NTA, followed by His-tagged green fluorescent protein immobilization. Adapted with permission from reference.[174] Copyright 2010 American Chemical Society.

The binding between $Ni^{2+}$-NTA complexes and His-tags owes its popularity to the fact that it takes place under very mild conditions in the presence of various salts required for protein activity and at neutral pH and the small size of the His-tag (6 (His6) to 10 (His10) histidines are most commonly used), which does not interfere with protein activity. The $Ni^{2+}$-NTA/His-tag interaction is sensitive to pH and chelators, which is a general strategy also to elute His-tagged proteins from columns. The sensitivity to pH depends on whether the metal ligands are protonated or deprotonated. At around neutral pH the NTA ligands are deprotonated and coordinate to the metal ion, while the protonation of the carboxylic acids and the amine abolishes the coordination capacity at a low pH (pH below 5.0). The interaction between the $Ni^{2+}$-NTA complex and the His-tag is also reversible in the presence of competing ligands and most commonly used ones include imidazole, EDTA (ethylenediaminetetraacetic acid) and EGTA (ethyleneglycoltetraacetic acid). While ligands such as imidazole only displace the His-tag from the coordination complex, strong chelators like EDTA and EGTA remove the metal ion from the NTA complex completely. For this reason, imidazole is the most widely used option for the elution from $Ni^{2+}$-NTA columns. Protein can be eluted by increasing the imidazole concentration, typically from 100 to 250 mM, depending on the number of histidines they contain in their His-tags. Moreover, low concentration of imidazole (10-30 mM) are commonly used to wash off non-specifically bound proteins. EDTA as a stronger ligand than imidazole will already elute proteins at low concentrations (5-10 mM) and remove the nickel ions from the NTA complex. The easy and straightforward purification of His-tagged proteins has made it by far the most commonly used method for the purification of recombinant proteins and large libraries of His-tagged proteins have been preparedes.[173]

The high specificity of the $Ni^{2+}$-NTA/His-tag interaction and the availability of His-tagged proteins has extended its use far beyond just protein purification and has made it a reliable biofunctionalization strategy. Nowadays, numerous molecules and materials with the NTA or His-tag functionality are commercially available, including nanoparticles, lipids, polymer beads, antibodies, fluorophores, polymers, and small molecules with other functional groups (e.g. biotin, thiols). The development both on the protein and the synthesis side has been extended the use to numerous other applications such as the incorporation of active proteins in nanomaterials[175-176] and on surfaces,[177-180] the immobilization of proteins on lipid vesicles[25, 34] and polymer beads,[181] specific immobilization of proteins on protein chips,[182-183] the labeling of proteins with fluorophores,[184-187] the synthesis of biofunctional hydrogels,[188] the

specific conjugation and separation of biomolecules with proteins.[189-191] For example, Gautrot and coworkers, functionalized protein-resistant polymer brushes, including poly(oligoethylene glycol methacrylate) (POEGMA) and poly(hydroxyethyl methacrylate) (PHEMA), with NTA end group that can complex with His-tagged proteins selectively and reversibly. The preserved protein resistance of NTA functionalized brushes was used to generate well-defined binary biofunctional patterns via a simple protocol of incubations and washes (**Figure 1.7b**).[174] In the area of *in cellulo* protein labeling, Christian and coworkers prepared a NTA-dichlorofluorescein conjugate for the selective labeling of His-tagged extracellular proteins. This fluorescent probe has allowed to fluorescently label His-tagged proteins on the extracellular surfaces of HEK 293-T and HeLa cells.[186] In a future study, Guignet and coworkers presented a generic method for the selective, rapid (within seconds) and reversibly labelling of proteins *in vivo* with small molecular probes. These probes comprised a chromophore and multiple NTA moieties, which bind reversibly and specifically to engineered oligohistidine sequences in proteins of interest. The feasibility of the labeling approach was demonstrated with representative ligand-gated ion channels and green fluorescent protein-coupled receptor. The labeling of the ionotropic $5HT_3$ serotonin receptor allowed to characterize *in vivo* the probe-receptor interactions, yielding information on structure and plasma membrane distribution of the receptor.[187] The reliable and specific interaction between $Ni^{2+}$-NTA and His-tagged proteins and its sensitivity to pH and chelators was also used in the context of this thesis for the design of multiresponsive synthetic cells, precise protein micropatterns and streptavidin-biotin conjugates.

# Chapter 2. Multistimuli sensing adhesion unit for the self-positioning of minimal synthetic cells

## Copyright



## Aim

Cells have the ability to sense different environmental signals and position themselves accordingly in order to support their survival. Introducing analogous capabilities to the bottom-up assembled minimal synthetic cells is an important step for their autonomy. This work develops a modular adhesion unit for minimal synthetic cells that is able to sense and integrate four important stimuli: light, pH, oxidative stress and the presence of metal ions and regulate the adhesion to a substrate in response to them. We integrated this multistimuli responsive adhesion unit with a light-driven ATP production module such that it is capable to adhere to substrates under environmental conditions that support its ATP production. This multistimuli responsive adhesion unit provides a new and modular element in producing smart and autonomous minimal synthetic cells that are able to position themselves in environments that meet their needs.

## 2.1 Abstract

Cells have the ability to sense different environmental signals and position themselves accordingly in order to support their survival. Introducing analogous capabilities to the bottom-up assembled minimal synthetic cells is an important step for their autonomy. Here, a minimal synthetic cell which combines a multistimuli sensitive adhesion unit with an energy conversion module is reported, such that it can adhere to places that have the right environmental parameters for ATP production. The multistimuli sensitive adhesion unit senses light, pH, oxidative stress and the presence of metal ions and can regulate the adhesion of synthetic cells to substrates in response to these stimuli following a chemically coded logic. The adhesion unit is composed of the light and redox responsive protein interaction of iLID and Nano and the pH sensitive and metal ion mediated binding of protein His-tags to $Ni^{2+}$-NTA complexes. Integration of the adhesion unit with a light to ATP conversion module into one synthetic cell allowed it to adhere to places under blue light illumination, non-oxidative conditions, at neutral pH and in the presence of metal ions, which are the right conditions to synthesize ATP. Thus, the multistimuli responsive adhesion unit allows synthetic cells to self-position and execute their functions.

## 2.2 Introduction

Cells have the remarkable ability to sense their environments, which allows them to inhabit ones that fit their metabolic needs/life style and escape hostile conditions. This capability requires cells to detect multiple environmental signals (e.g. oxygen levels, pH, light, nutrients), integrate these signals in real-time following a defined logic and come to the final decision to stay or leave under these circumstances. Most cells require neutral pH and nutrients for survival, while some depend on additional more specialized factors, e.g. photosynthetic organisms live in places where the light reaches[192] and anaerobic ones avoid oxygen rich zones.[193] Achieving analogous capabilities in synthetic cells, which are bottom-up assembled systems from modular molecular building blocks with life-like features, would be an important step forward in their autonomy.[14, 194] This bottom-up approach in synthetic biology builds on the idea of producing minimal living systems through the modular synthesis and integration[24, 195] of well-characterized units and modules capable of diverse functions (energy conversion,[196] metabolism,[197] division,[198] growth[199] etc.). In this context, an adhesion module that responds to multiple environmental inputs would allow minimal synthetic cells to sense and position themselves in the right place to carry out their functions

and would represent a key feature for potential applications in biotechnology like drug delivery,[200] nanoreactors,[201] biosensing[202] and bioremediation.[203]

One general strategy of cells to control colonization of environments is to regulate their adhesion to the substrate in response to multiple signals.[204] The real-time response to changes in the environmental inputs requires the direct and integrated sensing of different stimuli by the adhesion coupled receptors of a cell. In minimal synthetic cells different triggers such as temperature,[15-16] pH,[20-21] metal ions,[25] redox potential[27-28] and light[32-34, 205] have been used to regulate their functions, including the adhesion to substrates.[32, 205] While these examples represent systems that respond to one parameter in their environment, the challenge remains to construct "smart" synthetic cells which can sense and integrate multiple signals and adhere to places with the right combination of stimuli to perform their function, analogous to natural cells.

As key feature of life, the synthesis of ATP as the energy currency in cells has been implemented into minimal synthetic cells.[197] In particular, converting light energy into ATP has been achieved in artificial systems through the reconstitution of light driven protons pumps and the ATP synthase into artificial biocompatible membranes, such as liposomes,[32, 37] polymersomes[10] or hybrid vesicles.[40] In these ATP generating systems a light driven proton pump, such as bacteriorhodopsin (bR), establishes a proton gradient, which is used by the ATP synthase to convert ADP to ATP. In these compartments, the functionality of ATP production is mainly influenced by the light-induced build-up of a proton motive force across the membrane as well as on the environmental parameters required for the molecular machineries to be functional. For instance, like many other enzymes, the ATP synthase has a metal ion cofactor, $Mg^{2+}$, which is critical for its activity.[206] Implementing an environmental sensing and adhesion unit into these minimal synthetic cells would allow them to position themselves in the right conditions to produce their energy.

Here we report a modular adhesion unit for minimal synthetic cells that is able to sense and integrate four important stimuli: light, pH, oxidative stress and the presence of metal ions and regulate the adhesion to a substrate in response to them. We integrated this multistimuli responsive adhesion unit with a light-driven ATP production module such that it is capable to adhere to substrates under environmental conditions that support its ATP production. On the other hand, the environmental parameters required for ATP production are related to the synthetic cell adhesion, for instance, the chemical used to move out $Mg^{2+}$ ion (used for ATP

production) will destroy the $Ni^{2+}$-NTA interaction so that the minimal synthetic cell detachs from the substrate. This multistimuli responsive adhesion unit provides a new and modular element in producing smart and autonomous minimal synthetic cells that are able to position themselves in environments that meet their needs.

### 2.3 Results and Discussion

In the first step, we sought to design an adhesion receptor that is able to sense and integrate multiple environmental parameters (including light, pH, oxidative stress and the presence of metal ions) and regulate the adhesion of a biomimetic compartment in response to them. In particular, we were interested in a multistimuli responsive adhesion unit that leads to adhesion under conditions that the light to ATP converting module requires. For this purpose, we proposed using the following molecular components as adhesion receptors for the minimal cell: i) For sensitivity to light and redox condition: The photoswitchable protein interaction between iLID (improved light-induced dimer) and Nano, which specifically binds to each other under blue light illumination and dissociate from each other in the dark.[207-208] We postulated that the iLID protein being an engineered version of the LOV2 domain (light oxygen voltage sensing domain 2) from *Avena sativa* would also be sensitive to oxidative stress. ii) For sensitivity to pH and presence of metal ions: The binding of His-tagged proteins to $Ni^{2+}$-NTA (nitrilotriacetic acid) groups, which requires the presence of a mediator ion such as $Ni^{2+}$ and reliably forms at neutral pH but is disrupted at acidic pH or in the presence of chelator such as EDTA (ethylenediaminetetraacetic acid).[209] In our design of an adhesion receptor that can integrate all the different inputs, we linked the His-tagged version of one of the proteins, iLID, onto the surface of a minimal cell model through $Ni^{2+}$-NTA linkers and functionalized a substrate with the second protein, Nano. In this design, the minimal synthetic cell should adhere to the substrate when both links through the light dependent protein-protein interaction and the $Ni^{2+}$-NTA/His-tag binding are in place. These interactions require the blue light to be on, non-oxidative conditions, the pH to be neutral and the presence of $Ni^{2+}$ ions (**Figure 2.1**). Thus, this adhesion unit has the potential to sense these four parameters and respond to different combinations of them differently following a chemically coded logic. The environmental parameters sensed by this multistimuli responsive adhesion unit are highly relevant as many organisms require neutral pH, non-oxidative conditions and the presence of essential metal ions and the presence of light specifically for photosynthetic cells.

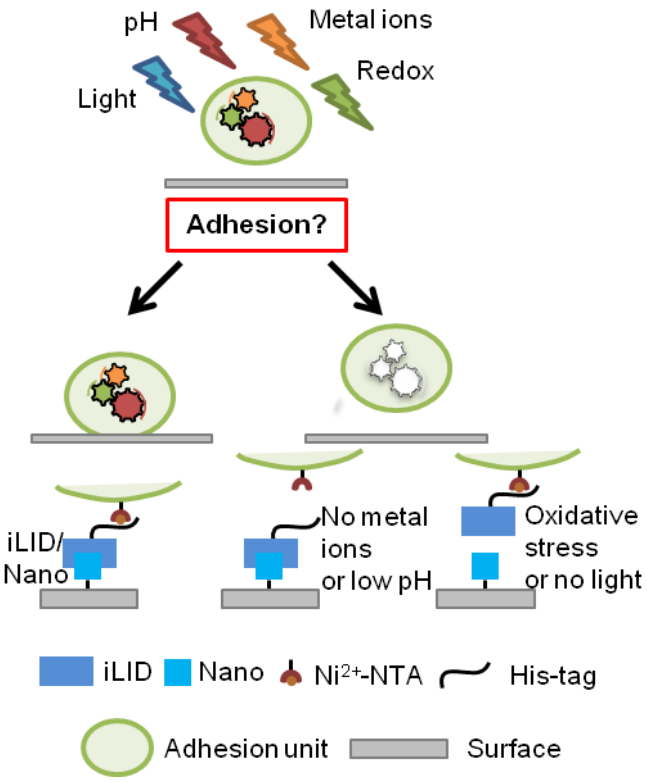


**Figure 2.1** The design of the multistimuli responsive adhesion unit. The adhesion unit responses to light, pH, oxidative stress and the presence of metal ions. The adhesion unit is composed of two molecular components: The photoswitchable protein pair iLID (improved light-induced dimer) and Nano, which specifically binds to each other under blue light illumination and dissociate from each other in the dark, non-oxidizing conditions, as well as the $Ni^{2+}$ mediated interaction of His-tags with NTA groups at neutral pH, which is disrupted at low pH and in the presence of chelators. The membrane anchored multistimuli responsive adhesion ($Ni^{2+}$-NTA/His-tag/iLID) unit allows the minimal synthetic cell to integrate the four environmental parameters and alter its adhesion to a Nano functionalized substrate. In this design, the minimal synthetic cells adhere to the substrate under blue light illumination, under non-oxidizing conditions, at neutral pH and in the presence of metal ions. On the other hand, if one of these parameters is not satisfied the cell does not adhere to the substrate.

To demonstrate the multiresponsiveness of this adhesion unit, we used 2 μm PS (polystyrene) beads as models to test the adhesion unit (the size of PS beads are not much different from some cells) and investigated their adhesion to a glass substrate under all possible combinations of the 4 stimuli, resulting in 16 different conditions. For this purpose, PS beads were functionalized with a His-tagged iLID through $Ni^{2+}$-NTA functionalities at their surface. On the other side, the protein interaction partner Nano was immobilized onto a PEG (polyethylene glycol) coated glass substrate also using the interaction between $Ni^{2+}$-NTA and the His-tag of the protein. Subsequently, the functionalized PS beads were added on top of the functionalized glass surface. The number of beads binding to the substrate (nonbinding beads were washed off with buffer) under different conditions was quantified using bright

field microscopy. More than 1200 beads/mm$^2$ bound under blue light illumination, at neutral pH, non-oxidative conditions and the presence of $Ni^{2+}$ ions (**Figure 2.2a, f**). Furthermore, the adhesion of the functionalized PS beads to the substrate was responsive to changes in the environmental parameters.

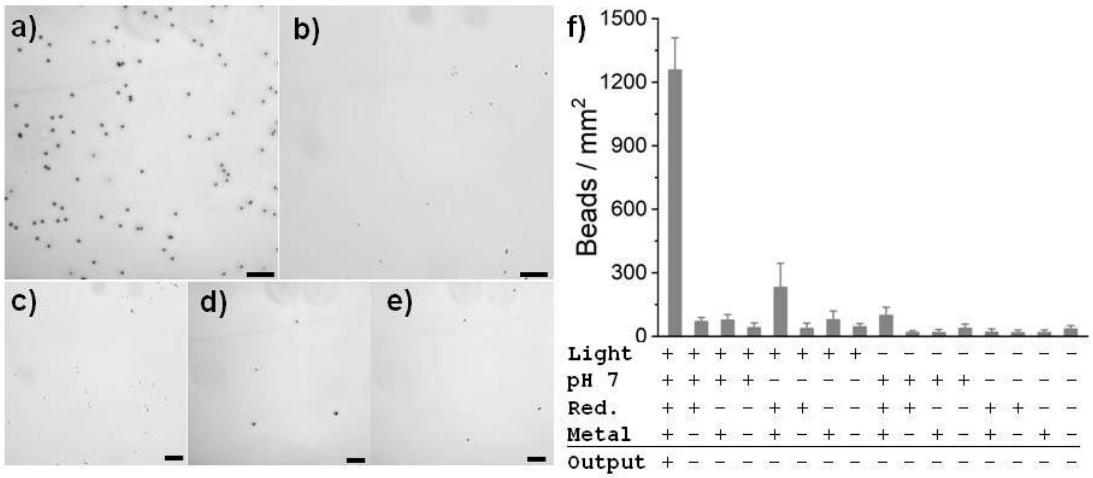


**Figure 2.2** Adhesion of His-tag/iLID functionalized $Ni^{2+}$-NTA-PS beads on Nano functionalized substrates under different conditions. Bright field images of beads on substrate under (a) light, pH 7.4, non-oxidizing (reducing, Red.) conditions and presence of metal ion (Light +, pH 7 +, Red. +, Metal +), (b) same as (a) but in the dark (Light -), (c) same as (a) but pH 3.5 (pH 7 -), (d) same as (a) but presence of oxidative stress, 10 mM $H_2O_2$ (Red. -), (e) same as (a) but in the presence of 50 mM EDTA (Metal -). Scale bars are 25 µm. (f) Number of beads on the substrate under different conditions. The average from 30 images was reported and error bars represent the standard error.

Light: Under otherwise identical conditions no beads attached to the glass in the dark (**Figure 2.2b, f**). This observation showed the sensitivity to light conferred by the iLID/Nano interaction.

pH: When the pH was changed from neutral (pH 7.4) to acidic (pH 3.5), only few beads attached (**Figure 2.2c, f**). One explanation for this observation is that at pH 3.5 the ligands of the $Ni^{2+}$ are protonated and no longer mediate the $Ni^{2+}$-NTA/His-tag binding. Beads will be immobilized on the surface by the interaction of iLID/Nano (only little beads on the substrate without the iLID/Nano pair, **Figure 2.3a**).

Oxidative stress: The attachment of the functionalized PS beads to the substrate was also disturbed under oxidative stress (10 mM $H_2O_2$) (**Figure 2.2d, f**). We demonstrated with the DTNB assay that $H_2O_2$ results in the oxidation of a key cysteine in the iLID protein, which as part of the photoresponse reacts with the flavin cofactor under blue light (**Figure 2.3b**).[132] As

a result of the $H_2O_2$ treatment iLID no longer bound to Nano under blue light as shown by QCM-D (**Figure 2.3c**). As demonstrated in previous studies the interaction between $Ni^{2+}$-NTA and His-tagged proteins is not affected by $H_2O_2$.[209]

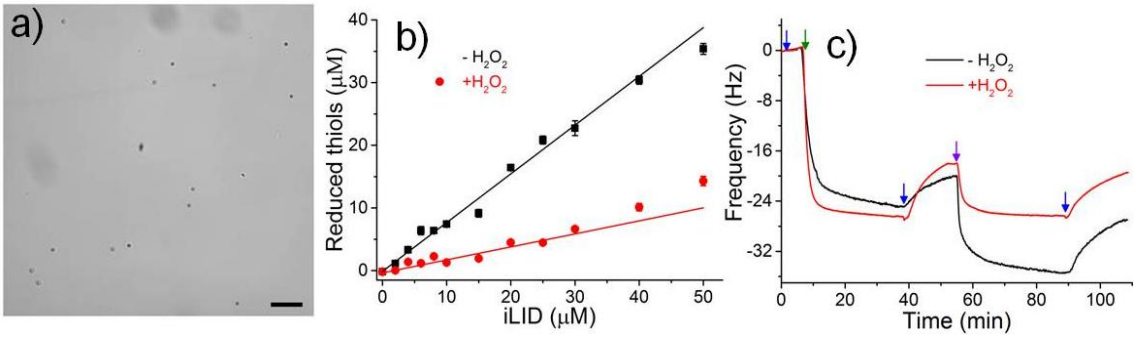


**Figure 2.3** (a) Adhesion of His-tag/iLID functionalized $Ni^{2+}$-NTA-PS beads on cut-Nano (without His-tag) functionalized substrate under light, pH 7.4, non-oxidizing (reducing, Red.) conditions and presence of metal ion (Light +, pH 7 +, Red. +, Metal +). Scale bar is 25 µm. (b) Influence of $H_2O_2$ on the oxidation of cysteines in iLID. The free thiols in iLID before and after exposure to 10 mM $H_2O_2$ for 2 h at 4 ℃ were quantified using the DTNB assay. The analysis showed that 78% of the thiols were oxidized after the exposure to $H_2O_2$. Experiments were performed in technical triplicated and the error bars represent the standard error. (c) Influence of $H_2O_2$ on the binding of iLID to Nano. QCM-D curves of 1 µM iLID without (back line) and with (red line) preexposure to $H_2O_2$ (10 mM $H_2O_2$ for 2 h at 4 ℃) binding to $Ni^{2+}$-NTA groups (5 mol% DGS-NTA-$Ni^{2+}$) on lipid bilayers (green arrow) and the subsequent binding of cut-Nano (without His-tag) (500 nM) under blue light (purple arrow). Blue arrows indicate washing steps with buffer A. The preexposure of iLID to $H_2O_2$ did not influence the binding to $Ni^{2+}$-NTA groups on the lipis bilayer but the interaction with Nano under blue light.

Presence of metal ions: The removal of metal ions i.e. $Ni^{2+}$, by adding 50 mM EDTA also disturbed the adhesion of the PS beads to the substrate (**Figure 2.2e, f**). In this case the chelator EDTA removed the mediator ion $Ni^{2+}$, breaking the link between NTA and His-tag.

These findings showed that changing one of the environmental parameters already was enough to disrupt the adhesion of the PS beads to the substrate. When not just one but more parameters were changed considering all 16 possible combinations (**Figure 2.2f**, **Figure 2.4** and **2.5**), it became apparent that one parameter cannot rescue the effect of another and that only under one condition (blue light, pH = 7.4, no $H_2O_2$, presence of metal ion) the PS beads adhered to the substrate. Thus, the four environmental parameters are connected by a fourfold AND logic and both the iLID/Nano and the $Ni^{2+}$-NTA/His-tag interaction are necessary molecular building blocks for the multistimuli responsive adhesion unit.

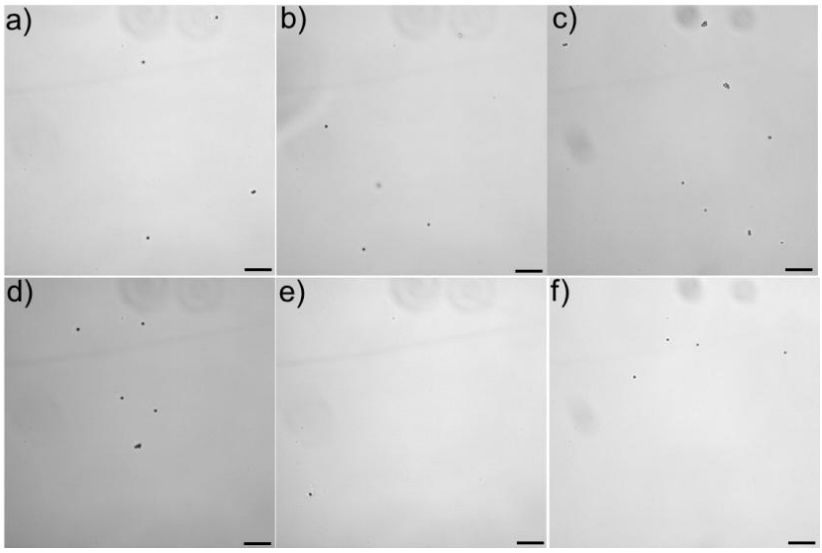


**Figure 2.4** Adhesion of His-tag/iLID functionalized $Ni^{2+}$-NTA-PS beads on Nano functionalized substrates under blue light (Light +) and varying other environmental parameters. Bright field images of beads on substrate under (a) Light +, pH 7 -, Red. -, Metal +. (b) Light +, pH 7 -, Red. +, Metal -. (c) Light +, pH 7 +, Red. -, Metal -. (d) Light +, pH 7 -, Red. -, Metal -. (e) Light -, pH 7 -, Red. -, Metal -. (f) negative control, substrate without Nano functionalization. Scale bars are 25 μm.

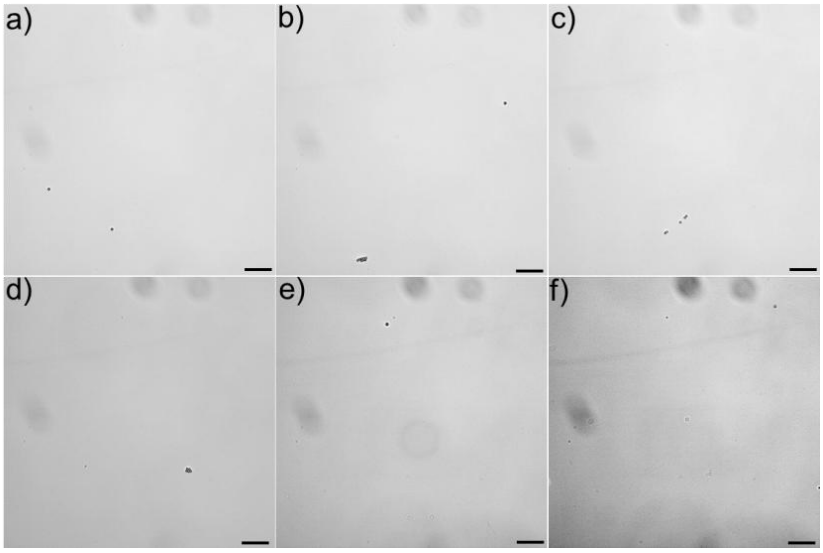


**Figure 2.5** Adhesion of His-tag/iLID functionalized $Ni^{2+}$-NTA-PS beads on Nano functionalized substrates in the dark (Light -) and varying other environmental parameters. Bright field images of beads on substrate under (a) Light -, pH 7 -, Red. +, Metal +. (b) Light -, pH 7 +, Red. -, Metal +. (c) Light -, pH 7 +, Red. +, Metal -. (d) Light -, pH 7 +, Red. -, Metal -. (e) Light -, pH 7 -, Red. +, Metal -. (f) Light -, pH 7 -, Red. -, Metal +. Scale bars are 25 μm.

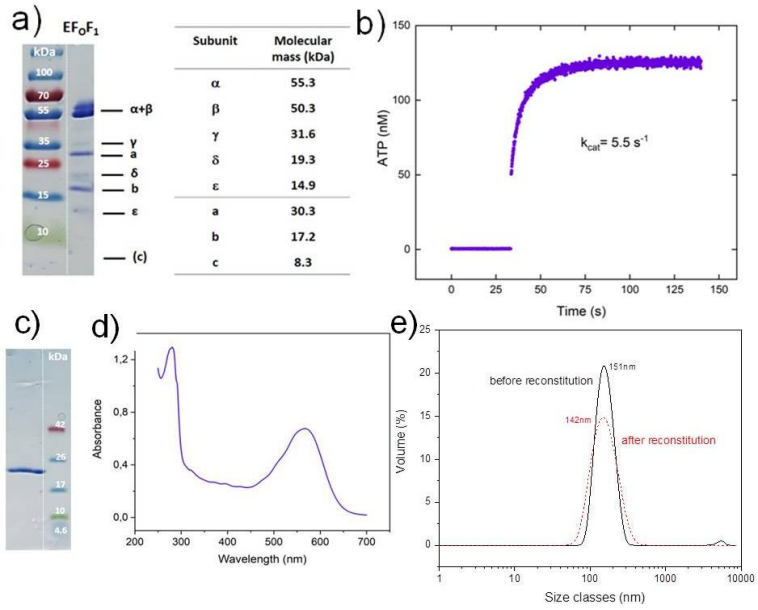


**Figure 2.6** (a) Coomassie-stained SDS-PAGE of purified $EF_0F_1$ ATP synthase and molecular masses of $EF_OF_1$ subunits. (b) Turnover ($k_{cat}$) of ATP synthase as determined in an acid-base transition experiment. The Coomassie-stained SDS-PAGE (c) of purified bR with the corresponding absorbance spectrum (d). (e) Size distribution of vesicles after extrusion through 100 nm pores (before reconstitution) and after coreconstitution of bR and ATP synthase (after reconstitution) as measured by Dynamic Light Scattering (DLS). The mean diameter of the vesicles is 151 nm and 142 nm, respectively. The PDI increases slightly due to reconstitution.

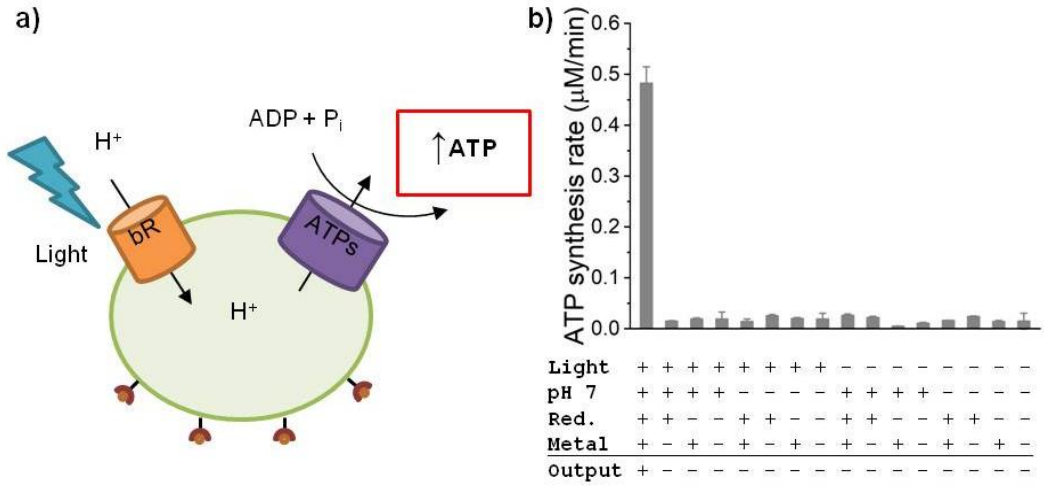


**Figure 2.7** ATP production under different conditions of the light to ATP converting liposomes. (a) Liposomes (142 nm, 10 % DGS-$Ni^{2+}$-NTA lipid) with co-reconstituted bacteriorhodopsin (bR) and ATP synthase (ATPs) convert light to ATP. Under light illumination, bR transports protons across the membrane. The established proton motive force is used by ATP synthase to convert ADP to ATP. (b) ATP synthesis rates under different conditions. Only under illumination (Light +), at neutral pH (pH 7 +), reducing conditions (Red. +) and in the presence of metal ions (Metal +), ATP is produced. In the dark (Light -) and/or at pH 3.5 (pH 7 -) and/or under oxidizing conditions, 10 mM $H_2O_2$ (Red. -) and/or in the absence of metal ions, 50 mM EDTA (Metal -), no ATP is produced. Experiments were performed in triplicated and the error bars represent the standard error.

In the next step, we used cell-like compartments containing an energy conversion modules that is capable of light to ATP conversion and aimed to integrate the multistimuli responsive adhesion unit onto them, such that it could colonize environments that supports ATP production. For this purpose, we investigated the environmental parameters required for ATP production and the sensitivity of the ATP synthesis to different environmental parameters. We co-reconstituted $EF_oF_1$ ATP synthase from *E. coli* (**Figure 2.6a, 2.6b**) and bR from *H. salinarium* (**Figure 2.6c, 2.6d**) in phosphatidylcholine (soy PC) liposomes that were supplemented with lipids baring $Ni^{2+}$-NTA head groups (10 mol%, $Ni^{2+}$-NTA-DGS), yielding vesicles with a mean diameter of 142 nm (**Figure 2.6e, 2.7a**).[37, 210-211]

For the ATP production, the orientation of the transmembrane proteins, bR and ATP synthase, in the lipid membrane are important and ATP will only be produced if the majority is in the correct orientation. In the here used method, the ATP synthase is mainly orientated with the hydrophilic head outwards and the hydrophilic head is unlikely to go through the hydrophobic membrane during reconstitution. Proteolytic digestion of the vesicle reconstituted bR showed that most of the bR is oriented with the C-terminus towards the bulk, which is the functional orientation for transporting protons inside the vesicles (**Figure 2.8a, 2.8b**). Moreover, the proton pumping activity of the bR was confirmed and a pH difference of 0.1 could be generated inside the vesicles (**Figure 2.8c**).

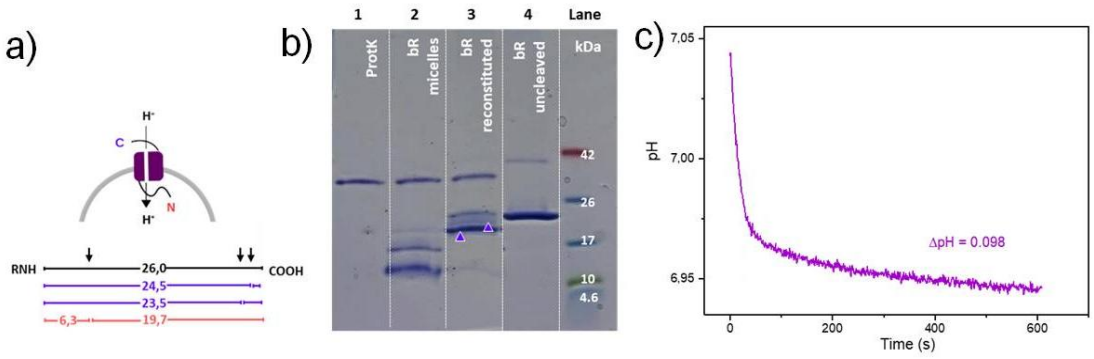


**Figure 2.8** bR orientation and proton pumping activity. (a) For proton pumping into the vesicle, the bR must be oriented such that the C-terminus is exposed to the bulk and the N-terminus is inside the vesicle. Expected sizes of proteolytic fragments of bR (26 kDa) after digestion with proteinase K (ProtK). bR fragments of 19.7 and 6.3 kDa are expected, if the N-terminus is exposed to the bulk (shown in orange) and bR fragments of 24.5 and 23.5 are expected, if the C-terminus is exposed to the bulk (shown in violet). (b) SDS-PAGE analysis of the digestion products show that bR is mainly orientated with the C-terminus outside, which is the functional orientation. Lane 1: band specific for ProtK enzyme only; lane 2: digestion product of not reconstituted bR; lane 3: digest pattern for bR after reconstitution, lane 4: undigested bR after reconstitution in lipid vesicles. (c) Proton pump activity of bR generates a pH gradient of around 0.1.

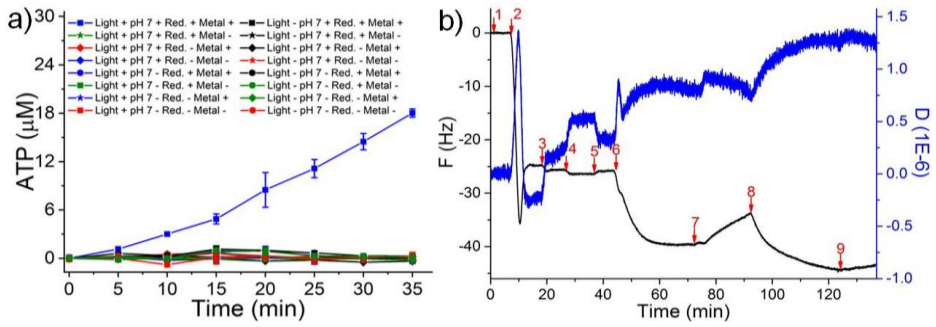


**Figure 2.9** (a) ATP production containing the light to ATP synthesis module under different conditions as measured with luminescence. Significant concentrations of ATP were only produced under illumination (Light +), at neutral pH (pH 7 +), non-oxidizing conditions (Red. +) and in the presence of metal ions (Metal +). In the dark (Light -) and/or at pH 3.5 (pH 7 -) and/or under oxidative stress (10 mM $H_2O_2$) (Red. -) and/or in the absence of metal ions (50 mM EDTA) (Metal -), no ATP was produced. (b) QCM-D curves of pure cut-Nano binding to iLID functionalized lipid bilayers under blue light. 1: buffer A; 2: 0.1 mg/mL DOPC + 5 mol % DGS-NTA; 3: Buffer A; 4: 10 mM $NiCl_2$; 5: buffer A; 6: 1 µM iLID; 7: buffer A; 8: 100 nM cut-Nano; 9: buffer A.

Subsequently, we monitored the conversion of ADP to ATP of these energy modules using an ATP bioluminescence assay changing the environmental parameters (**Figure 2.7b, 2.9a**).[40] Considering all possible combinations of these four important environmental inputs, we tested the synthesis of ATP in 16 different conditions. We found that ATP is produced only upon light illumination (blue light or white light), at neutral pH (7.4), under non-oxidative conditions and the presence of $Mg^{2+}$ ions (2 mM). On the other hand, the ATP synthesis function was disrupted if any of these four parameters were altered, i.e. in the absence of light, at lowered pH (3.5), under oxidative stress (10 mM $H_2O_2$) or the absence of metal ions (50 mM EDTA). These changes in environmental conditions result in the malfunction of different components in ATP synthesis machinery and no conversion of ADP to ATP occurs. For instance, in the dark the bR cannot transport protons from the outside to the inside of the vesicles and EDTA removes magnesium ions, which are the cofactor of ATP synthase and required for its activity. Likewise, oxidative stress (induced by $H_2O_2$) can lead to the oxidation of sulfur containing amino acids (cysteine and methionine) and alter protein structure and activity, which can damage highly sensitive membrane proteins like ATP synthase and bR. Both of these proteins are pH sensitive and inactive at low (pH<4) or high pH (pH>9). Overall, this ATP producing module requires specific conditions to execute its function, which match the response of the developed multistimuli responsive adhesion unit. Finally, we aimed to integrate the multistimuli sensitive adhesion unit onto compartments with the light-driven ATP synthesis module into one synthetic cell, such that it can adhere to substrates under conditions that support its energy conversion (**Figure 2.10a**). To achieve this,

we immobilized Nano onto the lipid vesicles capable of light to ATP conversion using $Ni^{2+}$-NTA lipids as described above. Similarly, the other interaction partner, iLID, was immobilized as a His-tagged protein on a supported lipid bilayer (DOPC + 5 mol% DGS-NTA) formed on a $SiO_2$ QCM-D crystal. It should be noted that either of the proteins, iLID or Nano, can be immobilized on the substrate or vesicle through their His-tags as the interaction between the proteins remains the same in both scenarios.

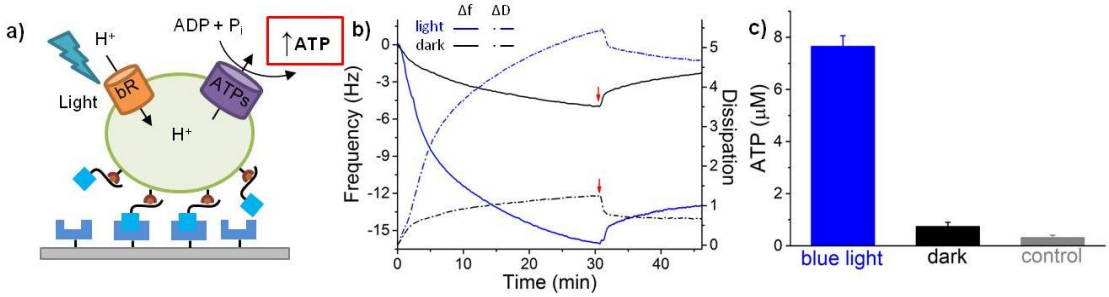


**Figure 2.10** Integration of the multistimuli responsive adhesion module with light to ATP converting energy module. (a) His-tagged Nano was immobilized onto light to ATP converting liposomes (10% DGS-NTA-$Ni^{2+}$ lipid) and His-tagged iLID was immobilized onto a supported lipid bilayer (5 mol% DGS-NTA-$Ni^{2+}$ lipid) on a $SiO_2$ QCM-D crystal. (b) QCM-D curves of Nano functionalized light to ATP converting liposomes on iLID functionalized lipid bilayers in the dark (black) and under blue light (blue). Changes in frequency are shown with solid and changes in dissipation with dashed lines. Red arrows indicate the washing step. (c) ATP synthesis of liposomes that adhered to the QCM-D crystal under blue light or dark, after 30 min subsequent exposure to blue light. As a control one sample was kept in dark both the adhesion step to the QCM-D crystal and the ATP production step. All experiments were performed in triplicated and the error bars represent the standard error.

First, to monitor the adhesion of the lipid vesicles and subsequently their ATP production, we used QCM-D (quartz crystal microbalance with dissipation monitoring) with a window module as a non-interfering and label free method that allows illumination during the measurement. The Nano functionalized lipid vesicles capable of ATP production were either added onto the iLID decorated QCM-D crystal in the dark or under blue light illumination at pH = 7.4 and in the absence of $H_2O_2$ and EDTA (**Figure 2.10b**). Subsequently, nonbinding vesicles were washed off after 30 min incubation. The results of the QCM-D measurement showed that the frequency decreased more under blue light illumination than in the dark ($\Delta f_{blue}$= -12.8 Hz, $\Delta f_{dark}$= -2.3 Hz). The results clearly indicate that more vesicles bound to the crystal under blue light than in the dark as a decrease in frequency correlates with the adsorption of mass to the crystal. In parallel, the dissipation increased more under blue light than in the dark ($\Delta D_{blue}$= 4.8, $\Delta D_{dark}$= 0.6). An increase in dissipation demonstrates the formation of a soft and highly hydrated layer. The particularly large increase under blue light

reveals that entire liposomes filled with buffer adhered to the surface. In comparison, if not entire vesicles but just pure protein Nano bound to the surface the change in dissipation was much smaller ($\Delta D_{blue}$= 1.2 for pure Nano protein, **Figure 2.9b**) due to a rigid protein layer. To evaluate the functionality of the energy conversion module in regard to adhesion on these QCM-D surfaces, buffer with ADP was flushed into the chambers. Both chambers (previously kept in the dark and under blue light during the adhesion step) were illuminated with blue light for 30 min to allow light-driven ATP conversion. At the end, the QCM-D chambers were opened and ATP was measured in the buffer above the crystal (**Figure 2.10c**). This analysis showed that the liposomes that adhere to the surface under blue light are also capable of ATP synthesis. In contrast, for the crystal kept in the dark only few liposomes adhered, resulting in low ATP production upon subsequent illumination. As a negative control one sample was kept in the dark during both the adhesion and the ATP production step. No ATP production was observed in the negative control. Thus, the integration of the multistimuli responsive adhesion unit onto compartments with the light to ATP converting energy module allows these minimal synthetic cells to adhere to places that have the right conditions for the energy conversion. As cells have the ability to sense different environmental signals and position themselves accordingly in order to support their survival, this study provides an approach for a more 'smart' system in the field of synthetic cells.

## 2.4 Conclusions

We are combining multiple stimuli response with the conversion of light to ATP. As in cells, in the multistimuli sensitive adhesion unit different parts in the adhesion receptors are sensitive to various environmental inputs, integrate them and work as sensors that alter adhesions to a surface. This adhesion unit places these synthetic cells into places, which are favorable for many life forms including neutral pH, free metal ions required as cofactors for different metalloproteins and the absence of oxidative stress. The integration of the multistimuli responsive adhesion module is straight forward as demonstrated with micrometer sized PS beads and nanometer sized energy module in this study. The modularity of the adhesion unit comes from the reliable and wide use of the interaction of His-tagged proteins with $Ni^{2+}$-NTA functionalized molecules and materials. The idea of using stimuli responsive adhesion elements to position cells is highly transferable and other interactions than the $Ni^{2+}$-NTA/His-tag and iLID/Nano can be used to colonize different environments with synthetic cells.

# Chapter 3. Green light lithography: a general strategy to create active protein and cell micropatterns

## Copyright



## Aim

The spatial protein patterning provides structural and functional advantages in vast technological applications as well as fundamental research. This work focuses on developing a method of surface patterning proteins and cells with high spatiotemporal control. Layer by layer (LbL) protein system with a green light cleavable protein as the first layer is designed based on the click reaction and $Ni^{2+}$-NTA-His-tag interaction. Using this method, we can incorporate proteins with distinct functions into different layers depending on the application. Our study presents meaningful insights for the assembly of multifunctional protein films which can be used in a wide variety of applications in the field of biomaterials, biosensing, and fundamental cell biology studies.

## 3.1 Abstract

Micropatterns of functional protein are important in biotechnology and research. Using noninvasive wavelengths, green light lithography allows to photopattern active proteins with high spatiotemporal control. Patterns of light are projected onto a layer-by-layer (LbL) multiprotein film, where the green light cleavable protein CarH is integrated into the first layer. CarH is tetramer in the dark and dissociates under green light into its monomers. The LbL protein film is designed to have different functional proteins in each layer based on the specific and polyvalent interactions between $Ni^{2+}$-NTA groups and His-tagged proteins, thus providing oriented protein immobilization under mild conditions to preserve protein activity. This enables the remote release of proteins in the upper layers by exposing the film to green light with 1 μm spatial and 10 s temporal resolution. Green light lithography is successfully used to produce complex patterns of different functional proteins including fluorescent proteins as well as the cell adhesion protein fibronectin. These protein patterns are compatible with cell cultures and the photopatterned fibronectin's allows spatially controlling cell adhesion. Overall green light lithography provides a flexible way to micropattern His-tagged proteins with high spatiotemporal control and in an oriented way by using noninvasive green light assuring protein function.

## 3.2 Introduction

Patterning surfaces with active proteins on the micrometer scale is important in many disciplines from biotechnological applications such as tissue engineering, guiding neuronal growth, biosensing and protein chips to fundamental research for the understanding of cell-material interactions and high throughput screenings.[84] Micropatterned cell adhesion proteins, for example, define where cells adhere on a material. The protein pattern on the micrometer scale determines which specific signaling pathways are activated in the cell.[85] Photolithography, which requires projecting a pattern of light onto a light responsive surface, combines a number of advantages over other micro-fabrication techniques, such as micro-contact printing, lithography and chemical deposition.[212-217] Photolithography also provides high spatial and temporal control, is scalable and cost efficient, while being remote controlled, noninvasive and tuneable.

There are two challenges remaining when using the technique of protein photolithography to achieve micropatterns on active and functional proteins: specific immobilization of proteins and the use of noninvasive visible light. The first challenge - specific immobilization: in

many photopatterning approaches, the surface chemistry is locally altered through exposure to light, which changes the unspecific adsorption of proteins.[110, 218-219] Although widely used, the unspecific adsorption of proteins leads to indiscriminate binding of all proteins in the environment, ill-defined interactions between proteins and substrate, unpredictable unfolding of proteins, and in the worst case inactive orientation on the substrate and loss of activity. To overcome these problems, the specific interactions used to immobilize proteins (e.g. between $Ni^{2+}$-NTA groups and His-tagged proteins,[102, 179, 220] biotin and streptavidin,[221] as well as glutathione and glutathione S-transferase[106]) have been rendered light-responsive and photoactivatable chemical dimerizers[101, 222] have been developed using UV light cleavable caging groups.

The second challenge is that most photopatterning schemes use UV light, which is toxic for cells and damaging to biomolecules. In particular, light cleavable (e.g. nitrobenzenes)[83-84] and light switchable (e.g. azobenzenes) moieties,[87-88] which have been widely used for unspecific and specific protein patterning, both require the use of UV light, which limits their use in cell biology. There are only a few studies in which researchers were able to photopattern proteins with biocompatible near infrared (NIR) and visible light. The advantage of NIR light is that it can be used for protein photopatterning in 3D using two-photon absorption.[106] However, this technique is time-consuming as each point needs to be illuminated sequentially. NIR light can also be used for photopatterning in combination with up converting nanoparticles, which absorb NIR light and emit visible and UV light. For instance up converting nanoparticles were used to locally photocleave a ruthenium complex and the associated unspecifically adsorbed proteins.[87] Recently, proteins were also specifically photopatterned with blue light on lipid vesicles and supported lipid bilayer using the blue and red light-dependent interaction between the proteins, which reverses in the dark or far-red light.[107-108] While the reversibility of these patterns is of benefit when studying dynamics, many biotechnological applications require permanent protein micropatterns. As a result, there is still a requirement to develop a general approach in order to specifically photopattern active proteins of interest with noninvasive visible light.

One of the major applications of protein micropatterns is the control of cell adhesion to enable studies in cell biology and to discover new possibilities in tissue engineering.[109] To date, photopatterning approaches for cells focus on creating local patterns of cell adhesive and repellent regions.[83] This has been achieved by coupling UV light responsive photocaging

or photoswitchable groups to the cell adhesion peptide RGD, by linking nonadhesive polyethylene glycol (PEG) chains to surfaces through nitrobenzene linkers,[79, 223] and immobilizing these molecules to up converting nanoparticles.[224] In order to go beyond the photopatterning of only adhesion peptides, a general approach is still essential to introduce full length adhesion and signaling proteins to the cell by using noninvasive wavelengths of light.

In this study, we present a versatile method of photopatterning oriented and active proteins with green light using layer-by-layer (LbL) multiprotein films. The LbL multiprotein film allows us to incorporate proteins with distinct functions into different layers depending on the application.

### 3.3 Results and Discussion

For green light photolithography, we used CarH,[121-122] a green light cleavable protein, as the light responsive building block. In particular, we integrated CarH into the 1$^{st}$ protein layer to photopattern proteins in the upper layers with green light at high spatiotemporal control (**Figure 3.1a**). Light responsive proteins, like CarH, were employed in the area of optogenetics to control cellular processes noninvasively with light at high spatiotemporal resolution.[225] In recent studies, certain light responsive proteins have also been used as useful building blocks to produce light-responsive hydrogels for controlled hydrogel formation, release of proteins and cells, and also to alter cell migration.[126, 226-227]

The LbL assembly of films is a simple and versatile way of generating substrates with diverse physicochemical and biological properties.[228] In particular, stimuli-responsive (enzyme, pH, temperature, light) LbL coatings have been developed for diverse applications in biosensing, drug delivery, responsive release and cell culture.[59, 70, 78, 229]

Surprisingly, when compared to diverse polymer classes, there are only a few examples of LbL systems with multiple functional proteins, given that different proteins can offer unprecedented functional diversity.[75] For the LbL assembly of multiple proteins, we used the specific interaction between $Ni^{2+}$-NTA groups and His-tags (polyhistidine sequences) of the proteins. This interaction is attractive as it is specific, takes place under mild conditions (in an aqueous buffer at neutral pH and in the presence of other molecules). In addition, NTA modified material as well as His-tagged proteins are readily available. This is the reason why

the interaction between $Ni^{2+}$-NTA groups and His-tags has already been used to assemble a wide variety of protein-based materials ranging from microparticles to hydrogels.[230-231]

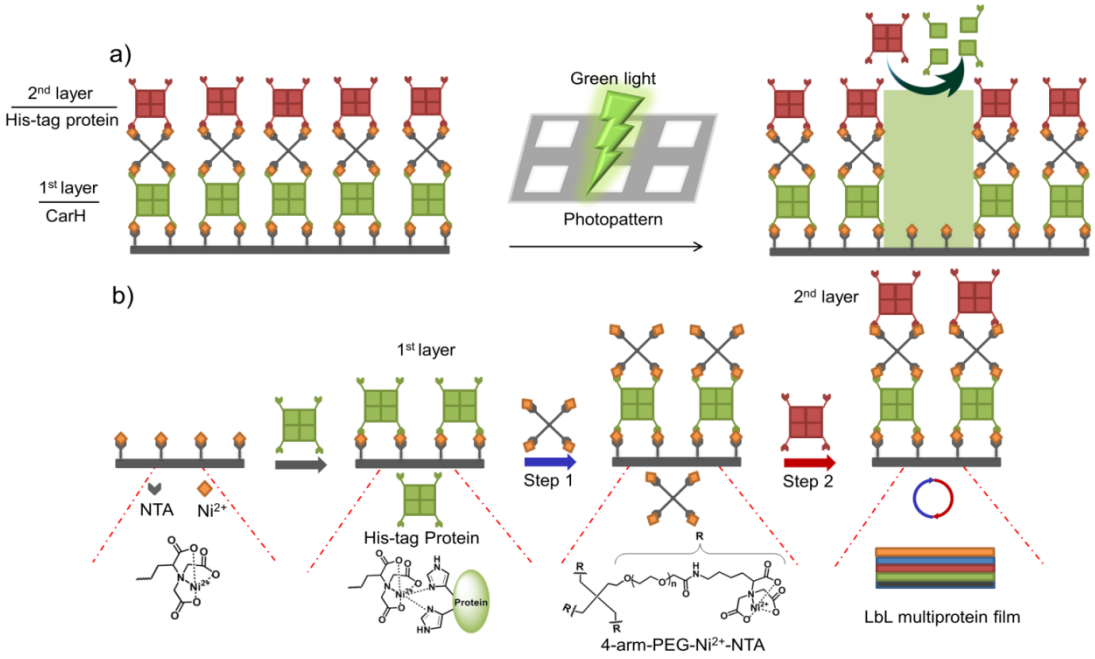


**Figure 3.1** Strategy for green light lithography and the assembly of LbL multiprotein films. a) The green light cleavable protein CarH, which is a tetramer in the dark, is incorporated into the 1st layer so that proteins in the upper layers can be removed locally by projecting a pattern of green light onto the LbL multiprotein film. b) The LbL multiprotein films are assembled using the specific and multivalent interactions between 4-arm-PEG-$Ni^{2+}$-NTA and multimeric His-tagged proteins. A protein with multiple His-tags is immobilized on a $Ni^{2+}$-NTA functionalized surface to form the 1st protein layer. Subsequent layers are formed by alternately adding 4-arm-PEG-$Ni^{2+}$-NTA (Step 1) and a protein of interest with multiple His-tags (Step 2). This allows for the assembly of a LbL multiprotein film with different proteins in each layer.

CarH forms a tetramer in the dark when it binds vitamin $B_{12}$ as its cofactor.[120-121, 125-126] Under green light illumination, the CarH tetramer dissociates into its monomers. We used this light dependent cleavage of the CarH tetramer into its monomers for the photopatterning of proteins, where we integrated CarH in the 1st layer of the LbL multiprotein films and subsequently were able to locally release proteins in the upper layers by the green light illumination. As a model in this study, we photopatterned the red fluorescent protein TurboRFP and the cell adhesion protein fibronectin (FN).[232-233] Photopatterns of FN were then used to pattern cells. Given that the low intensities of green light needed to cleave CarH are not damaging to proteins and cells, it makes this approach highly biocompatible and provides high spatiotemporal remote control.[126] Additionally, the specific interactions between the His-tagged proteins and the $Ni^{2+}$-NTA groups provide specific and oriented

protein presentation to preserve protein activity. These results illustrate a versatile strategy for assembling multiple active proteins into LbL films and photopatterning proteins and cells using noninvasive green light.

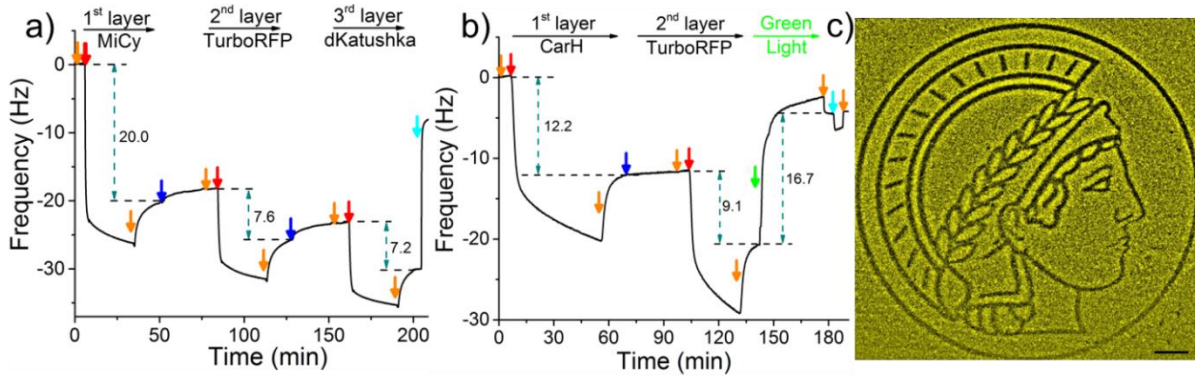


**Figure 3.2** LbL film formation and protein patterning. (a) A 3 protein LbL film is formed on a PEG-$Ni^{2+}$-NTA functionalized $SiO_2$ QCM-D crystal using 4-arm-PEG-$Ni^{2+}$-NTA and the dimeric proteins MiCy (1st layer), TurboRFP (2nd layer) and dKatushka (3rd layer). (b) A light-sensitive LbL protein film using the green light cleavable protein CarH (1st layer) and TurboRFP (2nd layer) is formed on a PEG-$Ni^{2+}$-NTA coated $SiO_2$ QCM-D crystal and removed upon green light illumination. Red arrows: 5 μM of the respective protein, blue arrows: 25 μM 4-arm-PEG-$Ni^{2+}$-NTA, orange arrows: Buffer, cyan arrows: Buffer with 250 mM imidazole and green arrow: green light illumination. The 7th overtone is presented. (c) Proteins were locally patterned by projecting the logo of the Max Planck Society, the Minerva, onto a LbL film with CarH (1st layer) and TurboRFP (2nd layer). The removal of the fluorescent protein TurboRFP from the illuminated areas leads to a dark protein pattern on a bright background. Scale bar: 100 μm.

We began by assembling LbL multiprotein films based on the interaction between His-tags and $Ni^{2+}$-NTA groups. The assembly of such an LbL film requires multivalent interactions between $Ni^{2+}$-NTA groups and His-tagged proteins so that the lower and upper layers in the film can be linked to each other (**Figure 3.1b**). Therefore, we used proteins with multiple His-tags oriented in opposite directions, such as the multimeric proteins that carry one His-tag per monomer (MiCy: dimer, TurboRFP: dimer, dKatushka: dimer, CarH: tetramer). To link the His-tagged proteins in each of the different layers, we synthesized and used a 4-arm-PEG (MW 10 kDa) with $Ni^{2+}$-NTA end groups. As shown in Figure 3.1b, proteins with multiple His-tags bind to a surface with $Ni^{2+}$-NTA groups to form the 1st protein layer. Subsequent protein layers, which form the LbL multiprotein film, are produced by alternately using 4-arm-PEG-$Ni^{2+}$-NTA (Step 1) and a protein with multiple His-tags (Step 2). It should be noted that the protein in the top layer can be any His-tagged protein and does not need to carry multiple His-tags. In this LbL set up, proteins with distinct functions integrated in each layer will determine the overall functionality of the LbL multiprotein film.

To demonstrate the LbL protein film formation based on the above-described method, we used quartz crystal microbalance with dissipation monitoring (QCM-D). QCM-D is a method commonly used to study the adsorption and desorption of macromolecules on surfaces, where adsorption of molecules onto the crystal is observed as a decrease and desorption as an increase in frequency. In order to form the 1st protein layer, we prepared a PEG-coated $SiO_2$ QCM-D crystal, where the PEG chain has terminal $Ni^{2+}$-NTA groups, then the dimeric protein MiCy, where each of the monomers carry a His6-tag, was bound to the surface (red arrow) and the excess protein was washed off with buffer (orange arrow) (**Figure 3.2a**). After the 1st protein layer of with MiCy was formed, 4-arm-PEG-$Ni^{2+}$-NTA solution (Step 1, blue arrow) was passed over the crystal in excess so that $Ni^{2+}$-NTA groups bind to the free His-tags and $Ni^{2+}$-NTA groups in other arms remained free for the next protein layer. Notably, upon addition of the 4-arm-PEG-$Ni^{2+}$-NTA solution there is a slight increase in frequency, which could potentially be due to the sensitivity of QCM-D to changes in viscosity or the removal of some weakly bound proteins from the surface. Subsequently, His6-tagged TurboRFP, dimer, was passed over the surface to form the 2nd protein layer (Step 2, red arrow). By repeating Steps 1 and 2 using a His-tagged dKatushka protein, which is also a dimer, a 3rd protein layer was formed. Further, the QCM-D data could be used to determine the hydrated film by fitting the curves to the Sauerbrey equation. The fitted QCM-D curves give film thicknesses of 4.2, 1.6 and 1.4 nm for the 1st (MiCy), 2nd (TurboRFP) and 3rd (dKatushka) protein layers, respectively (**Figure 3.3a**). Considering that the monomeric unit of a fluorescent protein is 3-4 nm in each dimension, it is apparent that the film thicknesses were less than the height of a protein. This finding support the suggested LbL assembly strategy, where a single nonconfluent layer of protein is added to the film in each step due to the specific interaction between the His-tag and $Ni^{2+}$-NTA groups. When we added an excess of imidazole, which competes with His-tags and disrupts the interaction between His-tag and $Ni^{2+}$-NTA, the components washed off the surface.

a)

| Layer | Thickness (nm) |
|---|---|
| MiCy | 4.2 |
| TurboRFP | 1.6 |
| dKatushka | 1.4 |

b)

| Layer | Thickness (nm) |
|---|---|
| CarH | 3.35 |
| TurboRFP | 2.5 |
| After green light | 1.5 |

c)

| Layer | Thickness (nm) |
|---|---|
| CarH | 2 |
| Fibronectin | 1.25 |
| After green light | 0.25 |

**Figure 3.3** (a) Film thicknesses obtained from QCM-D measurement in Figure 3.2a by fitting the 7th overtone to the Sauerbrey equation. (b) Film thicknesses obtained from QCM-D measurement in Figure 3.2b by fitting the 7th overtone to the Sauerbrey equation. (c) Film thicknesses obtained from QCM-D measurement in Figure 3.6a by fitting the 7th overtone to the Sauerbrey equation.

To use green light lithography to produce protein micropatterns, we next integrated the green light-sensitive CarH tetramer into the 1st protein layer in the LbL protein films, so that we could release proteins in the upper film layers after green light illumination when the CarH tetramer dissociates into its monomers. At this point we used the light sensitive C-terminal adenosylcobalamin binding domain of CarH with a C-terminal His6-tag, which is referred to as CarH in the manuscript.[121-122] In the dark CarH is a tetramer when it binds to adenosylcobalamin and dissociates into monomers upon exposure to green light due to drastic conformational changes in the protein. For green light lithography, the CarH tetramer was immobilized on the $Ni^{2+}$-NTA surface through multiple His6-tags (one on each monomer) to form the first layer protein of a LbL protein film. Subsequently, a second protein layer was assembled on top of the CarH tetramer relying on some of the His-tags that are oriented towards the upper part of the film using first 4-arm-PEG-$Ni^{2+}$-NTA and then a His-tagged protein of choice. Under green light illumination, the CarH tetramer disassembled into its monomers, which broke the linkage between the substrate and the upper layers of the LbL film and lead to the removal of upper protein layers. To integrate the CarH tetramer into the 1st protein layer, we immobilized it on a PEG-$Ni^{2+}$-NTA functionalized $SiO_2$ QCM-D crystal, followed by QCM-D measurements (**Figure 3.2b**). Next, we produced a 2nd protein layer on top of the CarH tetramer layer using 4-arm-PEG-$Ni^{2+}$-NTA (Step 1), and followed by His6-tagged TurboRFP (Step 2). Upon green light exposure to the two layer protein film, both CarH and the TurboRFP dissociated from the surface (green arrow). Fitting the QCM-D data to the Sauerbrey equation showed that the CarH and TurboRFP layers were 3.35 and 2.5 nm, respectively and the film thickness reduced to 1.5 nm upon green light illumination. Upon green light illumination most of the protein was removed from the surface including most of the CarH protein. This is presumably due to the washing off of CarH monomers that were not linked directly to the substrate through their His-tags but to the upper layer $Ni^{2+}$-NTA-PEG and a reduced avidity of the CarH monomer with a single His-tag compared to the CarH tetramer with four His-tags per protein. This observation was also supported by QCM-D results, where just CarH was immobilized onto a $Ni^{2+}$-NTA surface and later illuminated with green light. Upon green light illumination surface bound CarH tetramer was almost completely removed from the surface as dissociates into its monomers under green light (**Figure 3.4a**). Hence, in the LbL multiprotein films the CarH tetramer acts as a green light cleavable linker between the 1st and 2nd protein layers and the protein in the 2nd layer can be flexibly chosen depending on the intended application.

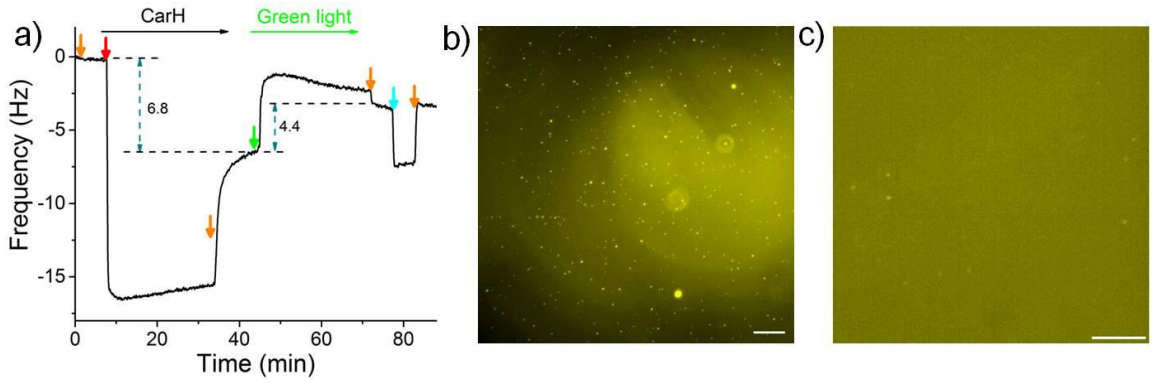


**Figure 3.4** (a) QCM-D measurement of CarH tetramer, the CarH protein is dissociated from the surface in the green light step. (Arrow with different color means different solutions run on the silica crystal, orange arrows: buffer A; red arrow: 5 μM CarH; blue arrow: 25 μM 4-arm-PEG-$Ni^{2+}$-NTA; green arrow: green light illumination; cyan arrow: buffer B). The 7th overtone is presented. This step is used to test if the CarH is still light sensitive when immobilized and if the photocleavage of the CarH tetramer leads to any dissociation from the surface. In the QCM-D measurement, we observe that CarH tetramer dissociates from the surface when illuminate with green light (green arrow) and it indicates that CarH can bind efficiently to the surface as a tetramer through multiple His6-tags but not as a monomer with a single His6-tag. (b) Protein were locally patterned by projecting the logo of the Max Planck Society, the Minerva, onto the pure TurboRFP film in 10% intensity using a digital micromirror device, wavelength 525 nm, exposure time 1 min, scale bar: 100 μm. (c) Patterned protein lines with thickness values from 100 μm to 1 μm onto a just TurboRFP film in confocal microscopy, 20% intensity, wavelength 552 nm, exposure time 10 s, scale bar: 100 μm.

The photocleavable CarH protein layer makes it possible to photopattern complex patterns of a designated protein in the upper layer using noninvasive green light, which we term green light lithography. To demonstrate this, we formed the above-described LbL multiprotein film with CarH and TurboRFP layers on a $Ni^{2+}$-NTA-PEG coated glass surface. Then, using green light, we projected the logo of the Max Planck Society, Minerva's head, onto it for 60 s using a digital micromirror device (DMD, 2048x2048, 0.488 μm/pixel). When the sample was fixed and imaged under a fluorescent microscope, we observed dark areas following the projected pattern on a bright fluorescent background (**Figure 3.2c**) indicating that the fluorescent protein TurboRFP was removed from these regions. As a negative control, we immobilized just TurboRFP on the $Ni^{2+}$-NTA-PEG coated glass surface and projected the same pattern for the same amount of time (**Figure 3.4b**). This did not result in any pattern formation on the surface, showing that the green light projected by the DMD does not result in significant photobleaching. The observed pattern is due to the light-induced CarH cleavage and the resulting protein dissociation. These results demonstrate a versatile strategy for

gaining spatial control of oriented proteins on surfaces and can be flexibly adapted to other His-tagged proteins for the design and production of biosensors and protein chips.

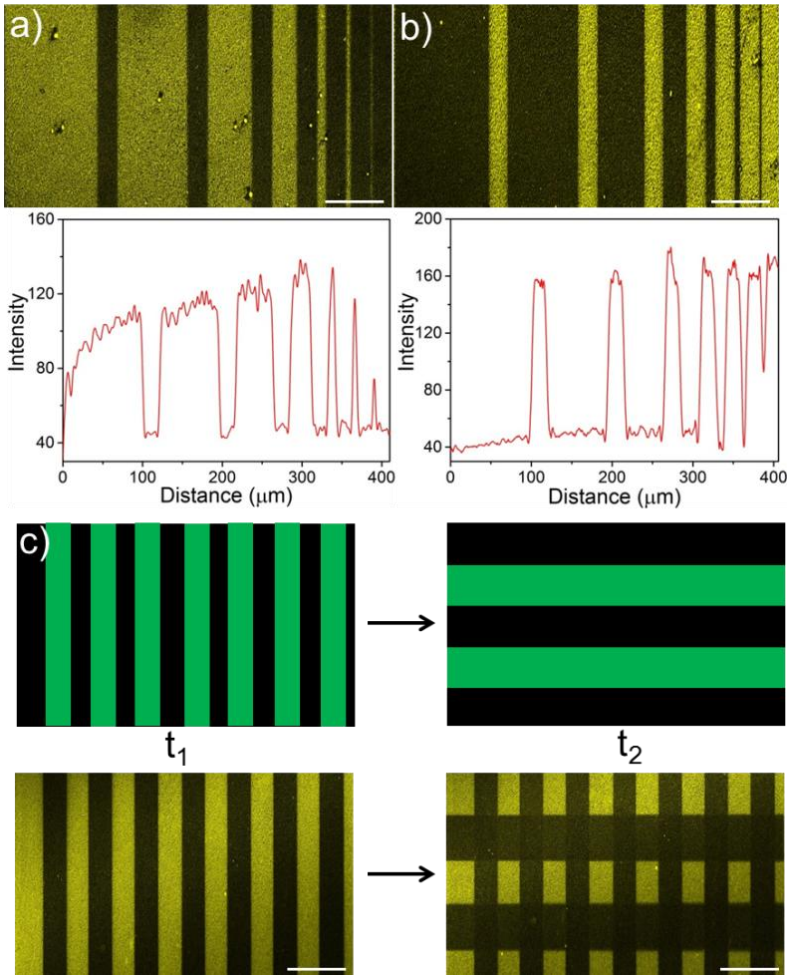


**Figure 3.5** Spatial and temporal control over protein patterns using green light lithography. (a) Protein patterns with thickness of 100 µm to 1 µm (100 µm, 75 µm, 50 µm, 25 µm, 10 µm, 5 µm and 1 µm) separated by 20 µm and (b) 20 µm protein patterns separated by distance from 100 µm to 1 µm on a LbL film with CarH (1st layer) and TurboRFP (2nd layer). Lines of green light corresponding to the dark areas in the protein pattern were projected onto the substrate for 10 s under a confocal microscope. Protein patterns with a resolution down to 1 µm were achieved. Below: Fluorescence intensity profile of the protein patterns. (c) Firstly, 40 µm vertical lines were patterned onto an LbL CarH/TurboRFP film ($t_1$). Subsequently, 80 µm horizontal lines were patterned onto the same substrate ($t_2$), resulting in a cross protein pattern. Hence, protein patterns can be altered at any desired time point. Top: Projected green light pattern, bottom: obtained protein pattern. Scale bar: 100 µm.

Green light lithography provides both high spatial and temporal control over the produced protein patterns. To demonstrate the spatial resolution that this method provides fine lines of proteins with widths from 100 µm to 1 µm and separated by 20 µm were patterned onto an LbL film containing CarH and TurboRFP described above by projecting 20 µm lines with a 552 nm laser for 10 s using a confocal microscope ( 0.568 µm/pixel) . Dark lines following

the projected 20 µm lines with bright areas between them down to 1 µm resolution were observed (**Figure 3.5a**). In contrast, illuminating a pure TurboRFP film (negative control) the same way did not result in any pattern formation (**Figure 3.4c**). Similarly, 20 µm bright lines with distances of 100 µm to 1 µm between them were patterned on LbL CarH/TurboRFP films, when lines with different widths were projected into the substrate (**Figure 3.5b**). So, both positive and negative proteinpatterns with a resolution down to 1 µm were attained using green light lithography. The spatial resolution of 1 µm we obtained for green light lithography is comparable to the resolution obtained for UV lithography in conventional setups[102, 179, 220] but has the clear advantage of using a noninvasive wavelength of light. Theoretically, the minimum feature size is directly proportional to the wavelength and therefore, the resolution for green light lithography (ca. 550 nm) is about two fold lower that for UV (ca. 200-356 nm) lithography. The other important advantage of this method is the high temporal control over protein patterns. To demonstrate this, we first pattered lines of 40 µm widths onto a CarH/TurboRFP LbL film as described above and imaged the protein pattern (**Figure 3.5c**, left). Later at a second time point, we patterned 80 µm lines perpendicular to the first ones on the same substrate, by again illumination for 10 s under the confocal microscope (**Figure 3.5c**, right). Hence, green light lithography does not only allow to pattern proteins with a spatial resolution of 1 µm but also allows for the manipulation of such patterns at a desired time point within 10 seconds.

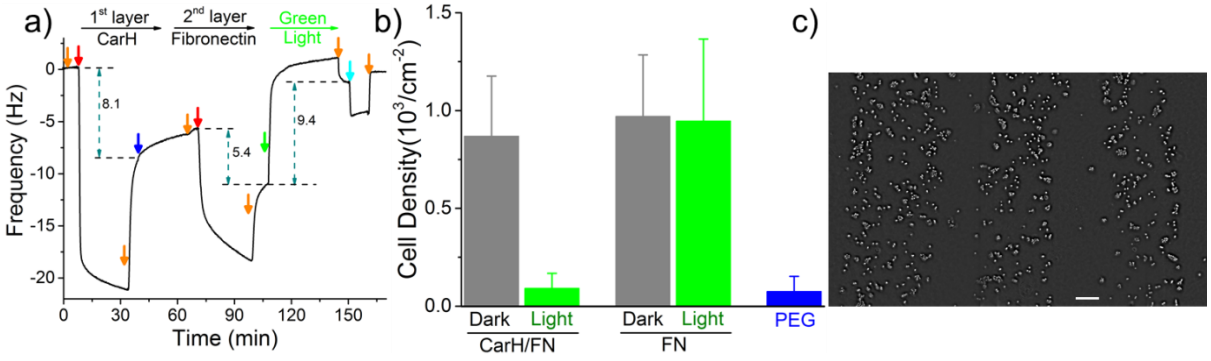


**Figure 3.6** Cell patterning through a patterned fibronectin LbL film. (a) A LbL film with CarH (1st layer) and FN (2nd layer) is formed on a PEG-$Ni^{2+}$-NTA functionalized $SiO_2$ QCM-D crystal and can be removed upon green light illumination. Orange arrows: Buffer, red arrows: 5 µM of the respective protein, blue arrow: 25 µM 4-arm-PEG-$Ni^{2+}$-NTA, green arrow: green light illumination, cyan arrow: Buffer with 250 mM imidazole. The 7th overtone is presented. (b) Quantification of the number of cells that adhere to CarH/FN and FN functionalized surfaces kept in the dark or exposed to green light. Cells cannot adhere to CarH/FN surfaces exposed to green light. (c) Patterned MCF-7 cells on CarH/FN modified surfaces. Cells only adhere to those areas, which were not exposed to green light. Scale bar: 100 µm.

The spatial control of proteins on functionalized surfaces is important in order to guide cell-material interactions in general, and cell adhesion in particular, for applications in tissue engineering and to gain a better understanding of cell biology. The possibility of being able to photopattern a protein of our choice motivated us to control cell adhesion through the patterning of the cell adhesion protein fibronectin (FN). To do this, we constructed a LbL protein film where the 1st layer contains CarH and the 2nd layer contains His-tagged FN and observed the forming by QCM-D (**Figure 3.6a, 3.3c**). As expected, the CarH/FN film is also sensitive to green light and can be removed from the crystal surface by green light illumination (green arrow). Next, we investigated if this CarH/FN film was able to support cell adhesion and if the removal of FN with green light produces nonadhesive surfaces.

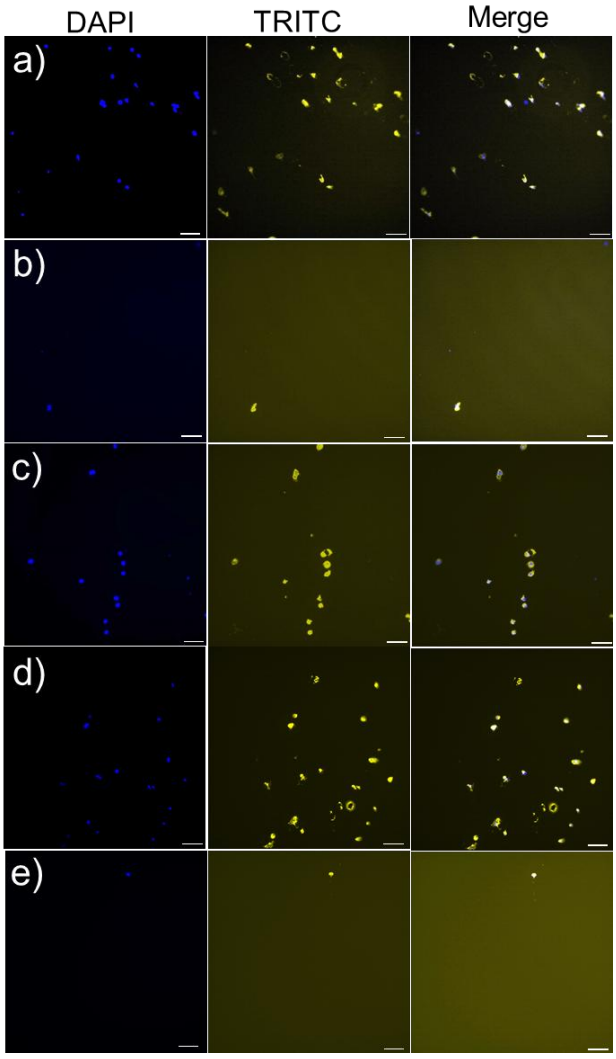


**Figure 3.7** The microscopy image of cell incubated on the (a) CarH/FN modified glass surface under dark environment; (b) CarH/FN modified glass surface under light environment; (c) FN modified glass surface under dark environment; (d) FN modified glass surface under light environment; (e) PEG-NTA modified glass surface. Cell is stained by DAPI (DAPI channel) and Phalloidin/Actin (TRITC channel), scale bar is 100 μm.

With this in mind, we incubated MDA-MB-231 cells ($5.21x10^3$ cells/$cm^2$) for 4 hours on the $Ni^{2+}$-NTA-PEG coated glass surfaces with either a CarH/FN film or just FN as a positive control. While one set of surfaces was kept in the dark, another set of surfaces was exposed to green light for 5 minutes before the cells were seeded (**Figure 3.6b**). First, equal numbers of cells adhered to the CarH/FN surface kept in the dark and to the FN modified surfaces. It should be noted that the cells adhered but did not spread on FN or CarH/FN surfaces, presumably due to the low overall FN concentration on the substrate (**Figure 3.7**). Secondly, only very few cells adhered to CarH/FN surfaces that had been exposed to green light illumination (1.9 % of seeded cells) compared to the CarH/FN surfaces that remained in the dark (25% of seeded cells). In fact, the removal of FN upon green light exposure was very efficient as the number of cells that adhered to green light-exposed CarH/FN surfaces were comparable to the number of cells that adhered to the unmodified $Ni^{2+}$-NTA-PEG-coated glass surfaces. This reduced cell adhesion on CarH/FN films upon green light illumination was clearly due to the photocleavage of CarH, as cells adhere equally well on pure FN surfaces even when exposed to green light. In summary, these results demonstrate that the CarH can be used to photorelease FN from the surface and hence control cell adhesion by using green light.

Next, we set out to photopattern FN with green light lithography to locally control cell adhesion on CarH/FN LbL films. For this purpose, we first projected a striped pattern of green light on a CarH/FN LbL film and then seeded MCF-7 cells onto it (**Figure 3.6c**). The MCF-7 cells adhered to the stripes that were not illuminated, but did not adhere to the illuminated regions, indicating the removal of FN in these areas. The cell patterns, which follow the photopatterned FN, show that spatially controlled presentation of active proteins influences cell behaviour such as cell adhesion. These straightforward protein and cell patterns demonstrate that green light lithography allows for the flexible photopatterning of active proteins on different LbL multiprotein films and can be used in a wide variety of applications in the field of biomaterials, biosensing, and fundamental cell biology studies.

### 3.4 Conclusions

To conclude, we have presented a general method for photopatterning of oriented and active proteins using green light on LbL multiprotein assemblies. The ability to photopattern active proteins with noninvasive green light is based on two scientific advancements. To begin with, we were the first to use the green light cleavable protein CarH as a light-sensitive building

block for photolithography. This provided us with the desired high spatial and temporal remote control over the protein patterns, while being noninvasive and biocompatible. Secondly, we developed a LbL assembly method for multiprotein films based on the specific and multivalent interaction of $Ni^{2+}$-NTA groups and His-tagged proteins, which allowed us to achieve the oriented presentation of a His-tagged protein of interest. The specificity of this interaction and the compatibility with buffered solutions at a neutral pH, are key factors in the bioactive presentation of proteins. We focused here on using these multiprotein LbL films to introduce and remove proteins by using green light and by incorporating His-tagged CarH in the $1^{st}$ protein layer. These LbL multiprotein films can be used for cell patterning, as a promising strategy to modulate cell-material interactions, and to design new biomaterials. The wide availability of His-tagged proteins and $Ni^{2+}$-NTA-modified materials makes this approach highly modular and adaptable for other applications. A further advantage is that the LbL structure of the multiprotein film can be used to control the sequence of released proteins. Given this, we anticipate that this approach will prove highly useful in applications using protein patterning, drug delivery and tissue engineering.

# Chapter 4. Turning cell adhesions on or off with high spatiotemporal precision using the green light responsive protein CarH

## Copyright



## Aim

Spatiotemporal control of integrin-mediated cell adhesions to extracellular matrix regulates cell behavior with has numerous implications for biotechnological applications. This work develops two approaches for regulating cell adhesions in space and time with high precision based on the photo-cleavable protein CarH and the cell adhesion sequence, cRGD. CarH was used to mask cRGD in the first design, which is call GREEN-ON system. In the second design, the GREEN-OFF system, CarH was fused with cRGD and the protein CarH-cRGD was used in the research of cell adhesion. Both designs allow for photoregulation with noninvasive visible light and open new possibilities to investigate the dynamical regulation of cell adhesions in cell biology.

## 4.1 Abstract

Spatiotemporal control of integrin-mediated cell adhesions to extracellular matrix regulates cell behavior with has numerous implications for biotechnological applications. Herein, we report two approaches for regulating cell adhesions in space and time with high precision both of which utilize green light. In the first design, CarH, which is a tetramer in the dark, is used to mask cRGD adhesion-peptides on a surface. Upon green light illumination, the CarH tetramer dissociates into its monomers, revealing the adhesion peptide so that cells can adhere. In the second design, the RGD motif is incorporated into the CarH protein tetramer such that cells can adhere to surfaces functionalized with this protein. The cell adhesions can be disrupted with green light, due to the disassembly of the CarH-RGD protein. Both designs allow for photoregulation with noninvasive visible light and open new possibilities to investigate the dynamical regulation of cell adhesions in cell biology.

## 4.2 Introduction

The cell adhesions to their extracellular matrix (ECM) are of fundamental importance in cell biology, and they are strictly regulated in space and time during different cellular processes including cell migration,[46] differentiation,[47] division[234] and apoptosis.[235] As such biomimetic synthetic materials have provided great insight into the mechanism surrounding cell adhesion processes and have guided material designs in medical applications, tissue engineering and cell-based biosensing devices. Stimuli-responsive ECM mimetic materials that allow altering cell adhesion in response to external stimuli such as light,[223, 236] heat,[237] pH[238] and voltage[239] have attracted a lot of attention. Controlling cell adhesions with light is particularly attractive as it provides regulation with a subcellular spatial and high temporal resolution, unmatched by other stimuli. Studies using photocontrolled cell-ECM interactions with high spatiotemporal control have provided new insight into the role of adhesions in intracellular signal transduction,[240-241] dynamics of cell adhesions,[51, 224, 242] mechanosensing,[243] collective cell migration,[103] vascularization of biomaterials,[83] guiding neuronal growth[244] and stem cell differentiation.[245-246]

Until now, numerous strategies to control cell-ECM interactions with light have been developed. Towards this purpose, photocleavable groups (e.g., nitrobenzyl), which can be removed upon illumination with UV-light, have been used to locally remove nonadhesive PEG (polyethylene glycol) chains and render the surface adhesive.[103, 247] Likewise, photocleavable groups have been coupled to cell adhesion peptides such as the arginine-

glycine-aspartic acid peptides (RGD), which are recognized by integrin receptors, as caging groups[83, 246] or to release them.[86] Linking these photocleavable groups to upconverting nanoparticles has allowed photoregulation with far-red light, thereby overcoming the phototoxicity of UV-light.[248-249] For reversible on/off regulation, photoswitchable groups (e.g. azobenzene) have also been employed to regulate RGD accessibility for integrin binding and mechanical properties of hydrogels using UV light.[250-251] A recent advancement in the field that overcomes limitation in response to UV-light is the integration of light responsive proteins into materials. These proteins respond to noninvasive visible light and can be genetically encoded so that cells can produce them. Hydrogel materials and surfaces coated with such light-responsive proteins allow altering cell adhesion properties[51, 180] as well as mechanical properties[126, 252-254] and thereby, study the dynamics of associated cellular processes. Moreover, photoswitchable proteins have also been integrated into the integrin receptors[255] and used as artificial cell adhesion receptors[256] to photoregulate cell adhesions.

In this manuscript, we demonstrate how to control cell adhesions to RGD motives using the green-light-responsive protein, CarH, as a photosensitive unit. CarH from *Thermus thermophilus* forms a tetramer in the dark when it binds its cofactor $AdoB_{12}$ and dissociates into monomers upon exposure to green light.[122, 127, 180] In two different designs, we were able to either turn cell adhesion on or off upon green light illumination.

### 4.3 Results and Discussion

In the first approach, GREEN-ON, the tetrameric CarH protein was used to form a nonadhesive layer hiding an underlying cRGD adhesion peptides (**Figure 4.1a**). Following green light illumination, the CarH protein layer was removed, and cells could adhere to the exposed cRGD sequences.

In the second approach, GREEN-OFF, we introduced three copies of the adhesion peptide RGD into the CarH protein, yielding CarH-RGD (**Figure 4.2a**). Thereby, cells could adhere to surfaces functionalized with this protein (**Figure 4.1b**). However, when these surfaces were exposed to green light, the adhesive CarH-RGD protein dissociated, and cells could no longer adhere to the PEG coating underneath. Overall, these two designs showed how biocompatible green light CarH could be employed as an alternative to photocleavable groups such as UV-sensitive nitrobenzyl to photoregulate cell adhesions (**Figure 4.2b**). The two approaches were implemented as follows. In the GREEN-ON design, the adhesion peptide cRGD was covered by a nonadhesive and photosensitive layer of CarH tetramer. For this

purpose, glass surfaces were first coated with PEG-azide (a PEG3000 with an azide and a triethoxy-silane terminal group), and the azide groups at the surface were functionalized with a mixture of 0.2% cRGD-alkyne and 99.8% NTA-alkyne using the copper(I) catalyzed azide-alkyne click reaction. Subsequently, the CarH tetramer (light-sensitive C-terminal adenosylcobalamin binding domain of CarH with a C-terminal His6-tag of *Thermus thermophilus*, referred to as CarH in the manuscript) was immobilized onto these surfaces using the specific binding of the His-tags and the $Ni^{2+}$-NTA (nitrilotriacetic acid).[180] We expected that upon green light illumination, the CarH tetramer would disassemble into its monomers and dissociate from the surface efficiently (12% of the initial protein remained on the surface) as previously shown,[180] so that the underlying cRGD motifs are exposed for cell adhesion. The efficient removal of CarH from the surface upon green light illumination is presumably due to the avidity of multiple His-tags in the CarH tetramer, which is lost when it dissociates into its monomers.[180]

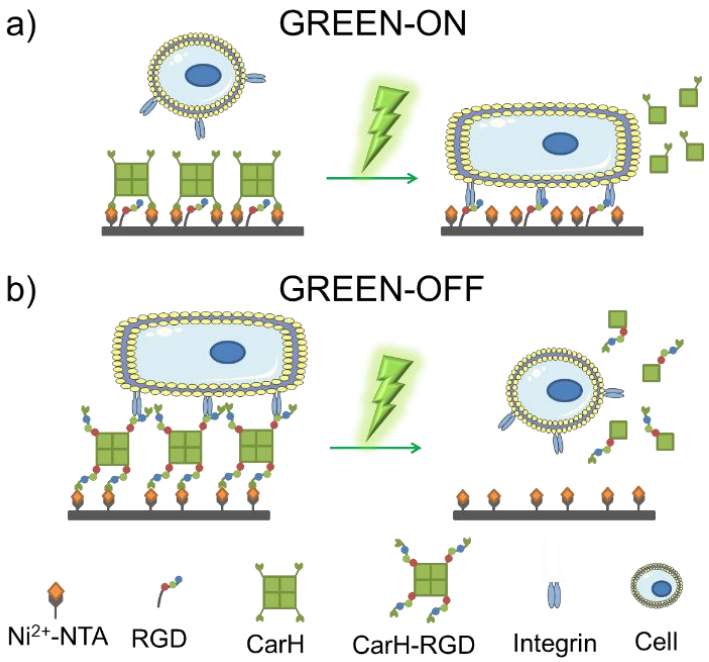


**Figure 4.1** Green light controlled cell-ECM adhesions. a) GREEN-ON design: The CarH tetramer was employed as a nonadhesive layer, which masks the underlying cell adhesion peptide RGD and blocks the binding of integrins. The CarH was immobilized on a PEG coated surface through the NTA-$Ni^{2+}$/His-tag binding. Upon green light illumination, CarH dissociates into its monomers and is removed from the surface, exposing the RGD peptides to integrin receptors on the cell and leads to cell adhesion. b) GREEN-OFF design: The RGD adhesion motif was fused to the CarH to yield CarH-RGD. A PEG coated surface was functionalized with the CarH-RGD tetramer, so that the RGD motifs are exposed for cell adhesion in the dark. Under green light, CarH-RGD dissociated and leads to the detachment of the cells from the surface.

In the second design, GREEN-OFF, the CarH-RGD tetramer was immobilized on top of a PEG layer with $Ni^{2+}$-NTA end groups via the His-tags of the protein. Similar to the parent CarH protein, CarH-RGD forms a tetramer in the dark as shown by size exclusion chromatography (**Figure 4.2c**) and undergoes the same photoreaction as shown by UV-Vis spectroscopy (**Figure 4.2d**). Due to the geometry of the CarH-RGD tetramer,[121] the different C-terminal poly-RGD sequences and His-tags point in opposite directions. Thus, we predicted that two of the poly-RGD sequences close to the His-tags implicated in immobilization would not be accessible to integrin binding as they will be covered by the protein, but the other two poly-RGD sequences would be facing away from the surface and would be exposed for integrins to bind. Thus, upon green light exposure, the CarH-RGD tetramer would disassemble, leaving no exposed adhesion motifs for cell adhesion, similar to the native proteins CarH.[180]

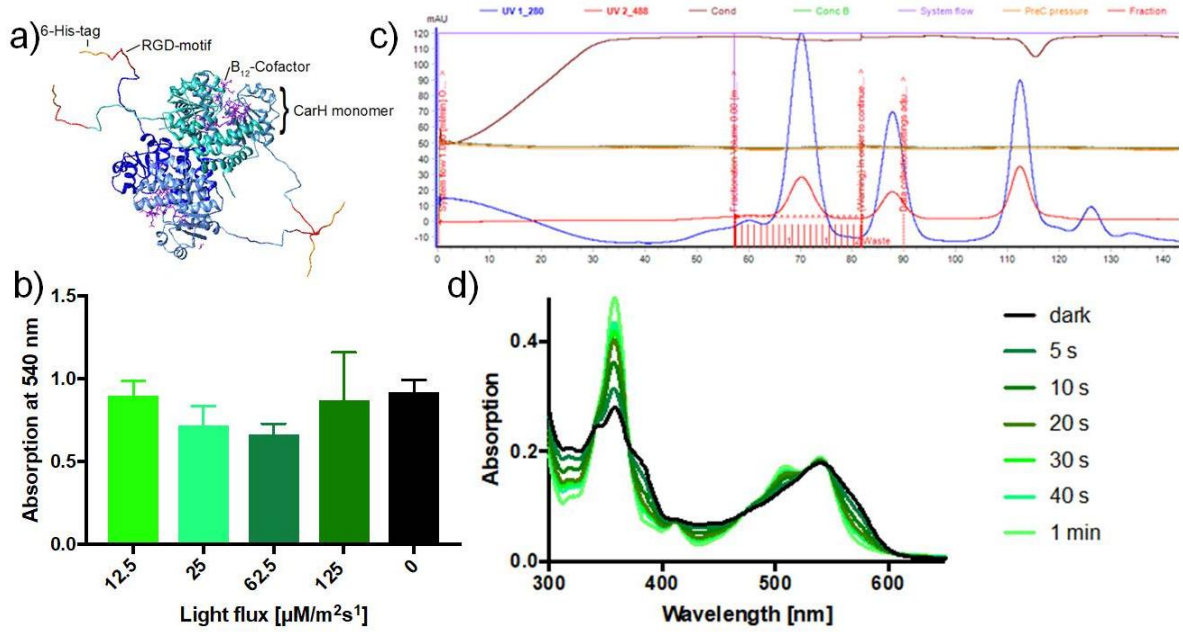


**Figure 4.2** (a) Design of CarH-RGD. a) Cobalamin binding domain of CarH in the dark is a tetramer (PDB: 5C8A) shown in different tones of blue and the cofactor $AdoB_{12}$ in purple. The predicted position of the C-terminal RGD motifs and His-tag are shown in red and yellow, respectively. (b) The metabolic activity of MCF-7 cells after green light illumination for 2 hours and in the dark, was assessed with a MTT assay, showing no decreased activity of cell cultures under different light intensities of green light compared to dark, which shows the nontoxicity of green light. (c) Chromatogram of CarH-RGD on a size exclusion column. Blue curve: Absorbance at 280 nm, red curve: absorbance at 488 nm. The CarH-RGD tetramer eluted at 70 mL, the CarH-RGD monomer at 87 mL and the excess cofactor $AdoB_{12}$ at 115 mL. (d) UV-Vis spectra of the CarH-RGD tetramer upon disassembly under green light. The black curve presents CarH tetramer before exposure to green light and the green curves show the changes over time under green light illumination.

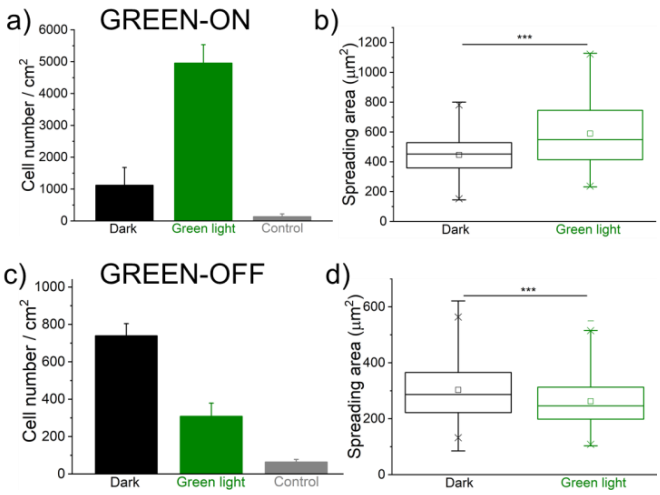


**Figure 4.3** Cell adhesion on GREEN-ON (a, b) and GREEN-OFF (c, d) surfaces. Quantification of (a), (c) the number of cells that adhere based on the nuclear DAPI staining and (b), (d) spreading area of cells based on the actin staining. The surfaces were either kept in dark or illuminated with light for 5 minutes prior to seeding cells. A surface without protein functionalization was used as a control. One Way ANOVA test, *p*-value *** <0.001.

To investigate if cell adhesion can be altered based on these two approaches using green light, we incubated MCF-7 cells on the above-described surfaces. In these experiments, one set of surfaces was kept in the dark, and another set was exposed to green light for 5 minutes prior to cell seeding. A surface with $Ni^{2+}$-NTA-PEG coating was a negative control. As measures of cell adhesion, the number of cells and their spreading area was determined based on the DAPI nuclei staining and phalloidin-TRITC based actin cytoskeleton staining, respectively.

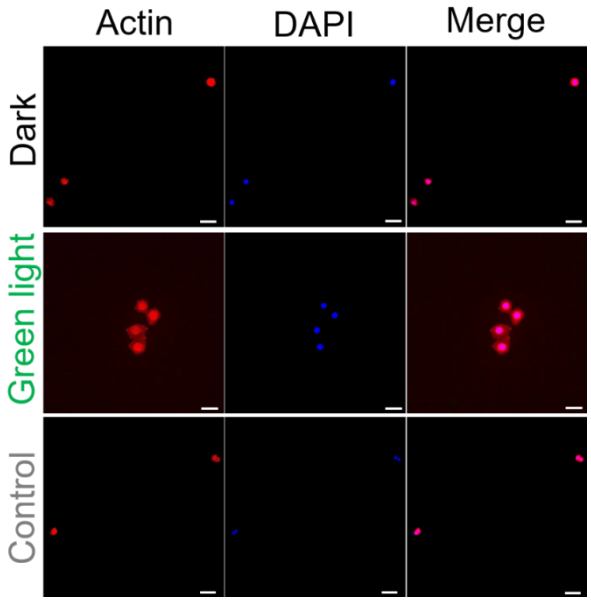


**Figure 4.4** Fluorescence images of cells on GREEN-ON surfaces in the dark and under green light illumination. A surface without any protein and peptide functionalization was used as a negative control. Red: actin, blue: nucleus. Scale bar: 50 µm.

For the GREEN-ON design, very few cells adhered to the surfaces functionalized with CarH that were kept in the dark; however, five times more cells adhered to the surfaces when exposed to green light (**Figure 4.3a**). Moreover, cells cultured in the dark and green light showed a significant difference in their spreading area. Green light illuminated cells spread well and formed actin networks, but in the dark cells did not spread (**Figure 4.3b, 4.4**). Taken together, these findings validate the design principle and indicate that cRGD peptides were hidden under the CarH layer prior to the tetramer disassembly upon green light illumination.

For the second strategy, GREEN-OFF, where the MCF-7 cells were seeded on CarH-RGD functionalized surfaces, the opposite cell adhesion trends were observed. Cells adhered well to surfaces that were kept in the dark but adhered less to surfaces with prior green light exposure (**Figure 4.3c**). Similarly, cells kept in the dark had a significantly larger spreading area on surfaces than ones exposed to green light (**Figure 4.3d, 4.5**).

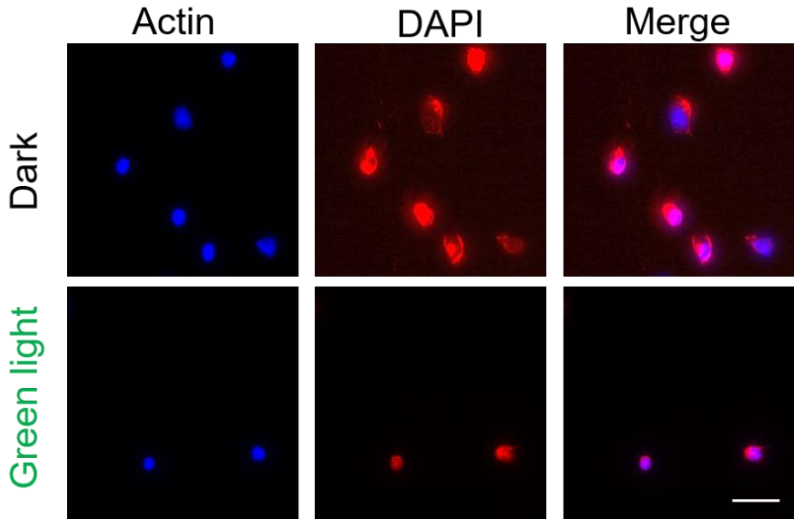


**Figure 4.5** Fluorescence images of cells on GREEN-OFF surfaces in the dark and under green light illumination. In the merged channel, red: actin, blue: nucleus. Scale bar: 50 μm.

Next, we explored the spatial and temporal control that these systems provide over cell adhesions in different set-up. In a first example to demonstrate the spatial control, we used the GREEN-ON system and projected a repeating green light stripe (150 μm) dark stripe (50 μm) pattern onto a surface. Then, we seeded MCF-7 cells on the surface and stained the nuclei and actin cytoskeleton (**Figure 4.6a**). The MCF-7 cells adhered to the regions that were illuminated but not to the unilluminated regions reproducing the striped pattern.

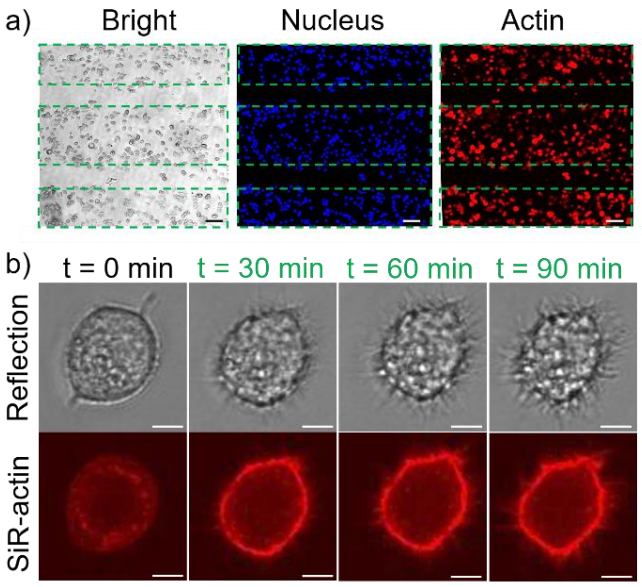


**Figure 4.6** Spatial and temporal control over cell adhesions using the GREEN-ON design. (a) Patterned MCF-7 cells seeded on surfaces that were pre-exposed with a 150 µm wide pattern of green light (dash lines). Cell nuclei are shown in blue and the actin cytoskeleton in red. Scale bars are 50 µm. (b) Green light triggered cell spreading. Top row: Interference reflection, bottom row: SiR-actin staining. Scale bars are 5 µm.

In a second example the GREEN-ON design was used to activate cell adhesions at any given time upon green light illumination, allowing to follow the progression of cell adhesions. To demonstrate this, cells, which were pre-stained with the SiR-actin dye, were seeded onto the surface in the dark. The cells did not significantly adhere to the surfaces, as was evident by their rounded appearance and the lack of actin fibers. Subsequently, a cell that was sitting on the surface was illuminated with green light under a confocal laser scanning, and the changes in morphology and actin structures were monitored. Over the 90 min observation window, the cells spread and established focal contacts with the surface as both visible from the interference reflection channel and SiR-actin actin staining (**Figure 4.6b, 4.7**).

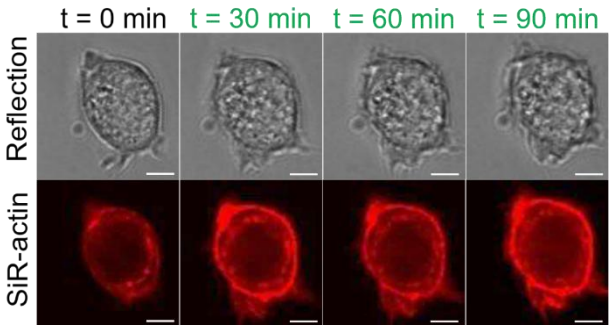


**Figure 4.7** Cell spreading on the GREEN-ON surfaces under green light illumination as monitored with live cell imaging in the interference reflection and SiR-actin channels. Images were first acquired in the dark (t = 0 min) and the cell spreading was monitored over time after 30 min green light illumination. Scale bar: 5 µm.

Complementarily, the GREEN-OFF design based on CarH-RGD coated surfaces allows the disruption of cell adhesions when and where desired. The spatiotemporal control was demonstrated by allowing cells to adhere to a CarH-RGD functionalized surface overnight (**Figure 4.8**). Then, in a field of view a subset of cells was chosen and the selected area was illuminated with green light under the microscope. We observed that the cells in the illuminated area detached from the surface within 20 min and the neighboring cells outside the illuminated area remained attached.

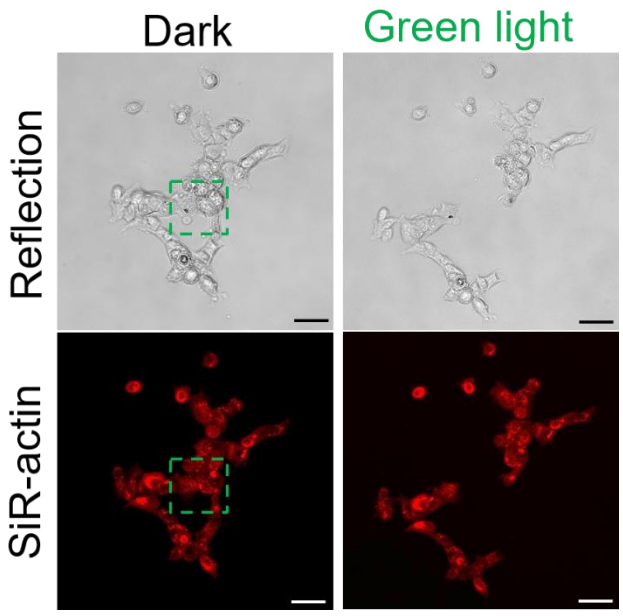


**Figure 4.8** Spatial and temporal control over cell adhesions using the GREEN-OFF design. Cells, which adhered to CarH-RGD functionalized surfaces, were specifically removed in the green light illuminated area (green outline) over 20 min. Scale bars are 50 μm.

### 4.4 Conclusions

In conclusion, we present two approaches for green light regulated cell adhesions that provide noninvasive, biocompatable control over integrin mediated adhesions with high spatiotemporal precision. The photocleavable protein CarH, which these approaches are based on, provides a visible light responsive protein counterpart to the widely used UV-light cleavable functional groups. In the GREEN-ON approach, the CarH was used as a nonadhesive photocleavable layer to hide the adhesion peptide cRGD. This approach is very adaptable and CarH could be used to regulate the exposure of other adhesion or bioactive peptides as well as small molecules. Further, CarH can also be incorporated as a light responsive alternative to non-cell adhesive polymers such as PEG or proteins such as BSA. In the GREEN-OFF approach, we incorporate the RGD cell adhesion motif as a genetically

coded protein component that can be removed with green light. Similarly, other peptide sequences or even protein domains could be incorporated as part of this green light removable protein. The high spatiotemporal precision and high flexibility, which these complementary GREEN-ON and GREEN-OFF designs provide, were here employed to grow cells in precise patterns, trigger cell spreading and remove a spatially defined subset of cells from a surface without the influence of phototoxic UV light. Yet, it should be noted that the response to low intensities of visible green light and the irreversible dissociation of the CarH tetramer requires handling and storing these surfaces carefully in the dark or under red light. Overall, the here presented design principles using CarH as a light responsive ECM component are an important step towards the biocompatible and spatiotemporal control of cell–matrix interactions. Given this, we anticipate that these strategies will be useful for the study of cellular events such as differentiation, cell division, migration and metastasis during which cell-ECM adhesions play an important role and for applications in tissue engineering and biomaterial development.

# Chapter 5. Multifunctional streptavidin-biotin conjugates with precise stoichiometries

## Copyright



## Aim

Streptavidin is used to link different biotinylated molecules thanks to its tetravalent binding to biotin. One side-effect is the resulting statistical mixtures of products. This work provides a general approach to form multifunctional streptavidin conjugates with precise stoichiometries and number of open binding pockets. This method relies on an iminobiotin-polyhistidine tag, which allows separating streptavidin conjugates with different numbers of tags, and later reopening binding pockets at lowered pH to introduce a second functionality. Pure fluorescently labelled mono-, di- and trivalent streptavidin-biotin conjugates prepared in this way were used for imaging biotinylated cell surface molecules with controlled clustering. Moreover, these conjugates were functionalized with a second biotinylated molecule, folic acid-biotin, to investigate the importance of multivalent binding in targeted delivery of cancer cells. These streptavidin-biotin conjugates combined with a variety of biotinylated molecules render this method a diverse and powerful tool for molecular biology and biotechnology.

## 5.1 Abstract

Streptavidin is ubiquitously used to link different biotinylated molecules thanks to its tetravalent binding to biotin. An unwanted side-effect is the resulting statistical mixtures of products. Here, a general approach to form multifunctional streptavidin conjugates with precise stoichiometries and number of open binding pockets is reported. This method relies on an iminobiotin-polyhistidine tag, which allows separating streptavidin conjugates with different numbers of tags, and later reopening binding pockets at lowered pH to introduce a second functionality. Pure fluorescently labeled mono-, di- and trivalent streptavidin-biotin conjugates prepared this way were used for imaging biotinylated cell surface molecules with controlled clustering. Furthermore, these conjugates were functionalized with a second biotinylated molecule, folic acid-biotin, to investigate the importance of multivalent binding in targeted delivery of cancer cells. These streptavidin-biotin conjugates with precise stoichiometries combined with a variety of biotinylated molecules render this method diverse and powerful tool for molecular biology and biotechnology.

## 5.2 Introduction

The binding of streptavidin to biotin is well-known for the strong noncovalent interaction with femtomolar affinity ($K_d$=$10^{-14}$).[148] The high affinity, slow exchange rate, and good specificity of the biotin-streptavidin interaction has resulted in a wide range of biotechnological applications including extracellular and in vitro labelling,[151-152] therapeutics, biosensing and biofunctionalization.[154-155] The large range of biotinylated small molecules, peptides, proteins, antibodies and nucleic acids as well as materials adds to the diversity of the biotin-streptavidin chemistry. Each streptavidin tetramer has four independent biotin binding sites. This tetravalence poses a challenge. On the one hand, it allows streptavidin to be used as a linker between a wide variety of biotinylated molecules with targeting, sensing, diagnostic and therapeutic functionalities and assembling them into one molecule in a modular fashion. On the other hand, tetravalence can be a disadvantage as it leads to statistical mixtures of conjugates when multiple biotinylated molecules are conjugated as well as unwanted cross-linking and aggregation.[161-162] A partial solution to the problems arising from the multivalence are genetically engineered monovalent versions of streptavidin with only one active biotin binding site per tetramer, as well as the use of a monomeric biotin binder, rhizavidin, which can almost achieve multimeric streptavidin-like binding stability for biotin conjugates.[161-162, 164, 166] Alternatively, (strep)-avidins composed of

different subunits have been used to integrate different functionalities within one conjugate.[257-258] These streptavidins have been used to form structurally defined one-to-one streptavidin-biotin conjugates and image biotinylated cell surface receptors without the formation of artificial receptor clustering. However, the monovalent streptavidins are unfit as linkers to assemble streptavidin conjugates with multiple functional groups, or with multiple copies of a functional group. Given this, a method of assembling multifunctional streptavidin-biotin conjugates with precise stoichiometries still remains a big challenge and if successful, it would significantly expand the potential of streptavidin-biotin based technologies.

In this study, we report on a new strategy to assemble multi-functional streptavidin-biotin conjugates with precise stoichiometries and different valancies. Using native streptavidin we were able to produce streptavidin (S) conjugates with one ($SA_1$), two ($SA_2$) or three ($SA_3$) copies of a biotinylated molecule (A), where the residual biotin binding pockets remain open to introduce a second biotin conjugated functionality. Using this method, we were able to produce precise fluorescent streptavidin conjugates for cell surface labeling and to investigate how the number of targeting ligands per conjugate affects cellular uptake. Initial illustrations show how this method can be used to address a wide range of questions in molecular and cell biology.

### 5.3 Results and Discussion

The assembly of multi-functional streptavidin conjugates with precise stoichiometries relies on two well-established chemistries; the separation of proteins by using different numbers of His-tags using $Ni^{2+}$-NTA (nitrilotriacetic acid) columns, and secondly, the pH-dependent binding of iminobiotin to streptavidin (basic pH, $K_d \sim 10^{-11}$ M; acidic pH, $K_d \sim 10^{-3}$ M).[159] In this method, varying numbers of biotin or iminobiotin conjugated His-tags (Bio-His-Tag or Ibio-His-Tag, respectively) were first introduced to streptavidin (**Figure 5.1**).

This allowed for the easy separation of species with differing numbers of His-tags and open biotin binding pockets on a $Ni^{2+}$-NTA column using an imidazole gradient. Subsequently, a biotin conjugated molecule of choice (A) was coupled to the open binding pockets yielding pure streptavidin conjugated with precise stoichiometries ($S(His\text{-}Tag)_3A_1$, $S(His\text{-}Tag)_2A_2$, $S(His\text{-}Tag)_1A_3$). In the case of the iminobiotin conjugated His-tag complexes, the His-tag was released by decreasing the pH to 3.5 and a second biotin conjugated molecule (B) was be added with a precise stoichiometry ($SA_1B_3$,$SA_2B_2$, $SA_3B_1$).

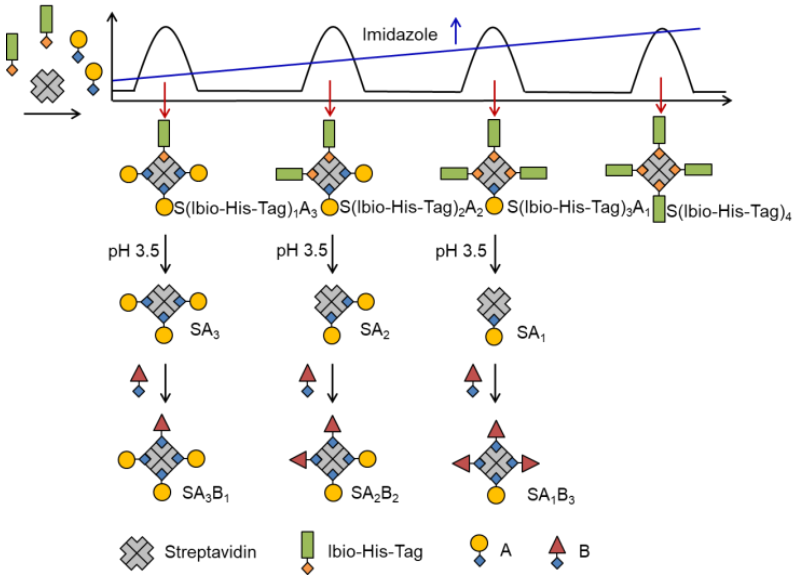


**Figure 5.1** Strategy for obtaining multifunctional streptavidin-biotin conjugates with defined stoichiometry ($SA_3B_1$, $SA_2B_2$, $SA_1B_3$) using the Ibio-His-Tag (iminobiotin-His-tag). The statistical mixture of the four streptavidin conjugates with different numbers of Ibio-His-Tags and the biotin-conjugated molecule, A, can be separated on a $Ni^{2+}$-NTA column based on their number of tags with an imidazole gradient. Once isolated, the Ibio-His-Tag can be removed from each conjugate at pH 3.5 to open the biotin binding pockets and introduce a second biotin conjugated molecule, B.

In a first step, to produce stoichiometrically defined streptavidin conjugates with one functionality, streptavidin, (S = 30 μM) was incubated with a biotin conjugated His6-tag peptide (Biotin-$(His)_6$, Bio-His-Tag = 90 μM), which yielded a statistical mixture of S, S(Bio-His-Tag)$_1$, S(Bio-His-Tag)$_2$, S(Bio-His-Tag)$_3$ and S(Bio-His-Tag)$_4$. Subsequently, the mixture was passed over a $Ni^{2+}$-NTA agarose column; unbound molecules (S) were washed off and different species were eluted using an imidazole gradient, where species bearing more tags eluted at higher imidazole concentrations. In the chromatogram there were four clearly separated peaks that eluted at different imidazole concentrations (relative integrated areas: 19.4% first peak, 14.3% second peak, 20.6% 3$^{rd}$ peak, 45.7% 4$^{th}$ peak) (**Figure 5.2a**).

Presumably the ratio of these peaks can be changed using different S to Bio-His-tag ratios. To demonstrate how each of these peaks corresponds to a single specie with a defined stoichiometry, the open biotin binding pockets of S(Bio-His-Tag)$_{1-4}$ were titrated with biotin-5-fluorescein where the fluorescence is quenched upon streptavidin binding (**Figure 5.2b-e**).[259-260] The streptavidin conjugate in the first peak required 3 equivalents of the dye to saturate all biotin binding sites and therefore was assigned as the S(Bio-His-Tag)$_1$. Likewise, the molecules in the second, third and fourth peaks required 2, 1 and 0 equivalents of dye to

saturate all biotin binding sites, respectively, and they corresponded to S(Bio-His-Tag)$_2$, S(Bio-His-Tag)$_3$ and S(Bio-His-Tag)$_4$, respectively. This assignment is also consistent with streptavidin conjugates eluting at higher imidazole concentrations having more Bio-His-Tags.

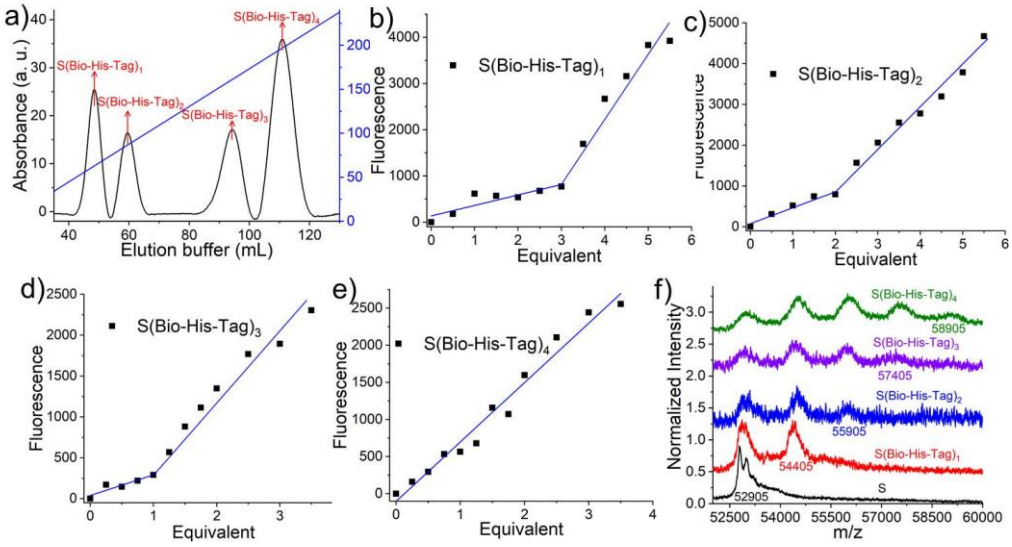


**Figure 5.2** (a) Samples are separated by different concentration of imidazole solution, typically, 30 μM streptavidin was mixed with 90 μM Bio-His-Tag for 15 min, the mixture was loaded on a $Ni^{2+}$-NTA column and washed by a concentration gradient of imidazole, S(Bio-His-Tag)$_1$ (the first peak) occurs at 62.4 mM imidazole and S(Bio-His-Tag)$_2$ (the second peak) was separated at 86.3 mM imidazole, peak 3 (S(Bio-His-Tag)$_3$) was detected at 161.2 mM imidazole and S(Bio-His-Tag)$_4$ (peak 4) occurs at 196.3 mM imidazole. The open biotin binding pockets of S(Bio-His-Tag)$_1$ (b), S(Bio-His-Tag)$_2$ (c), S(Bio-His-Tag)$_3$ (d) were titrated with biotin-5-fluorescein where the fluorescence is quenched upon streptavidin binding. Result indicates S(Bio-His-Tag)$_1$, S(Bio-His-Tag)$_2$, S(Bio-His-Tag)$_3$ required three, two and one equivalents of the dye to saturate all biotin binding sites, respectively. (e) No quench happens in S(Bio-His-Tag)$_4$ titration experiment, indicates all biotin binding pockets have been occupied by Bio-His-Tag. (f) MALDI-TOF mass spectrometry of pure streptavidin (S: m/z 52905), S(Bio-His-Tag)$_1$ (m/z 54405), S(Bio-His-Tag)$_2$ (m/z 55905), S(Bio-His-Tag)$_3$ (m/z 57405) and S(Bio-His-Tag)$_4$ (m/z 58905).

The identity of the different species was further confirmed with MALDI-TOF mass spectroscopy. While S and Bio-His-tag have molecular weights of 52905 and 1500 Da (**Figure 5.3a**), respectively, the different conjugates of S and Bio-His-Tag have higher molecular weights (**Figure 5.2f**). The isolated species with one to four Bio-His-tags had maximal peaks 54405 Da (S(Bio-His-Tag)$_1$), 55905 Da (S(Bio-His-Tag)$_2$), 57405 Da (S(Bio-His-Tag)$_3$) and 58905 Da (S(Bio-His-Tag)$_4$), respectively, which are well in agreement with the theoretically expected values. Moreover, for species with different numbers of Bio-His-Tags lower molecular weight peaks were observed due to the dissociation of the Bio-His-Tag from S in the mass spectrometer. More specifically, there were two peaks for S(Bio-His-

Tag)$_1$ (S and S(Bio-His-Tag)$_1$) and three peaks for S(Bio-His-Tag)$_2$ (S, S(Bio-His-Tag)$_1$ and S(Bio-His-Tag)$_2$), while no peak of S(Bio-His-Tag)$_2$ were observed for S(Bio-His-Tag)$_1$. These results confirm and fully resolve the molecular structure of the prepared streptavidin conjugates with defined stoichiometries.

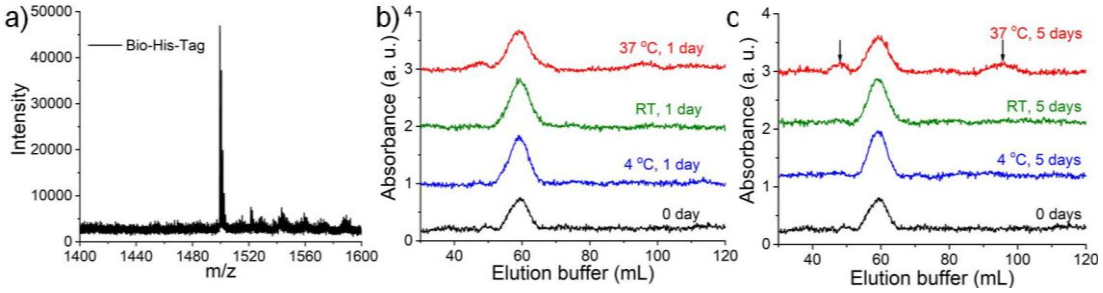


**Figure 5.3** (a) MALDI-TOF mass spectrum of biotin-(His)$_6$ (Bio-His-Tag). The molecular weight is 1500 g/mol. (b) S(Bio-His-Tag)$_2$ were stored at 4 ℃, room temperature (RT) and 37 ℃ separately for one day, then was loaded on $Ni^{2+}$-NTA column and washed by elution buffer. (c) There is no change for samples stored at 4 ℃ and room temperature after five days, while 70% S(Bio-His-Tag)$_2$ kept stable if stored at 37 ℃ for five days, 8.4% and 21.6% S(Bio-His-Tag)$_2$ changed to S(Bio-His-Tag)$_1$ and S(Bio-His-Tag)$_3$, respectively (black arrow).

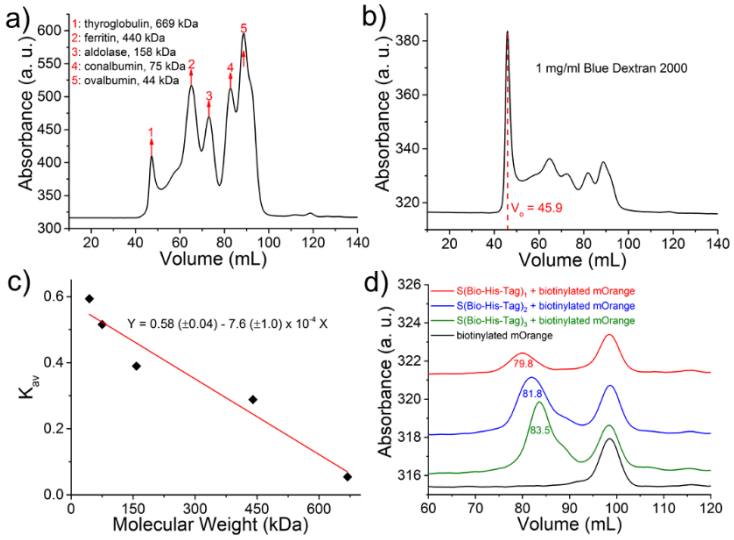


**Figure 5.4** (a) Chromatogram of standard protein mixture and (b) blue dextran 2000 on HiLoad$^{TM}$ 16/600, Superdex$^{TM}$ 200 pg size exclusion column. Elution volumes ($V_e$) for each protein were determined as maximum peak height: peak 1 at 47.2 mL for thyroglobulin (669 kDa), peak 2 at 65.2 mL for ferritin (440 kDa), peak at 73.0 mL for aldolase (158 kDa), peak 4 at 82.7 mL for conalbumin (75 kDa) and peak 5 at 88.7 mL for ovalbumin (44 kDa). The void volume ($V_o$) is the first eluted peak in b) at 45.9 mL. (c) Standardization curve of $K_{av}$ versus protein molecule weight. (d) Chromatogram of different streptavidin conjugates (S(Bio-His-Tag)$_1$ (trivalent), S(Bio-His-Tag)$_2$ (divalent) and S(Bio-His-Tag)$_3$ (monovalent)) reacted with biotinylated mOrange. The molecular weights: mOrange (31.3 kDa) streptavidin (53 kDa), Bio-His-Tag (1.5 kDa). The peaks in the chromatogram were for the reaction of biotinylated mOrange with S(Bio-His-Tag)$_1$, S(Bio-His-Tag)$_2$ and S(Bio-His-Tag)$_3$ were at 79.8 mL, 81.8 mL and 83.5 mL, respectively. The theoretical molecular weight was

calculated assuming that all remaining open binding pockets were occupied by biotinylated mOrange. S(Bio-His-Tag)$_1$O$_3$ (theo. 148.4 kDa, exp. 141.0 kDa), S(Bio-His-Tag)$_2$O$_2$ (theo. 118.6 kDa, exp. 108.6 kDa) and S(Bio-His-Tag)$_3$O$_1$ (theo. 88.8 kDa, exp. 81.3 kDa). The theoretical and experimental molecular weights were in agreement showing that the open binding pockets were indeed occupied by biotinylated mOrange.

The isolated S(Bio-His-Tag)$_1$, S(Bio-His-Tag)$_2$ and S(Bio-His-Tag)$_3$ conjugates are equivalent to trivalent, divalent and monovalent streptavidin and can be used to form precise conjugates with a large variety of biotinylated molecules including small molecules, peptides, proteins, DNA and antibodies. As an example, biotinylated mOrange (orange fluorescent proteins, O, 31.3 kDa) was reacted with the streptavidin (53 kDa) conjugates of varying valences. Each of the conjugates eluted at a different volume on a size exclusion column, and the molecular weights determined, based on a protein standard, were in agreement with the theoretically expected value. S(Bio-His-Tag)$_1$O$_3$ (theo. 148.4 kDa, exp. 141.0 kDa), S(Bio-His-Tag)$_2$O$_2$ (theo. 118.6 kDa, exp. 108.6 kDa) and S(Bio-His-Tag)$_3$O$_1$ (theo. 88.8 kDa, exp. 81.3 kDa) a protein standard (**Figure 5.4**). The agreement between theoretical and experimental values supports the assigned structures and shows the great potential of this approach to form precise protein conjugates. For the success of this approach, the slow exchange rate of the Bio-His-Tag with streptavidin is required so that species isolated in different peaks do not interconvert. To test the kinetic stability, purified S(Bio-His-Tag)$_2$ was stored at 4 ℃, room temperature (RT), and at 37 ℃. After 1 and 5 days, the samples were loaded onto the $Ni^{2+}$-NTA column and eluted using an imidazole gradient (**Figure 5.3b, 5.3c**). The S(Bio-His-Tag)$_2$ stored at 4 ℃ and RT for up to five days eluted as a single peak as did the fresh sample (0 day), demonstrating the long-term stability of isolated species. Even at 37 ℃ after one day, there is not significant changes for S(Bio-His-Tag)$_2$, while after five days at 37 ℃, 30 % of S(Bio-His-Tag)$_2$ converted into S(Bio-His-Tag)$_1$ and S(Bio-His-tag)$_3$.

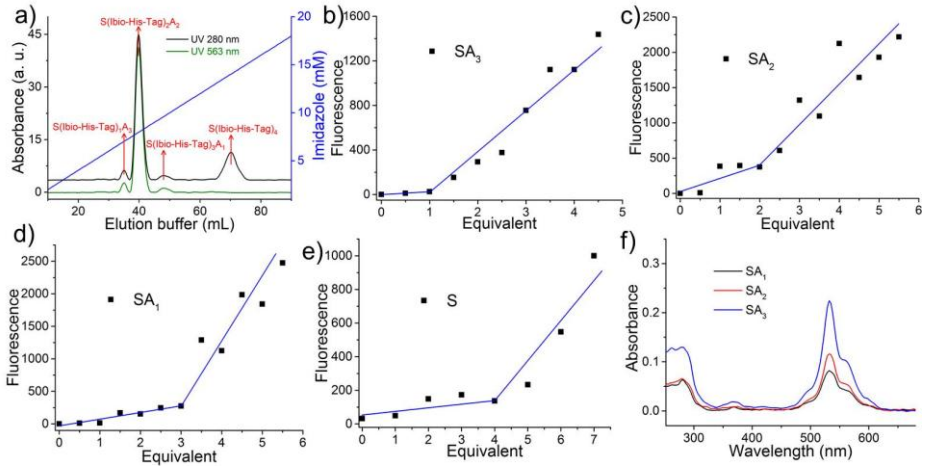

**Figure 5.5** (a) Chromatogram of the reaction mixture of streptavidin (S) (30 µM), which was first reacted with Ibio-His-Tag (90 µM) for 15 min and then with atto-565-biotin (A) (50 µM) for 15 min, separated on a $Cu^{2+}$-NTA column using an imidazole gradient. The elution of different species was monitored through the absorbance 280 nm (both streptavidin and atto-565-biotin absorb) and 563 nm (only atto-565-biotin absorbs). The different $S(Ibio\text{-}His\text{-}Tag)_nA_{4-n}$ species eluted at increasing imidazole concentrations as the numbers of Ibio-His-Tags increases from 1 to 4. First peak at 6.9 mM imidazole was $S(Ibio\text{-}His\text{-}Tag)_1A_3$, second peak at 8.0 mM imidazole was $S(Ibio\text{-}His\text{-}Tag)_2A_2$, third peak at 9.6 mM imidazole was $S(Ibio\text{-}His\text{-}Tag)_3A_1$ and the fourth peak at 14.0 mM imidazole $S(Ibio\text{-}His\text{-}Tag)_4$ (only observed in the absorbance at 280 nm since it does not contain atto-565-biotin). The relative areas of the peaks are: 5.1% 1st peak, 42.6% 2nd peak, 26.7% 3rd peak and 25.6% 4th peak. (b-e) The Ibio-His-Tag was removed from the different $S(Ibio\text{-}His\text{-}Tag)_nA_{4-n}$ species through acidification to yield the corresponding $SA_{4-n}$. The open biotin binding pockets of (b) $SA_3$, (c) $SA_2$, (d) $SA_1$ and (e) S were titrated with the fluorophore biotin-5-fluorescein, which is quenched upon binding to streptavidin. $SA_3$, $SA_2$, $SA_1$ and S required 1, 2, 3 and 4 equivalents the dye to saturate all biotin binding sites, respectively. (f) The UV-vis absorption spectra of $SA_1$, $SA_2$ and $SA_3$ measured by Nanodrop. The absorbance at 280 nm and 532 nm were used confirm the stoichiometry of these streptavidin conjugates.

In the second step, in order to produce precise streptavidin conjugates with two different functional groups, we used an iminobiotin conjugated His-tag (Ibio-His-Tag) instead of the Bio-His-Tag. The Ibio-His-Tag is removable from the streptavidin complex at a lower pH (pH 3.5) and can be used to reopen biotin binding pockets in isolated streptavidin conjugates with precise stoichiometry and a first functionality. The new biotin binding pockets can then be used to introduce a second biotin conjugated molecule. In initial experiments, we noticed that the streptavidin-Ibio-His-Tag complexes had a lower affinity on the $Ni^{2+}$-NTA column. A potential reason for this could be the different orientations of biotin and iminobiotin in the streptavidin binding pocket. While serine 27 of streptavidin acts as a H-bond donor for biotin, it is a H-bond acceptor for iminobiotin.[261] Consequently, the exposure of the connected His-tags could also be affected. To increase the affinity to the column and later separation of different species, the His6-tag was extended to a His12-tag, which increases the number of ligands that can bind to the column and the $Ni^{2+}$-NTA column was replaced with a $Cu^{2+}$-NTA column, as $Cu^{2+}$ has a higher binding affinity towards His-tags than $Ni^{2+}$.[262] To produce the Ibio-His-tagged streptavidin, streptavidin (namely S, 30 µM) was incubated with the Ibio-His-Tag (iminobiotin-$(His)_{12}$= 90 µM) for 15 min. Additionally, to simplify the procedure, the first biotin conjugated molecule, atto-565-biotin (namely A, 50 µM), was subsequently added to the reaction mixture and incubated for 15 min before the separation of different species ($S(Ibio\text{-}His\text{-}Tag)_1A_3$, $S(Ibio\text{-}His\text{-}Tag)_2A_2$, $S(Ibio\text{-}His\text{-}Tag)_3A_1$, $S(Ibio\text{-}His\text{-}Tag)_4$) over the $Cu^{2+}$-NTA column using an imidazole gradient. In the chromatogram, four peaks were

visible in the absorbance channel at 280 nm, but only the first three absorbed at 563 nm, where atto-565 absorbs (**Figure 5.5a**, relative integrated areas at 280 nm: 5.1% first peak, 42.6% second peak, 26.7% 3rd peak and 25.6% 4th peak). To confirm the identity of the species in each peak, first the Ibio-His-Tag was removed by lowering the pH to 3.5 and by dialysis, and subsequently the streptavidin species were titrated with biotin-5-fluorescein as described above (**Figure 5.5b-f**). The streptavidin species in the first peak reacted with 1 equivalent of biotin-5-fluorescein and was therefore identified as $SA_3$, which carried 1 Ibio-His-Tag before the acidification. Similarly, the species in the following peaks reacted with 2, 3 and 4 equivalents of biotin-5-fluorescein, respectively, and were identified as $SA_2$ (two open biotin sites), $SA_1$ (three open biotin sites) and S (four open biotin sites). Moreover, this assignment was also supported the relative absorbance of the conjugates in the UV-vis at 280 nm where streptavidin and atto-565 absorb and 532 nm where only atto-565 absorbs (**Figure 5.6a**). Using the Ibio-His-Tag, we were able to prepare fluorescently labeled mono- ($SA_3$), di- ($SA_2$) and tri- ($SA_1$) valent streptavidins without genetic manipulation. The atto-565-biotin used in this protocol can easily be replaced by another biotin conjugated molecule of choice. The straightforward preparation of these functionalized streptavidin derivatives with defined valences for the introduction of a second biotin coupled molecule offers us a new domain in which to expand and develop the many applications of biotin-streptavidin chemistry.

a)

| | $A_{280}$ | $\varepsilon_{280}$ ($M^{-1}$ $cm^{-1}$) | $C_{280}$ (µM) | $A_{532}$ | $\varepsilon_{532}$ ($M^{-1}$ $cm^{-1}$) | $C_{532}$ (µM) |
|---|---|---|---|---|---|---|
| **$SA_1$** | 0.0653 | 78060 | 8.37 | 0.0801 | 91835 | 8.71 |
| **$SA_2$** | 0.0664 | 114794 | 5.78 | 0.1108 | 183670 | 5.99 |
| **$SA_3$** | 0.1296 | 151528 | 8.55 | 0.2243 | 275505 | 8.14 |

b)

| | #A | Cons. (nM) | Fluorescence | Fluorescence / nM | Relative fluorescence brightness |
|---|---|---|---|---|---|
| **$SA_1F_3$** | 1 | 466 | 2200 | 4.721 | 1 |
| **$SA_2F_2$** | 2 | 378 | 2414 | 6.386 | 1.353 |
| **$SA_3F_1$** | 3 | 319 | 2927 | 9.176 | 1.944 |

**Figure 5.6** (a) The concentrations of $SA_1$, $SA_2$ and $SA_3$ were calculated based on the extinction coefficients of pure streptavidin (41326 $M^{-1}$ $cm^{-1}$ at 280 nm) and atto-565-biotin (36734 $M^{-1}$ $cm^{-1}$ at 280 nm and 91835 $M^{-1}$ $cm^{-1}$ at 532 nm) and the stoichiometry of the streptavidin conjugate. Light path= 1 mm, $\varepsilon_{280}$ ($SA_n$) = $\varepsilon_{280}$ (S) + n x $\varepsilon_{280}$ (A). $\varepsilon_{532}$ ($SA_n$) = n x $\varepsilon_{532}$ (A). The concentrations determined based on the absorbance at 280 nm and 532 nm were in agreement confirming the assumed stoichiometry of the $SA_{1-3}$. (b) The relative fluorescence brightness's of $SA_1F_3$, $SA_2F_2$ and $SA_3F_1$ were measured in solution and used to normalize the fluorescence intensities measured in confocal images for quantification in Figure 5.10g.

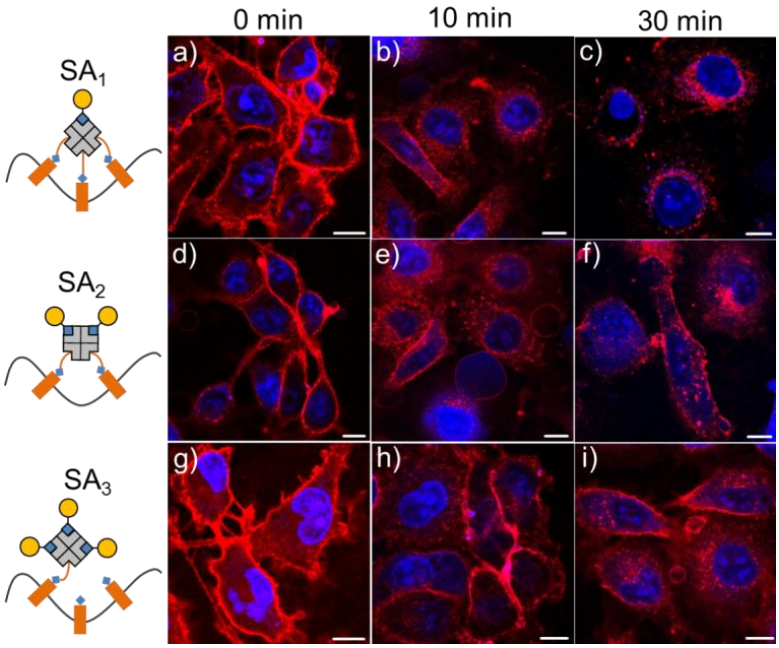


**Figure 5.7** Confocal microscopy images of biotinylated cell-surface proteins using sulfo-NHS-LC-biotin which were fluorescently labelled with trivalent ($SA_1$) (a-c), divalent ($SA_2$) (d-f) and monovalent ($SA_3$) (g-i) streptavidin-atto-565-biotin conjugates. Artificial protein clustering induced by trivalent ($SA_1$) and divalent ($SA_2$) conjugated results in protein internalization over time but not the monovalent ($SA_3$) conjugate. Cell nuclei were stained with TO-PRO-3. Scale bars are 10 μm.

One area where fluorescently labelled monovalent streptavidins are especially useful is in the imaging of biotinylated cell surface molecules. Unlike monovalent streptavidins, multivalent streptavidins lead to artificial clustering of the biotinylated surface molecules, resulting in altered biological response and cell uptake. Given this, the atto-565-biotin labelled monovalent streptavidin $SA_3$ described above is ideal for the visualization of biotinylated cell surface molecules. For this purpose, the cell membranes of MDA-MB-231 cells were first randomly biotinylated using sulfo-NHS-LC-biotin[163] and subsequently the cell membranes were labeled with $SA_3$, $SA_2$ or $SA_1$, which was visible under the confocal microscope (**Figure 5.7**). However, the fluorescence staining appeared different for different atto-565-biotin-streptavidin conjugates over time, as membrane proteins quickly internalize when they are cross-linked.[161, 163] The cells labeled with monovalent $SA_3$ were stained at the membrane's periphery and even after 30 minutes hardly any labeled protein was internalized. On the other hand, cells incubated with divalent $SA_2$ and trivalent $SA_1$ showed significant protein internalization after just 10 minutes, where this effect was more pronounced for $SA_1$. The conclusions were also supported quantitatively based on the intracellular fluorescence intensity (**Figure 5.8a**). The fluorescently labelled monovalent streptavidin, $SA_3$, can actually

be used at concentrations as low as 0.05 µM for clearly cell surface labelling with high sensitivity (**Figure 5.9, 5.8b**). Thus, it is a good alternative to current monovalent streptavidins, which require an additional labelling step with the fluorophore and are only labelled statistically.

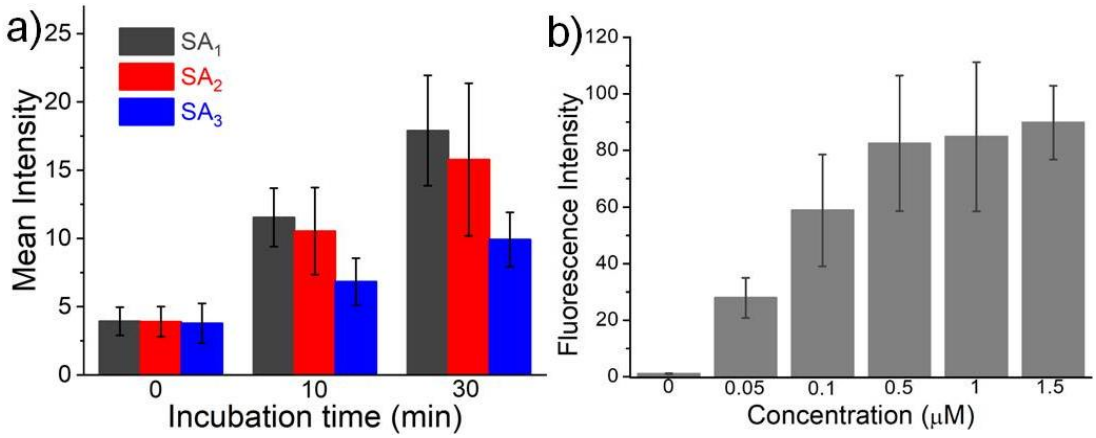


**Figure 5.8** (a) Intracellular fluorescence intensity of cells with biotinylated surface proteins and labelled with different streptavidin conjugates. 25 cells were analysed per data point. The error bars represent the standard error. (b) Fluorescence intensity at the cell membrane of cells in Figure 5.9. For each concentration 15 cells were analysed. The error bars represent the standard error.

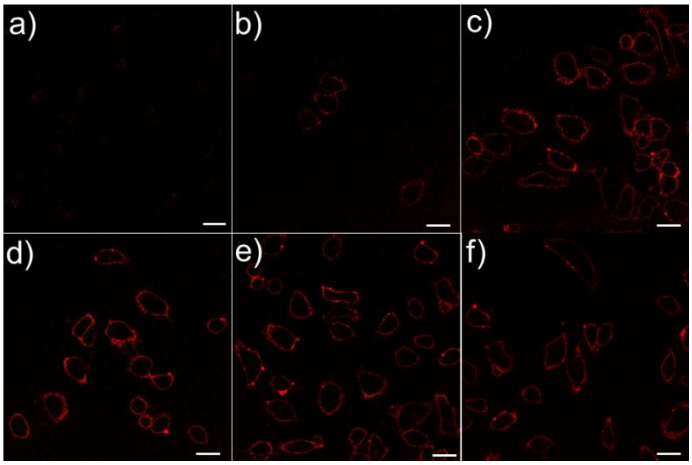


**Figure 5.9** (a) Fluorescent images in the atto-565 channel of cells with biotinylated surfaces, which were incubated with different concentrations of $SA_3$. a) 0 µM b) 0.05 µM. c) 0.1 µM. d) 0.5 µM. e) 1.0 µM and f) 1.5 µM. Scale bar: 25 µm.

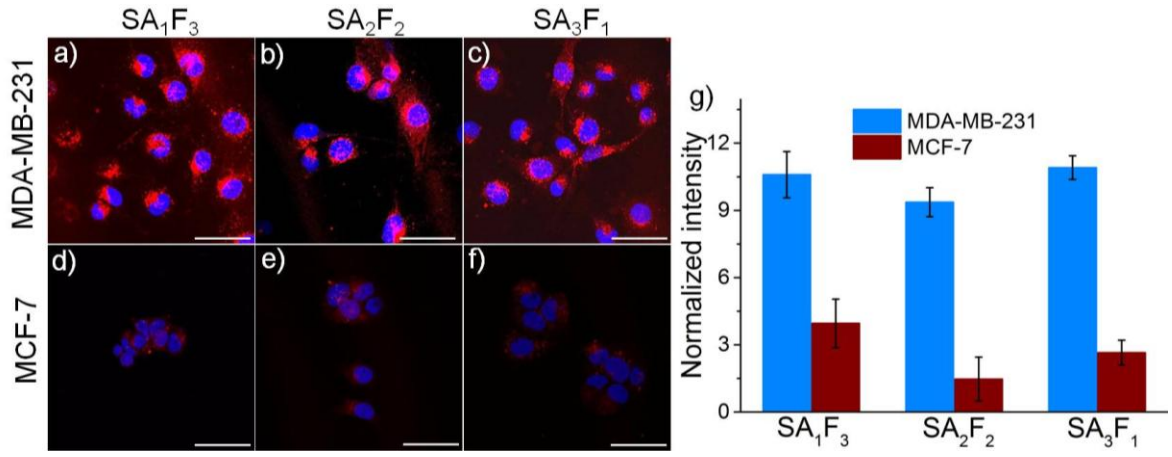


**Figure 5.10** Confocal microscopy images of folate-receptor positive MDA-MB-231 cells (a-c) and folate-receptor negative MCF-7 cells (d-f) incubated with atto-565 (A) (shown red) labelled folic acid (F) streptavidin conjugates with different stoichiometries. Cells were incubated with 1 μM $SA_1F_3$ (a, d), $SA_2F_2$ (b, e) or $SA_3F_1$ (c, f) in RPMI-1640 (no folic acid) medium for 4 h at 37 °C. Cell nuclei were stained with DAPI (shown blue). Scale bars are 50 μm. (g) The fluorescence intensities of different streptavidin conjugates in MDA-MB-231 and MCF-7 cells, normalized to the relative brightness's of the conjugates. The fluorescent intensity for all streptavidin conjugates is higher in MDA-MB-231 cells than in MCF-7 cells but increasing numbers of folic acid in the conjugates do not result in higher uptake.

The open biotin binding pockets in the fluorescently labelled streptavidins can also be used to introduce a second functionality with precise molecular stoichiometry. For instance, we added folic acid, an active and selective targeting molecule for aggressive cancer cells that overexpress the folic acid receptor on their surfaces.[263-265] The folic acid and atto-565 labelled streptavidins allowed us to determine whether the number of folic acid groups per molecule impact cellular uptake by using the signal from the fluorescent label. For this purpose, pure $SA_3$, $SA_2$ and $SA_1$ were each incubated first with excess folic acid-PEG-biotin (F) for 20 min and then excess F was removed by dialysis. The final conjugates, $SA_3F_1$, $SA_2F_2$ and $SA_1F_3$ were tested on two different cell lines: folate receptor-positive MDA-MB-231 and folate receptor-negative MCF-7. After 4 h of incubation the fluorescence signal from the atto-565 was much brighter in the MDA-MB-231 cells than in the MCF-7 cells (**Figure 5.10a**). The uptake was clearly due to the folic acid as cells incubated with $SA_1$, $SA_2$ and $SA_3$ were not significantly fluorescent (**Figure 5.11**). For quantification, the fluorescence intensities of $SA_1F_3$, $SA_2F_2$ and $SA_3F_1$ in both MDA-MB-231 and MCF-7 cells were measured and normalized to the relative brightness of the streptavidin-atto-565 species (**Figure 5.10b, 5.6b**). This analysis shows that all three streptavidin-folic acid conjugates were taken up equally

well by the folic acid receptor positive cell line MDA-MB-231 independent of the number of folic acids in its structure.

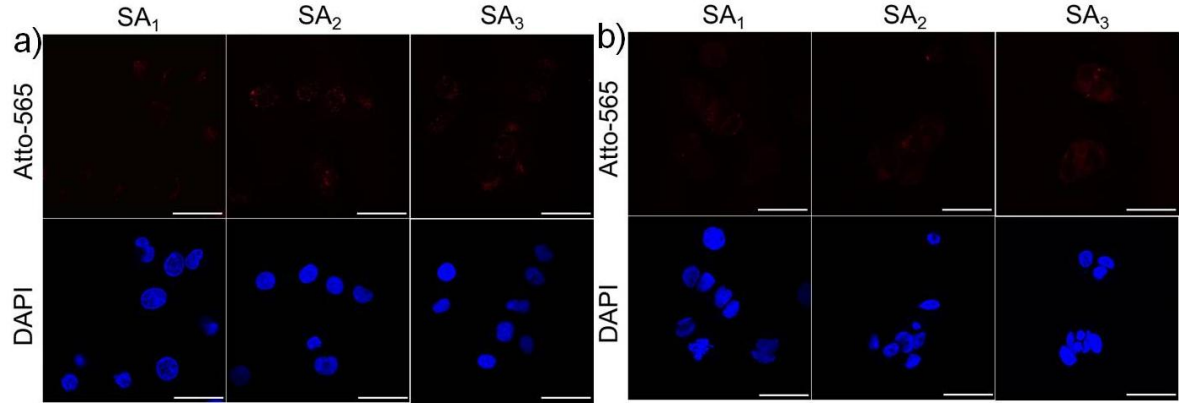


**Figure 5.11** (a) Confocal microscopy images of folate-receptor positive MDA-MB-231 cells incubated with atto-565 (A) (shown red) streptavidin conjugates with different stoichiometries. Cells were incubated with 1 µM $SA_1$, $SA_2$ or $SA_3$ with RPMI-1640 (no folic acid) medium for 4 h at 37 °C. Cell nuclei were stained with DAPI (shown blue). Scale bars are 50 µm. (b) Confocal microscopy images of folate-receptor negative MCF-7 cells incubated with atto-565 (A) (shown red) streptavidin conjugates with different stoichiometries. Cells were incubated with 1 µM $SA_1$, $SA_2$ or $SA_3$ with RPMI-1640 (no folic acid) medium for 4h at 37 °C. Cell nuclei were stained with DAPI (shown blue). Scale bars are 50 µm.

## 5.4 Conclusions

In summary, we demonstrated that the Bio-His-Tag and Ibio-His-Tag can both be used to prepare multifunctional streptavidin-biotin conjugates with precise stoichiometry and structure. This method, as demonstrated in two examples, can be widely applied and is highly adaptable. It is an ideal approach to answer questions in molecular biology and for biotechnological applications. We used fluorescently labeled monovalent ($SA_3$), divalent ($SA_2$) and trivalent ($SA_1$) streptavidin for imaging biotinylated cell surface molecules and investigated the importance of multivalent cell receptor interactions with folic acid in the cellular uptake and targeting ($SA_3F_1$, $SA_2F_2$ and $SA_1F_3$). The wide variety of commercially available biotinylated molecules ranging from small molecules and peptides to proteins, nucleic acids and antibodies, as well as the Bio-His-Tag and Ibio-His-Tag, all make this method extremely versatile and accessible. The potential diversity in precise streptavidin-biotin conjugates opens the door to building new bio- and nanostructures and will play a significant role in expanding the well-established status of streptavidin-biotin chemistry in biotechnology.[266-267]

# Chapter 6. Precise tetrafunctional streptavidin bioconjugates towards multifaceted drug delivery systems

## Copyright



## Aim

Precise macromolecules with multiple functionalities are required for many biomedical applications, especially drug delivery. But their preparation is a challenge due to many functionalities and the rich surface chemistries. This work provides a method to prepare stoichiometrically precise tetrafunctional streptavidin conjugates is presented with an exemplary structure combining exactly one fluorescent label, one cell targeting group, one nucleus penetrating peptide and one drug molecule. The systematic introduction of each functionality allows studying its effect on viability, targeting and efficacy, which improves our understanding on the essential features of drug delivery agents and of course enables optimization. Overall, such precise tetrafunctional streptavidin conjugates open the door for combinatorial multifunctional libraries of exact streptavidin taking advantage of a wide repertoire of biotinylated molecules (proteins, peptides, antibodies, small molecules, lipids and nucleic acids) based on the well-established biotin-streptavidin interaction.

## 6.1 Abstract

The preparation of precise macromolecules with multiple functionalities remains a challenge in drug delivery. Here, a method to prepare stoichiometrically precise tetrafunctional streptavidin conjugates is presented with an exemplary structure combining exactly one fluorescent label, one cell targeting group, one nucleus penetrating peptide and one drug molecule.

## 6.2 Introduction

In drug delivery, the availability of macromolecules combining several different functionalities is often crucial to impart bioactivity, traceability and labelling. Beside the cytotoxicity of a drug designed as an anti-cancer agent, its targeted delivery to the right cell type and intracellular location as well as the real-time monitoring of the therapeutic are all desired features to increase the efficacy and safety.[268-269] Yet, combining multiple functional groups in a single macromolecule is non-trivial.[170, 270-273] Multifunctionalization has mostly been realized with nanocarriers[274] that are large enough to harbor many molecules but with limited control of the number of functional groups that are incorporated. These have been decorated with targeting ligands like antibodies[275] or peptides[276] and loaded with known small molecule drugs and imaging probes.[277-278] Macromolecular drugs with many functionalities are far less common, due to the challenges in synthesis, solubility and preserving the activity. Even more important, general methods for the straightforward optimization of multifunctional molecules that would allow for efficient design and screening are missing.

Multivalent protein assemblies, which provide the advantages of simple production, monodisperse size and structure,[167] have been developed for specific targeting and delivery. In particular, streptavidin with its four independent biotin binding pockets, extraordinarily high affinity ($K_d=10^{-14}$) and low exchange rates is an attractive scaffold.[161] Moreover, the mature biotin labelling technology provides a large repertoire of biotinylated molecules with targeting, sensing, diagnostic and therapeutic entities. Yet, it is still challenging to produce structurally defined streptavidin conjugates with more than one type of biotin labeled molecule and precise stoichiometry. More precisely, when four different biotinylated molecules are mixed with streptavidin, a statistical mixture forms where only 1 of the 35 possible products is the desired tetrafunctional one. It is challenging if not impossible to separate the desired product, which contains all four functional labels from the mixture of

defective structures and would result in extremely low yield. So far, only precise streptavidin conjugates with four different single stranded DNA have been prepared, which limits the type of functional groups in the macromolecular assembly.[170] Other approaches to deal with multivalency or desymmetrization of streptavidin include the development of monovalent streptavidin to specifically label one receptor at the cell surface without artificially inducing clustering[161] and to use solid support-based assemblies to sterically block some of the biotin binding sites.[267] Nevertheless, incorporating more than two functional entities without restriction on one streptavidin in a controlled fashion is still elusive.

Herein, we describe a general method to prepare stoichiometrically exact tetrafunctional streptavidin conjugates offering great flexibility in conjugated molecules. For example, we combined a fluorescent label (atto-565-biotin), a cell type specific targeting group (folic acid-biotin), a nuclear localization peptide (nucleus penetrating peptide-biotin)[279] and an anti-cancer drug (doxorubicin-biotin) within one conjugate, which allowed for a more specific and efficient cellular toxicity towards cancer cells and its simultaneous detection.

### 6.3 Results and Discussion

The assembly of precise tetrafunctional streptavidin conjugates relies on a peptide with an iminobiotin and 12 histidines, named the Ibio-His-tag. First of all, the Ibio-His-tag allows separating streptavidin (S) conjugates with different numbers of bound Ibio-His-tags on a $Cu^{2+}$-NTA column using an imidazole elution gradient ($S(Ibio\text{-}His\text{-}tag)_{1\text{-}4}$).[262] Secondly, the pH-dependent binding of iminobiotin to streptavidin[159] allows releasing the Ibio-His-tag from the conjugates by lowering the pH to 3.5 and linking a biotinylated molecules with precise stoichiometry. Previously reports have shown the preparation of monofunctional streptavidin conjugates with precise stoichiometries and different vacancies using this method.[280]

Building on this chemistry and repeating it over multiple cycles, we assemble in a step by step fashion up to four biotinylated molecules; in this case various fluorophores, on a single streptavidin with exact control over the stoichiometry ($SA_1B_1C_1D_1$, S: streptavidin, A: atto-565-biotin, B: atto-425-biotin, C: atto-665-biotin, D: biotin-5-fluorescein) (**Figure 6.1**). To introduce the second biotinylated molecule, we started with a mono atto-565 labeled streptavidin, $SA_1$, with three available biotin binding pockets, which was prepared as described previously.[280] When $SA_1$ (1 μM) was incubated with a secondbiotinylated molecule, atto-425-biotin (B = 2 μM) and the Ibio-His-tag (2 μM), a statistical mixture composed of

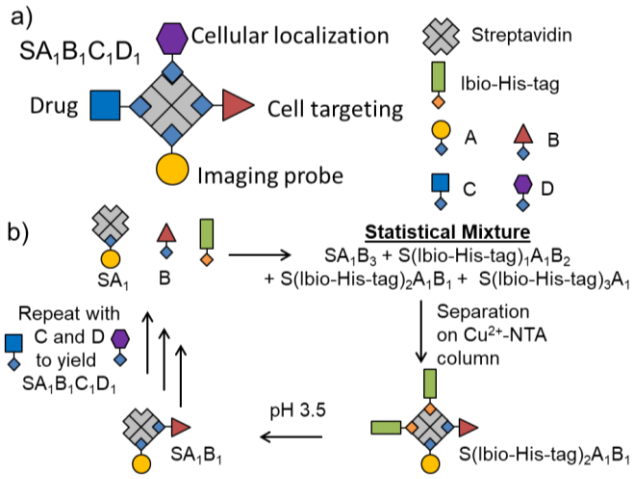


**Figure 6.1** Strategy for preparing tetrafunctional streptavidin-biotin conjugates. a) Four different biotinylated molecules for therapeutic activity, cell targeting, intracellular localization and theranostics are combined into one streptavidin conjugate. b) Each of the functionalities is added one by one going through cycles of forming statistical mixtures of products containing different numbers of Ibio-His-tags, which are separated on a $Cu^{2+}$-NTA column. The biotin binding pockets made accessible again at lower pH, allowing the repetition of the synthesis and purification cycles.

$SA_1B_3$, S(Ibio-His-tag)$_1A_1B_2$, S(Ibio-His-tag)$_2A_1B_1$ and S(Ibio-His-tag)$_3A_1$ formed. Then, the mixture separated on a $Cu^{2+}$-NTA agarose column, where conjugate without the tag, $SA_1B_3$, was washed off and species bearing higher numbers of tag eluted at higher imidazole concentrations. In the chromatogram, three peaks with an absorbance typical for atto-565 (A) at 563 nm were observed, but only the first two absorbed at 436 nm typical for atto-425 (B) (**Figure 6.2a**). Thus, the peaks with increasing imidazole concentration were assigned as S(Ibio-His-tag)$_1A_1B_2$, S(Ibio-His-tag)$_2A_1B_1$ and S(Ibio-His-tag)$_3A_1$, respectively.

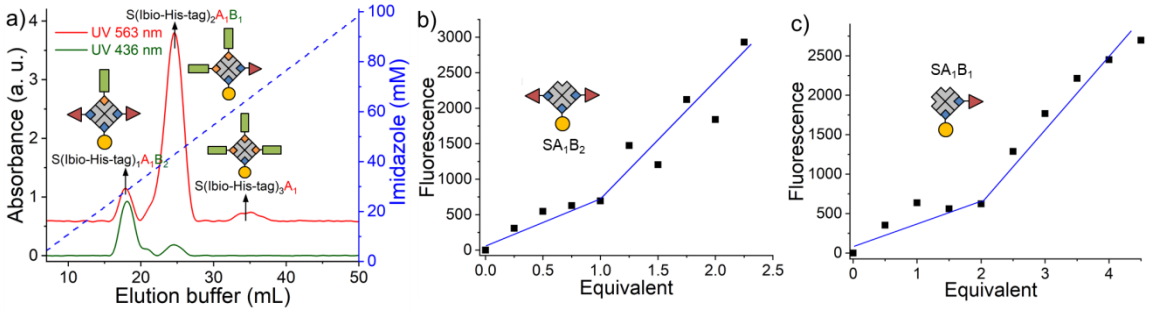


**Figure 6.2** Preparation and characterization of difunctional streptavidin conjugates. (a) Chromatogram of the reaction mixture of $SA_1$, atto-425-biotin and Ibio-His-tag. 1st peak: S(Ibio-His-tag)$_1A_1B_2$ (27.8 mM imidazole, area 9.7%), 2nd peak: S(Ibio-His-tag)$_2A_1B_1$ (43.6 mM imidazole, area 85.2%), 3rd peak: S(Ibio-His-tag)$_3A_1$ (63.2 mM imidazole, area 5.1%). $SA_1B_3$ (area 2.5%) washed off without imidazole. The accessible biotin binding pockets of the species in the (b) 1st and (c) 2nd peak were titrated with biotin-5-fluorescein, which is quenched upon streptavidin binding. S: streptavidin, A: atto-565-biotin, B: atto-425-biotin.

To confirm the identity of the species, first the Ibio-His-tag was removed at lowered pH to yield well defined difunctionalized streptavidin conjugates with available biotin binding pockets, $SA_1B_2$ and $SA_1B_1$. Subsequently, the number of accessible biotin binding pockets was determined through the titration with biotin-5-fluorescein, which is quenched upon binding to streptavidin (**Figure 6.2b, 6.2c**).[260] The streptavidin conjugate in the first peak, which carried one Ibio-His-tag before the acidification, $SA_1B_2$, reacted with one equivalent of biotin-5-fluorescein. The species collected in the second peak, $SA_1B_1$, reacted with two equivalents of biotin-5-fluorescein.

The third biotinylated molecule was added onto the $SA_1B_1$ bioconjugate repeating the same protocol. Shortly, $SA_1B_1$ (A: atto-565-biotin, B: atto-425-biotin, 1 µM) was incubated with atto-665-biotin (C, 1.5 µM) and Ibio-His-tag (1.5 µM) and the reaction products were separated on a $Cu^{2+}$-NTA agarose column. While the specie without the biotin tag, $SA_1B_1C_2$, did not bind to the column, two species eluted at different imidazole concentrations (**Figure 6.3a**). The first peak was assigned as S(Ibio-His-tag)$_1$$A_1B_1C_1$ because it only has one Ibio-His-tag and was the only species to absorb at 663 nm typical for atto-665 (C). The second peak at higher concentrations, was identified as S(Ibio-His-tag)$_2$$A_1B_1$ since it has two tags.

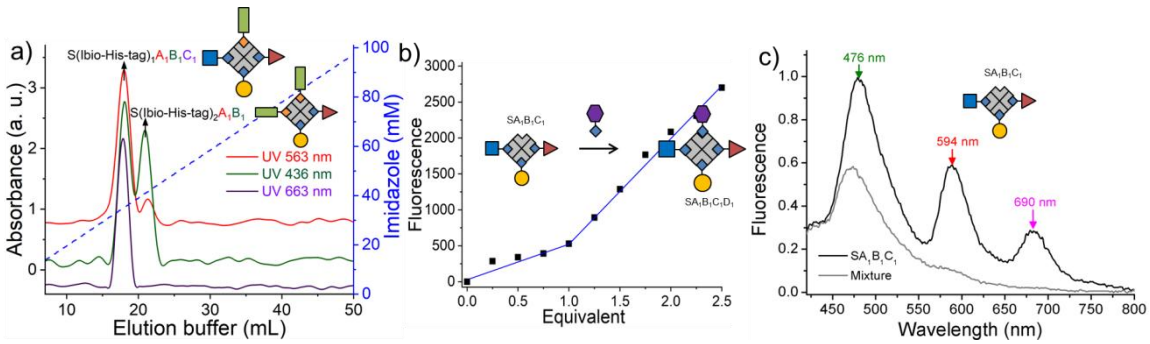


**Figure 6.3** Preparation and characterization of tri- and tetra-functional streptavidin conjugates. (a) Chromatogram of the reaction mixture of $SA_1B_1$, atto-665-biotin and Ibio-His-tag. 1st peak: S(Ibio-His-tag)$_1$$A_1B_1C_1$ (34.1 mM imidazole, area 84.5%), 2nd peak: S(Ibio-His-tag)$_2$$A_1B_1$ (41.5 mM imidazole, area 16.5%). $SA_1B_1C_2$ (area 2.3%) washed off without imidazole. (b) $SA_1B_1C_1$ required one equivalent of the biotin-5-fluorescein in the titration to saturate the biotin binding site, forming the tetrafunctional streptavidin conjugate, $SA_1B_1C_1D_1$. (c) Fluorescence emission spectrum ($\lambda_{Ex}$= 400 nm) of the precise $SA_1B_1C_1$ and a statistical mixture of streptavidin conjugates (S mixed with 1 equivalent of A, B and C). S: streptavidin, A: atto-565-biotin, B: atto-425-biotin, C: atto-665-biotin, D: biotin-5-fluorescein.

Finally, to form an exact tetrafunctional streptavidin conjugate, $SA_1B_1C_1D_1$, it is sufficient to remove the Ibio-His-tag from S(Ibio-His-tag)$_1$$A_1B_1C_1$ at lowered pH and add one equivalent of the desired biotinylated molecule. When the above prepared $SA_1B_1C_1$ was titrated with

biotin-5-fluorescein (D), it reacted with one equivalent yielding $SA_1B_1C_1D_1$ (**Figure 6.3b**). This experiment confirms the structure of the $SA_1B_1C_1$ with one open biotin binding pocket.

The importance of forming precise multifunctional streptavidins and not statistical mixtures was already apparent from the Förster resonance energy transfer (FRET) in $SA_1B_1C_1$ (A: atto-565-biotin, B: atto-425-biotin, C: atto-665-biotin). In this stoichiometrically precise conjugate with three different fluorophores, which cover different parts of the visible spectrum (**Figure 6.4a**), are in close proximity. Consequently, when we excited the atto-425 at 400 nm, there were three emission peaks at 476, 594 and 690 nm for atto-425, atto-565 and atto-665, respectively (**Figure 6.3c**). On the other hand, when we formed a statistical mixture of conjugates by mixing one equivalent of each of the three fluorophores with streptavidin, there was only one peak at 476 nm upon excitation at 400 nm. Moreover, the characteristic UV-Vis absorbance peaks of the three fluorophores in $SA_1B_1C_1$ support the stoichiometry of the complex (A:B:C = 1.0:1.2:1.0) (**Figure 6.4b**).

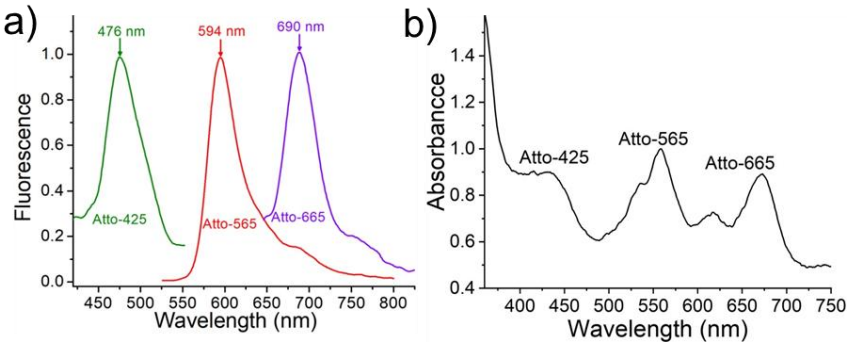


**Figure 6.4 (**a) Emission spectra of fluorescent conjugates (atto-425-biotin (excitation at 400 nm), atto-565-biotin (excitation at 505 nm) and atto-665-biotin (excitation at 625 nm)). (b) Absorbance spectrum of $SA_1B_1C_1$ (S: streptavidin, A: atto-565-biotin, B: atto-425-biotin, C: atto-665-biotin). The ratio of A:B:C was determined to be 1.0: 1.2: 1.0 based on the extinction coefficients of the pure A, B and C at 535 nm, 440 nm and 665 nm.

Next, we set out to combine four functionalities in one streptavidin conjugate to underline the potential for designing cancer theranostics. For this purpose, integrated the following functionalities within a single macromolecule: i) atto-565-biotin (A) as a fluorescent label for tracking the fate of the conjugates, ii) folic acid-PEG-biotin (F) for selective targeting of folic acid receptor positive cancer cells such triple negative breast cancer cells (MDA-MB-231),[265] iii) doxorubicin-biotin (D, **Figure 6.5**) as a broadly applied anti-cancer drug and iv) a nucleus penetrating peptide-biotin (C, **Figure 6.6**) for the targeted delivery of doxorubicin to the relevant subcellular compartment.[281] Each of these biotinylated molecules was added

sequentially according to the above order following the same method as described above (**Figure 6.7** and **6.8**).

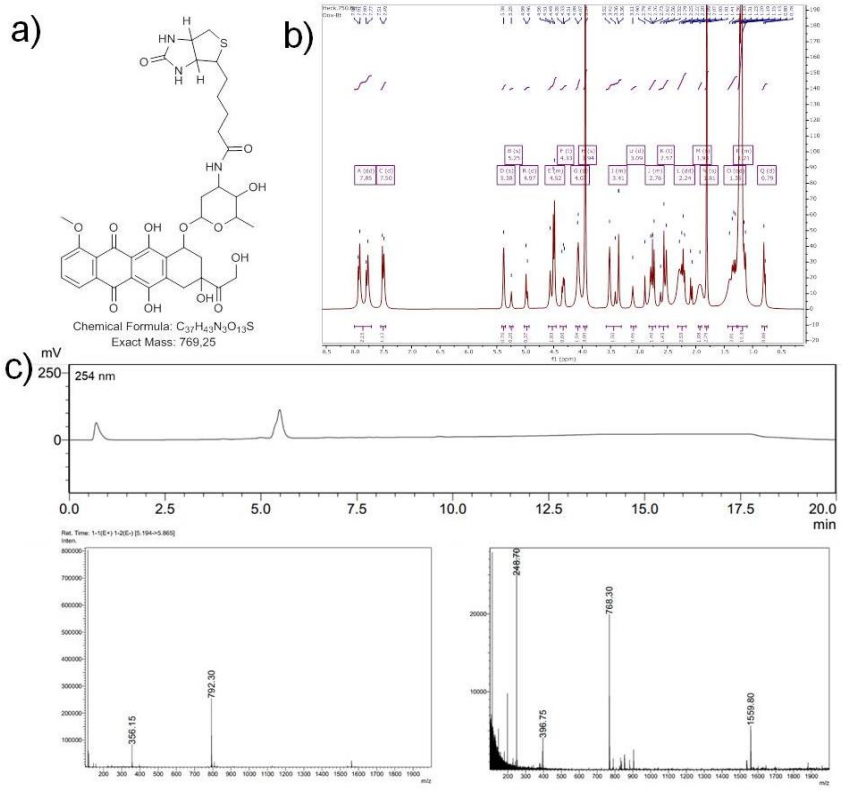


**Figure 6.5 (**a) The chemical structure of doxorubicin-biotin. (b) $^{1}$H NMR of doxorubicin-biotin (MeOD-d4, 300 MHz). (c) LC-Spectrum, $T_R$= 0.75 DMF, $T_R$= 5.5 Doxorubicin-biotin. ESI(+) left and ESI (-) right.

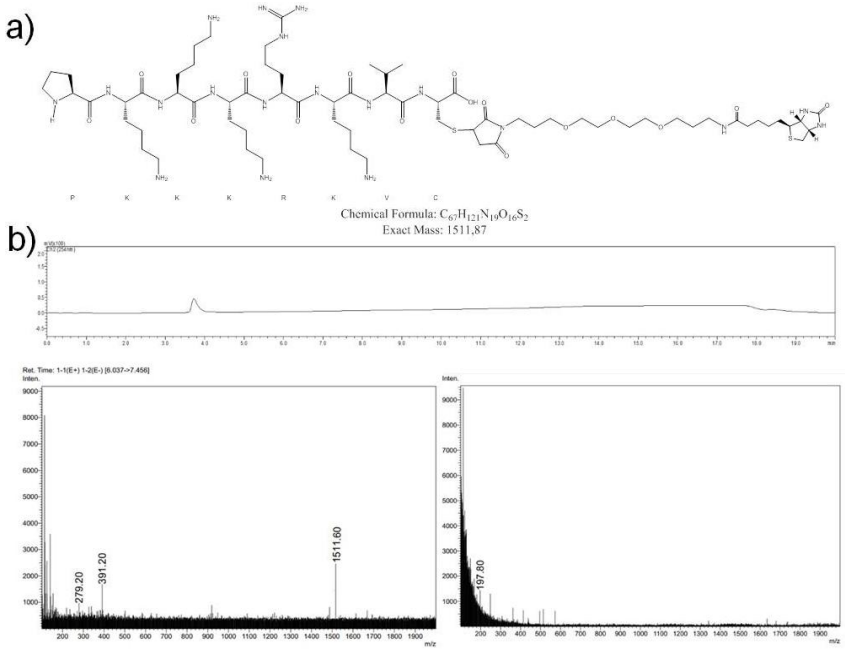


**Figure 6.6** (a) The chemical structure of biotin-NH-PKKKRKVC-COOH. (b) LC-Spectrum, $T_R$= 3.91, Biotin-PKKKRKVC. ESI (+) left and ESI (-) right.

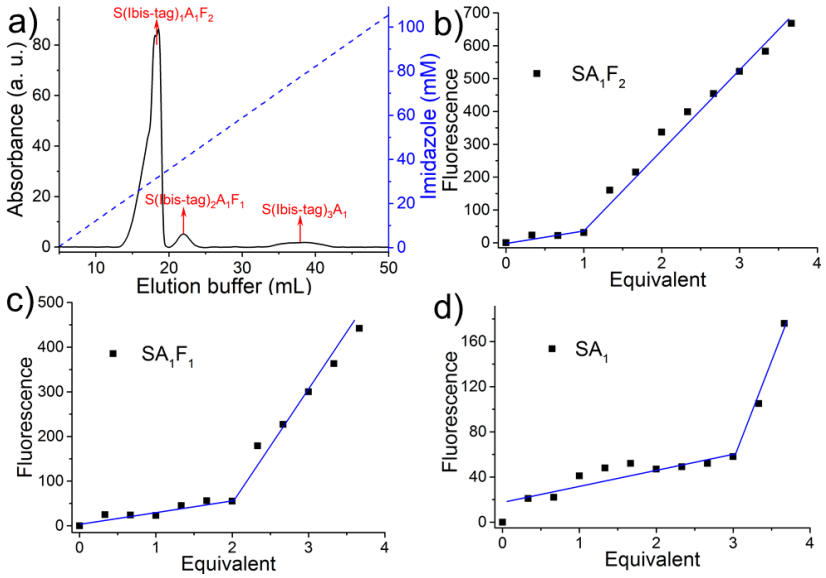


**Figure 6.7** Preparation and characterization of streptavidin conjugates with fluorophore and folic acid functionality, ($SA_1F_2$ and $SA_1F_1$). (a) A statistical mixture of products formed by mixing 10 µM $SA_1$ first with 20 µM Ibio-His-tag for 15 min, then 20 µM F (folic acid-biotin) was separated with a linear imidazole gradient on a $Cu^{2+}$-NTA column. S(Ibio-His-tag)$_1A_1F_2$ (the first peak) eluted at 28.4 mM imidazole, S(Ibio-His-tag)$_2A_1F_1$ (the second peak) eluted at 38.7 mM imidazole and S(Ibio-His-tag)$_3A_1$ (third peak) eluted at 74.2 mM imidazole. The Ibio-His-tag was removed from the different S(Ibio-His-tag)$_nA_1F_{3-n}$ species through acidification to yield the corresponding $SA_1F_{3-n}$. The open biotin binding pockets of $SA_1F_2$ (b), $SA_1F_1$ (c) and $SA_1$ (d) were titrated with biotin-5-fluorescein, where the fluorescence of biotin-5-fluorescein is quenched upon binding to streptavidin. The conjugates $SA_1F_2$, $SA_1F_1$ and $SA_1$ required one, two and three equivalents of biotin-5-fluorescein to saturate all biotin binding sites, respectively.

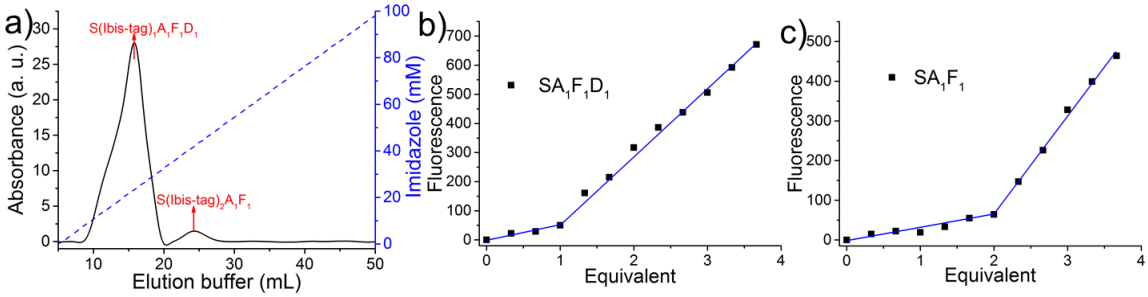


**Figure 6.8** Preparation and characterization of streptavidin conjugates with fluorophore, folic acid and doxorubicin functionality, ($SA_1F_1D_1$). (a) A statistical mixture of products formed by mixing 10 µM $SA_1F_1$ first with 15 µM Ibio-His-tag for 15 min, then 15 µM D (doxorubicin-biotin) was separated with a linear imidazole gradient on a $Cu^{2+}$-NTA column. S(Ibio-His-tag)$_1A_1F_1D_1$ (the first peak) eluted at 23.1 mM imidazole and S(Ibio-His-tag)$_2A_1F_1$ (the second peak) eluted at 41.5 mM imidazole. The Ibio-His-tag was removed from the different conjugates through acidification to yield the corresponding $SA_1F_1D_1$ and $SA_1F_1$. The open biotin binding pockets of $SA_1F_1D_1$ (b) and $SA_1F_1$ (c) were titrated with biotin-5-fluorescein, where the fluorescence of biotin-5-fluorescein is quenched upon binding to streptavidin. The conjugates $SA_1F_1D_1$ and $SA_1F_1$ required one and two equivalents of biotin-5-fluorescein to saturate all biotin binding sites, respectively.

Each of the biotinylated molecules within the tetrafunctional streptavidin conjugate should contribute to the overall function. For example, a conjugate without the doxorubicin should not be toxic to cancer cells and a conjugate without the folic acid should not to be selective for folate receptor positive cancer cells resulting in increased side effects. To demonstrate the added value of each functionality, we conducted a series of experiments using the tetrafunctional conjugate together with controls of conjugates.

The folic acid in the conjugate is supposed to increase the selectivity for cancer cell types, which are folate receptor positive. To demonstrate this point, the uptake of streptavidin conjugates with ($SA_1F_1$, $SA_1F_2$ and $SA_1F_3$) and without folic acid ($SA_1$) was evaluated in the folate receptor positive breast cancer cells, MDA-MB-231, and folate receptor-negative MCF-7 cells. After 4 h incubation the fluorescence signal from the atto-565 (A) in the conjugates showed that MDA-MB-231 cells incubated with different SAF conjugates were much brighter than MCF-7 cells (**Figure 6.9a** and **Figure 6.10**, **6.11**, **6.12a**). Moreover, the uptake in MDA-MB-231 cells was clearly due to the folic acid as cells incubated with $SA_1$ (A: atto-565-biotin) were not significantly fluorescent.

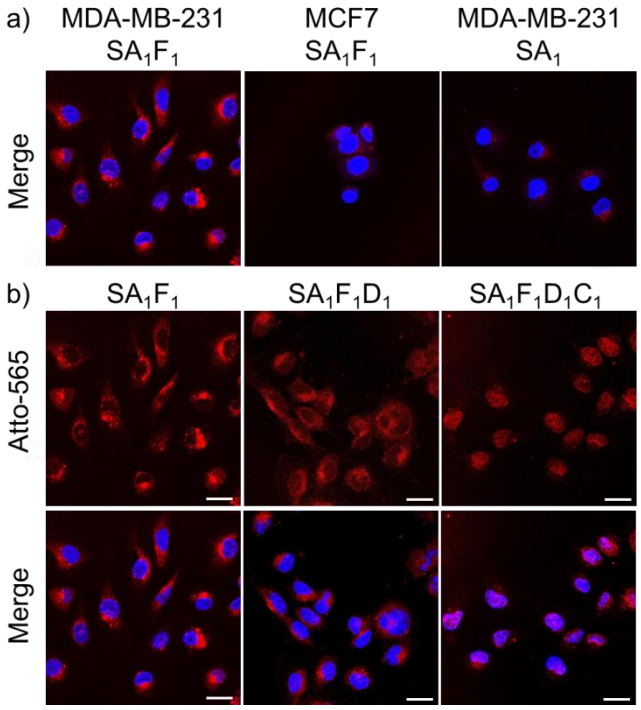


**Figure 6.9 (**a) Confocal microscopy images of MDA-MB-231 (folate receptor positive) and MCF-7 (folate receptor negative) cells incubated with $SA_1F_1$ and MDA-MD-231 cells incubated with $SA_1$. (b) MDA-MB-231 cells were incubated with $SA_1F_1$, $SA_1F_1D_1$ or $SA_1F_1D_1C_1$ in RPMI-1640 medium. Atto-565 fluorescence shown in red and nuclei stained with DAPI are shown in blue. Scale bars are 25 µm. S: streptavidin, A: atto-565-biotin, F: folic acid-biotin, D: doxorubicin-biotin, C: nucleus penetrating peptide-biotin.

Next, we evaluated the function of D (doxorubicin) and C (nucleus penetrating peptide) and their cooperativity in terms of the localization in the cells and cell toxicity. In particular, as doxorubicin stops DNA replication,[282] we aimed to deliver it into the cell nucleus using this peptide. We found that the trifunctional streptavidin conjugate $SA_1F_1D_1$ and tetrafunctional conjugate $SA_1F_1D_1C_1$ localized differently, when incubated with MDA-MB-231 cells (**Figure 6.9b)**. While $SA_1F_1D_1$ localized in the cytoplasm and was excluded from the nucleus, $SA_1F_1D_1C_1$ with the nucleus penetrating peptide localized in the nucleus, as observed under the confocal microscope. This finding was further supported through the quantification of the fluorescence signal within the nucleus of the cells (**Figure 6.12b**).

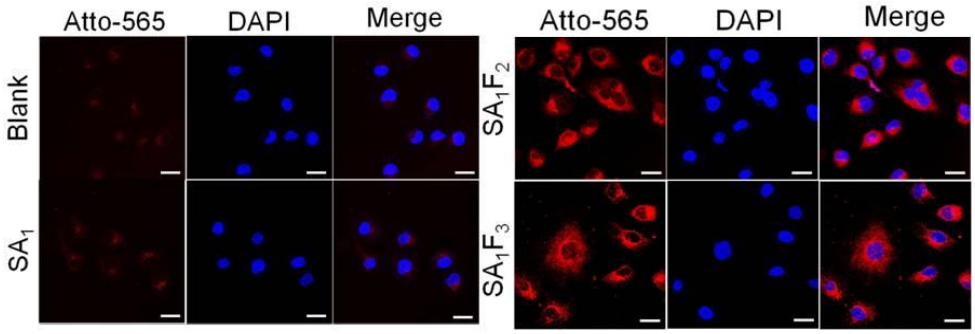


**Figure 6.10** Confocal microscopy images of MDA-MB-231 cells incubated with different streptavidin-biotin conjugates. Cells were incubated with 1 μM $SA_1$, $SA_1F_2$ or $SA_1F_3$ in RPMI-1640 medium for 4 h at 37 ℃, 5% $CO_2$. Atto-565 fluorescence from the conjugates is shown in red and cell nuclei stained with DAPI are shown blue. Cells not incubated with any streptavidin conjugate were used as blank. Scale bars are 25 μm.

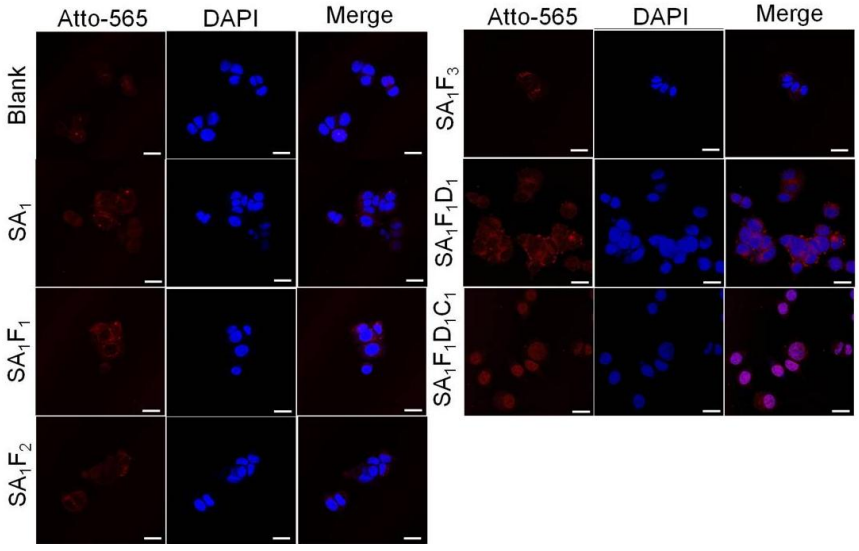


**Figure 6.11** Confocal microscopy images of MCF-7 cells incubated with multifunctional streptavidin-biotin conjugates. Cells were incubated with 1 μM $SA_1$, $SA_1F_2$ or $SA_1F_3$ in RPMI-1640 medium for 4 h at 37 ℃, 5% $CO_2$. Atto-565 fluorescence from the streptavidin conjugates is shown in red and cell nuclei stained with DAPI are shown blue. Cells not incubated with any streptavidin conjugate were used as blank. Scale bars are 25 μm.

Next, we tested the cell toxicity of the multifunctional streptavidin conjugates in MDA-MB-231 and MCF-7 cells. The cell viability as measured using the MTT test after 72 h, showed that the tetrafunctional $SA_1F_1D_1C_1$ was the most effective drug against the aggressive MDA-MB-231 cells (**Figure 6.13**). In $SA_1F_1D_1C_1$ and $SA_1F_1D_1$ the folic acid was responsible for the higher cell toxicity in MDA-MB-231 cells compared to MCF-7. While $SA_1F_1D_1C_1$ and $SA_1F_1D_1$ had $IC_{50}$ (50% inhibitory concentration) of 0.5 µM and 0.74 µM for MDA-MB-231 cells, respectively, their $IC_{50}$ for MCF-7 cells were higher at 2 µM and 2.62 µM, respectively. This amounts to a fourfold selectivity for MDA-MB-231 cells over MCF-7. Pure doxorubicin had no specificity and was almost equally cell toxic to both cell types (**Figure 6.14a**).

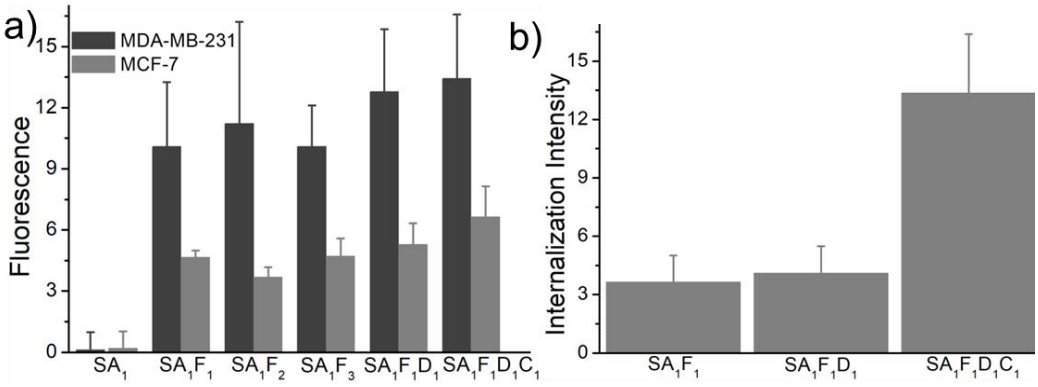


**Figure 6.12 (**a) Average intracellular fluorescence intensities of MDA-MB-231 and MCF-7 cells incubated by different streptavidin conjugates. The fluorescence in the atto-565 channel was measured by encircling single cells and measuring their average intensities and the background fluorescence determined from the blank sample was subtracted. (b) Average nuclear fluoresce intensity of different streptavidin conjugates in MDA-MB-231 cells. The extend of nuclear localization of the different streptavidin conjugates was quantified by measuring fluorescence intensity in the atto-565 channel inside the nucleus of MDA-MB-231 cell. 20 cells were analysed per sample and the error bars represent the standard error of the mean.

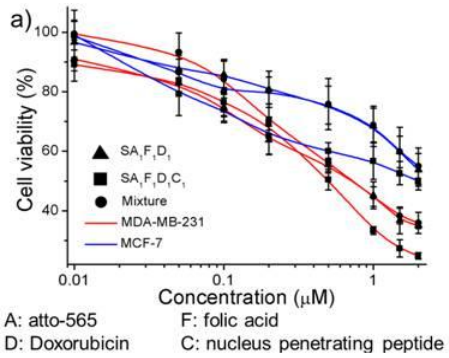


b)

| $IC_{50}$ (µM) | MDA-MB-231 | MCF-7 |
|---|---|---|
| $SA_1F_1D_1$ | 0.74 ±0.12 | 2.62 ±0.78 |
| $SA_1F_1D_1C_1$ | 0.50 ±0.08 | 2.00 ±0.80 |
| Mixture | 0.75 ±0.11 | 2.65 ±0.76 |

**Figure 6.13 (**a) Cell viability of MDA-MB-231 and MCF-7 cells were incubated with $SA_1F_1D_1$, $SA_1F_1D_1C_1$ and a statistical mixture of streptavidin conjugates (S was mixed with one equivalent of A, F, D and C) for 72 h, as measured using the MTT assay. (b) Table of the 50% inhibitory concentration ($IC_{50}$) different conjugates.

In $SA_1F_1D_1C_1$, the nucleus penetrating peptide, C, increased the delivery of doxorubicin, D, to the cell nucleus, which contributes to the higher final efficacy. As a result, $SA_1F_1D_1C_1$ had a lower $IC_{50}$ of 0.5 μM compared to $SA_1F_1D_1$, which had a $IC_{50}$ of 0.74 μM. The precise $SA_1F_1D_1$ conjugate also outperformed the statistical mixtures of conjugates (S mixed with one equivalent of A, F, D and C). In fact, the $SA_1F_1D_1C_1$ was 1.5 times more cell toxic than the statistical mixture of conjugates ($IC_{50}$ 0.75 μM). We also compared the viability under different samples at exact concentration of 0.5 μM, as shown in **Figure 6.14b**, results indicated that cells had the lowest viability (almost 48%) using $SA_1F_1D_1C_1$. Besides, we also confirmed that extra free folic acid will inhibit the function of our samples because the folate receptor on cell surface has been occupied. Overall, this data showed the added value of the precise tetrafunctional conjugate, which allowed the incorporation of each functionality for detection, targeting, subcellular localization and cell toxicity.

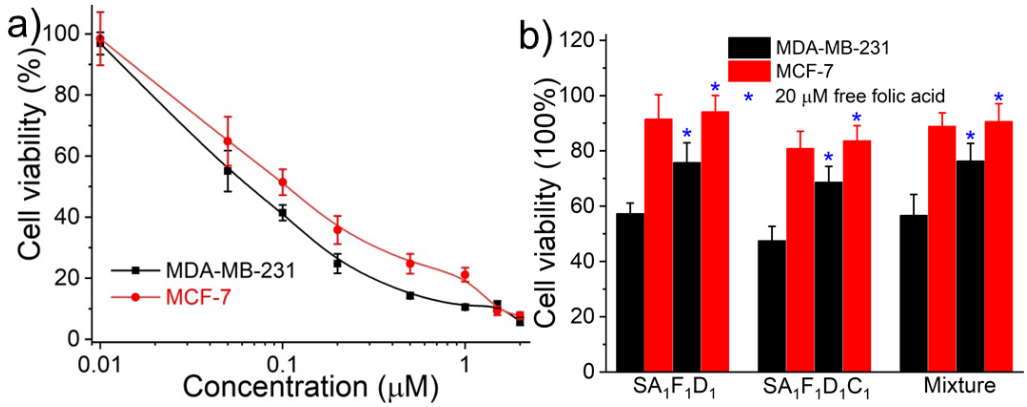


**Figure 6.14 (**a) Cytotoxicity of free doxorubicin-biotin against MDA-MB-231 and MCF-7 cell as measure with the MTT assay. Cells were incubated by RPMI-1640 medium containing 0.01, 0.05, 0.1, 0.2, 0.5, 1.0, 1.5, 2.0 μM of doxorubicin-biotin at 37 ℃, 5% $CO_2$ for 72 hours. The $IC_{50}$ is 0.07 μM and 0.10 μM for MDA-MB-231 and MCF-7 cells, respectively. Data is expressed as the percentages of viable cells relative to a sample without doxorubicin. (b) Cell viability of MDA-MB-231 and MCF-7 cells were incubated with 0.5 μM $SA_1F_1D_1$, 0.5 μM $SA_1F_1D_1C_1$ and a statistical mixture of streptavidin conjugates (0.5 μM, S was mixed with one equivalent of A, F, D and C) for 72 h with and without 20 μM extra free folic acid (shown with a blue star), as measured using the MTT assay. S: streptavidin, A: atto-565-biotin, F: folic acid-biotin, D: doxorubicin-biotin, C: nucleus penetrating peptide-biotin.

## 6.4 Conclusions

In summary, we demonstrated how stoichiometrically precise tetrafunctional streptavidin conjugates can be prepared to bring together multiple functionalities. In particular, we demonstrated how the delivery of an anti-cancer drug can be improved through the combination of a fluorescent, a cell specific targeting group, a nucleus penetrating peptide

and a cell toxic drug in a tetrafunctional streptavidin. The systematic introduction of each functionality allows studying its effect on viability, targeting and efficacy, which improves our understanding on the essential features of drug delivery agents and of course enables optimization. Especially, the cell nucleus penetrating peptide plays a vital role in delivery drug into where it functions. The precise tetrafunctional streptavidins also open the door to assembly combinatorial libraries of exact streptavidins taking advantage of a wide repertoire of biotinylated molecules (proteins, peptides, antibodies, small molecules, lipids and nucleic acids). Thus, our study plays a significant role in expanding the streptavidin-biotin chemistry in biotechnology, nanostructure assemblies and drug delivery.

# Chapter 7. Summary and outlook

The interaction between $Ni^{2+}$-NTA and His-tagged proteins can be widely used in many contexts from the design of smart minimal synthetic cells, photopatterning, controlled cell-matrix adhesion to the design of multifunctional streptavidin-biotin conjugates.

In the first part, a multiresponsive minimal synthetic cell was proposed and ATP production of the synthetic cell can be controlled by different environmental parameters. The modular adhesion unit, which is composed of the light and redox responsive protein interaction of iLID and Nano as well as the pH sensitive and metal ion mediated binding of protein His-tags to $Ni^{2+}$-NTA complexes, is able to sense and integrate four important stimuli: light, pH, oxidative stress and the presence of metal ions and regulate the adhesion to a substrate in response to them. The multistimuli responsive adhesion unit was further integrated with a light-driven ATP production module such that it is capable to adhere to substrates under environmental conditions that support its ATP production. If only one of the environmental parameters required for ATP production is not satisfied, the minimal synthetic cell detaches from the substrate. Thus the multistimuli responsive adhesion unit allows synthetic cells to self-position and carry out their functions.

In the second part, a layer-by-layer (LbL) protein system was first proposed to prepare precise micropatterns. The LbL assembly method for multiprotein films was based on the specific and multivalent interaction of $Ni^{2+}$-NTA groups and His-tagged proteins, which allowed us to achieve the oriented presentation of a His-tagged protein of interest. The green light cleavable protein CarH was then used as a light-sensitive building block for photolithography, which provided the desired high spatial and temporal remote control over the protein patterns in a noninvasive and biocompatible way. The LbL system is successfully used to produce complex patterns of different functional proteins including fluorescent proteins as well as the cell adhesion protein fibronectin. Furthermore, we proposed two approaches for the study of cell-matrix adhesions. One cell adhesion sequence, cRGD was masked by CarH in the first approach, which is GREEN-ON system. Then CarH was fused cRGD, the fused protein CarH-cRGD was directly used to regulate cell-matrix adhesions, which is GREEN-OFF system. All the methods allow for dynamical regulation of cell adhesions in space and time with high precision.

In the last part, a general approach to form multifunctional streptavidin conjugates with precise stoichiometries and number of open binding pockets was developed. This method

relies on an iminobiotin-polyhistidine tag, which allows separating streptavidin conjugates with different numbers of tags, and later reopening binding pockets at lowered pH to introduce a second functionality. Streptavidin (S) conjugates with one ($SA_1$), two ($SA_2$) or three ($SA_3$) copies of a biotinylated molecule (A) were produced, where the residual biotin binding pockets remain open to introduce a second biotin conjugated functionality. These precise fluorescent streptavidin conjugates was used to study for cell surface labeling and to investigate how the number of targeting ligands per conjugate affects cellular uptake. As a further step, a stoichiometrically precise tetrafunctional streptavidin conjugate was prepared based on this method. The tetrafunctional streptavidin conjugate with exactly one fluorescent label, one cell targeting group, one cell penetrating peptide and one drug demonstrates how each functionality contributed to overall efficacy of the drug.

The work presented here provides a potential approach for the study of chemical biology, synthetic biology and cell biology. The multistimuli responsive adhesion unit provides a new and modular element in producing smart and autonomous minimal synthetic cells that are able to position themselves in environments that meet their needs. The idea of using stimuli responsive adhesion elements to position cells is highly transferable and other interactions can be used to colonize different environments with synthetic cells. The LbL multiprotein films and GREEN-ON, GREEN-OFF system can be used for cell patterning, as a promising strategy to modulate cell-material interactions, and to design new biomaterials. The precise tetrafunctional streptavidins open the door to assembly combinatorial libraries of exact streptavidins taking advantage of a wide repertoire of biotinylated molecules (proteins, peptides, antibodies, small molecules, lipids and nucleic acids). Thus, this study plays a significant role in expanding the streptavidin-biotin chemistry in biotechnology, nanostructure assemblies and drug delivery.

# Chapter 8. Materials and method

## 8.1 Materials

### 8.1.1 Plasmids

The protein MiCy (Addgene plasmid # 54565), TurboRFP (Addgene plasmid # 54858), dKatushka (Addgene plasmid # 54775) and fibronectin (FN) (pET28a-ybbR-HIS-10FNIII(x4)-DocI, Addgene plasmid #58712) were acquired from Addgene. The CarH plasmid (Ampicillin resistance) was inserted into the vector pET-22b between the NdeI and BamHI cutting sites. BL21 (DE3) *E. coli* was purchased from New England Biolabs. The pQE-80L iLID (C530M) and pQE-80L MBPSspB Nano were gifts from Brian Kuhlman (Addgene plasmids # 60408 and # 60409, respectively). pQE-80L iLID (C530M) expresses iLID with an N-terminal His6-tag and pQE-80L MBP-SspB Nano expresses Nano with N-terminal His6-MBP-TEV tag (His6-MBP-TEV-Nano). His6-tagged TEV protease originated from the Wombacher Lab and was kindly provided as a glycerol stock of E. coli BL21 (DE3) co-transformed with pLysS (chloramphenicol) and pET N_TEV234 (kanamycin) plasmids. pET Biotin His6 mOrange LIC cloning vector (H6-mOrange) was a gift from Scott Gradia (Addgene plasmid # 29723; http://n2t.net/addgene:29723; RRID:Addgene_29723) and BirA in pET28a (w400-2) was a gift from Eric Campeau (Addgene plasmid # 26624; http://n2t.net/addgene:26624; RRID: Addgene_26624).

### 8.1.2 Other materials

4-arm PEG-Succinimidyl NHS ester (MW 10 kDa) was purchased from Creative PEG Works. $Ni^{2+}$-NTA column (HisTrap$^{TM}$ HP, column volume 5 mL) was purchased from GE Healthcare Life Sciences. $Ni^{2+}$-NTA functionalized polystyrene beads (2 μm) were purchased from Micromod Partikeltechnologie GmbH. SM-2 Bio-Beads derived from Bio-Rad were used to remove the detergent in the step of vesicle co-reconstitution and was extensively washed before usage. Luciferin/Luciferase reagent CLSII from Roche was prepared as a 10 times concentrated stock solution in water. Ultra-pure ADP was purchased from Cell Technology. Streptavidin (MW 53361 g/mol) was purchased from Cedarlane Laboratories. Bio-His-Tag (biotin-$(His)_6$, MW 1500 g/mol, sequence: biotin-GSGSGSHHHHHH) was synthesized by Peptide Specialty Laboratories GmbH and Ibio-His-Tag (MW 2322 g/mol, iminobiotin-$(His)_{12}$, sequence: iminobiotin-GSGSGSHHHHHHHHHHHH) were synthesized by Pepscan. Folic acid-PEG-biotin (MW 2000 g/mol) was purchased from Nanocs. Sulfo-

NHS-LC-biotin (MW 558 g/mol) was purchased from AdooQ Bbioscience. DMEM and RPMI-1640 without folic acid medium were purchased from Thermo Fisher Scientific. Cell nucleus location sequence (PKKKRKVC, MW 883 g/mol) purchased from PhtdPeptides Co Ltd. with 95% purity (Zhengzhou City, China). All organic solvents (acetonitrile ($CH_3CN$), chloroform ($CHCl_3$), dichlormethane (DCM), dimethylformamide (DMF), dimethyl sulfoxide (DMSO), methanol (MeOH) were obtained from Fisher Scientific and used without further purification (HPLC or analytical grades).

## 8.2 Methods

### 8.2.1 Protein preparation

Each protein expression plasmid was transformed into BL21(DE3) *E. coli* and plated on an LB-Agar plate with the appropriate antibiotic (50 μg/ml) at 37 ℃ overnight. A single colony was inoculated into 10 mL LB medium with the appropriate antibiotic (50 μg/mL) and incubated at 37 ℃, 250 rpm overnight. The overnight culture was transferred to 1 L LB medium with the appropriate antibiotic and incubated at 37 ℃, 250 rpm until the $OD_{600}$ = 0.6-0.8. Then protein expression was induced with 1 mM IPTG for CarH, CarH-RGD, iLID, Nano, TEV, FN, mOrange and with 1 g/L L-(+)-Arabinose for MiCy, TurboRFP and dKatushka, temperature was reduced to 18 ℃ and the cultures were incubated overnight at 250 rpm. Next day, the cultures were centrifuged at 6000 rpm, 4 ℃ for 8 min (Beckman Coulter Avanti J-26S XP, JA-10 rotor), supernatant was discarded and the bacteria pellet collected. Then the bacteria pellet was resuspended in 20 mL buffer A (50 mM Tris-HCl, 300 mM NaCl, pH 7.4) supplemented with 1 mM protease inhibitor phenylmethane sulfonyl fluoride (PMSF) and 1 mM DL-dithiothreitol (DTT). The bacteria were lysed by sonication and the lysate was cleared by centrifugation at 12000 rpm (Beckman Coulter Avanti J-26S XP, JA-25.50 rotor) for 30 min, followed by filtration through a 0.45 μm filter (ROTH, KH 55.1) twice. The lysate was loaded onto a 5 mL $Ni^{2+}$-NTA agarose column. The column was washed with 50 mL buffer C (Buffer A with 25 mM imidazole and 1 mM DTT) and the protein was eluted with 10 mL buffer B (Buffer A with 250 mM imidazole and 1 mM DTT). The purified proteins were dialyzed against 2 L buffer A with 1 mM DTT twice for 6 h.

Bacteriorhodopsin (bR) was isolated from Halobacterium salinarium (strain S9) as described by Oesterhelt and Stoeckenius. His-tagged E. coli $F_OF_1$-ATP synthase ($EF_OF_1$) was expressed from the plasmid pBWU13-βHis in the E. coli strain DK8 (ΔuncBEFHAGDC) and purified by $Ni^{2+}$-NTA affinity chromatography as previously described by Ishmukhametov.

### 8.2.2 Preparation of CarH and CarH-RGD tetramer

The purified CarH and CarH-RGD monomer was incubated with fivefold excess of Vitamin $B_{12}$ (Sigma-Aldrich, V2876) for 30 min in the dark to form the CarH tetramer. Unbound Vitamin $B_{12}$ was removed from the resulting CarH tetramer by size exclusion chromatography using a HiLoad™ 16/600, Superdex™ 200 pg size exclusion column. If necessary CarH tetramer was concentrated using a centrifugal filtration devices (10 kDa molecular weight cutoff).

### 8.2.3 Preparation of 4-arm-PEG-NTA

The $N_{\alpha}$,$N_{\alpha}$-Bis(carboxymethyl)-L-lysine hydrate (NTA-Lys) (0.24 mmol, 65 mg) was first dissolved into 10 ml MeOH and then 4-arm-PEG N-hydroxysuccinimide ester (4-arm-PEG-NHS, MW 10 kDa) (0.06 mmol, 600 mg) was added and dissolved. Then 60 µl 4-methylmorpholine was added to the solution as catalyst. After reacting for 6 h at room temperature, the product was precipitated by adding diethyl ether (100 mL) and vacuum dried.

### 8.2.4 Glass surface functionalized with PEG-$Ni^{2+}$-NTA

The glass surfaces were functionalized similarly as previously reported.[2] In short, glass slides (20 × 20 mm) were cleaned with freshly prepared Piranha solution (3:1 (v/v) concentrated $H_2SO_4$:$H_2O_2$ (30%)) for 1 h, rinsed 3 times with Milli-Q water and dried in an $N_2$ stream. For the PEGylation reaction, surfaces were immersed in a solution of $PEG_{3000}$-azide (10 mg $PEG_{3000}$-azide, MW = 3500 g/mol) and 200 µl dry triethylamine in dry toluene and kept at 80 ℃ overnight under a $N_2$ atmosphere. The surfaces were first washed with ethyl acetate for 5 min by sonication, then with methanol for 5 min by sonication and dried in a $N_2$ stream. The PEG-coated surfaces were incubated with 100 µl of reaction solution containing 100 mM L-ascorbic acid, 100 mM Tris HCl (pH 9.0), 150 µM of NTA-alkyne and 1 mM $CuSO_4$ in a moisture chamber for 2 h. The surfaces were incubated with the following solutions to obtain PEG-$Ni^{2+}$-NTA functionalized surfaces: (1) 50 mM EDTA (pH 7.4) for 5 min; (2) Buffer A twice for 5 min; (3) 0.1 M $NiCl_2$ in water for 5 min; (4) Buffer A for 5 min.

### 8.2.5 Protein immobilization on PEG-$Ni^{2+}$-NTA functionalized glass Surfaces

Afterward the surfaces were incubated with the following solutions to obtain the protein functionalized LbL substrates through NTA-$Ni^{2+}$-His tag interaction: (1) 1st layer: 5 µM purified protein for 30 min; (2) Buffer A for 10 min; (3) 25 µM 4-arm-PEG-NTA+100 µM $NiCl_2$ in Buffer A for 30 min; (4) Buffer A for 5 min; (5) 5 µM purified protein for 30 min

($2^{nd}$ protein layer); (6) Buffer A for 10 min. To generate subsequent protein layers step 3-6 were repeated to assemble the LbL protein film. Other proteins can also be immobilized on the glass surface using this method.

### 8.2.6 Metabolic Activity Test

The influence of light on the metabolic activity of cells was determined with the 3-(4,5-Dimethylthiozol-2-yl)-2,5-diphenaltetrazolium bromide (MTT) assay. Therefore, MCF-7 cells were seeded in a density of 50000 cells/$cm^2$ in a 96 well plate in 100 µL complete growth medium (DMEM + 10% FBS + 1% P/S). The cells were incubated at 37 ℃ exposed to green light (532 nm, Flora LED Module) at different intensities for 2 h. The control was kept meanwhile in the dark. Afterwards 75 µL medium per well were removed and 10 µL MTT (saturated solution in PBS) was added. The cells were incubated at 37 ℃ in dark for 4 h. 50 µL DMSO per well was added and incubated at room temperature in dark for 10 min. The absorption at 540 nm was measured with a Tecan plate reader. The lowest tested light intensity at 12.5 µM/$m^2$s was used in all cell experiments, to assure no influence of the cells.

### 8.2.7 Protein patterning

Substrates with LbL films with CarH in the $1^{st}$ and TurboRFP in the $2^{nd}$ layer were used for all protein patterning experiments. The logo of the Max Planck Society, the Minerva, was patterned on an inverted fluorescence microscope (DMi8, Leica) equipped with a 10x objective and a digital micromirror device (Mosaic, Andor) and illuminating for 1 min with 10% intensity of the 525 nm LED line. Line patterns of proteins were produced on the confocal laser scanning microscopy (Leica TCS SP8) equipped with an argon laser and 20x objective. Lines were projected onto the LbL film using 20% intensity of the 552 nm laser for 10 s. To demonstrate the temporal control, substrates were patterned in buffer A solution and after each patterning step imaged using 1% intensity of the 552 nm laser and 0.5 s exposure time. All other substrates were first fixed with 4% paraformaldehyde for 20 min, mounted in Mowiol-488 and then imaged using 1% intensity of the 552 nm laser and 1 s exposure time.

### 8.2.8 Quantification of cell adhesion

The PEG-$Ni^{2+}$-NTA coated glass surfaces were either functionalized with the FN or a CarH ($1^{st}$ layer)/ FN ($2^{nd}$ layer) LbL film. While one set of surfaces was illuminated with green light for 5 min (15 W), the other one was kept in the dark. A PEG-$Ni^{2+}$-NTA functionalized surface without protein functionalization was used as a negative control. The surfaces were

placed into the 6-well cell culture plates and were washed with phosphate buffered saline 1x (PBS 1x). Subsequently, $5\times10^4$ MDA-MB-231 cells were seeded per well in 2 ml Dulbecco's modified Eagle's medium (DMEM) (Gibco BRL) supplemented with heat inactivated fetal bovine serum (FBS, 10%) (Sigma Aldrich) and penicillin/streptomycin (P/S, 1%, Gibco BRL) and incubated at 37 ℃, 5% $CO_2$ for 4 h in the dark. After carefully washing the surfaces twice with PBS, the cells were fixed with 2% paraformaldehyde. The cells were mounted with Moviol-488 containg 1 μg/ml DAPI (Sigma Aldrich) for nucleus staining. Fluorescent images were acquired with an inverted fluorescence microscope (DMi8, Leica) in the DAPI channel with a 10x objective for an area of 5 $mm^2$ per sample. The number of cells on the surface were counted using the analyze particle tool in ImageJ. For the GREEN-ON and GREEN-OFF system, in the box plots, the box represents the 25–75% percentile and the whiskers are the 10–90% percentiles. Statistical significance is evaluated using the One Way ANOVA test. *p*-value *** <0.001

### 8.2.9 Cell patterning

A PEG-$Ni^{2+}$-NTA modified glass surface with the CarH ($1^{st}$ layer)/FN ($2^{nd}$ layer) film was illuminated with green light through TRITC channel filter for 2 second by an inverted fluorescence microscope (DMi8, Leica) through a 20x objective with an adjustable field diaphragm. Then surfaces were incubated with $1\times10^6$ MCF-7 cells were seeded on the surface in the 2 ml DMEM supplemented with 10% FBS and 1% P/S at 37 ℃, 5% $CO_2$ overnight. After cell incubation, surfaces were washed with PBS 1x and bright filed images of the samples were acquired.

### 8.2.10 Cell spatial and temporal control of cell adhesions

To pattern cells on GREEN-ON surfaces, surfaces modified with CarH and cRGD-alkyne peptide were illuminated in a desired pattern using the FRAP function with green light at 552 nm (argon laser, 10% intensity) for 1 min under a confocal laser scanning microscopy (Leica TCS SP8) through a 10x objective. Then, the surfaces were incubated with $1\times10^6$ MCF-7 cells in the 2 ml DMEM supplemented with 10% FBS and 1% P/S and 300 nM SiR-actin for actin staining at 37 ℃, 5% $CO_2$ overnight. Subsequently, 1 μg/ml Hoechest 33342 was added to stain the cell nuclei for 10 min and surfaces were washed with PBS before acquiring images of the cells on the surfaces in the actin and nuclear stain channels.

To trigger cell adhesions or detach cells upon green light illumination, CarH/cRGD-alkyne (GREEN-ON) or CarH-RGD (GREEN-OFF) functionalized glass surfaces were glued to a hollow µ-slide well dish (ibidi). For the GREEN-ON surfaces $2\times10^5$ MCF-7 cells and for the GREEN-OFF surfaces $1\times10^5$ MDA-MB-231 cells were seeded in the 2 ml DMEM supplemented with 10% FBS and 1% P/S containing and 300 nM SiR-actin for actin staining and incubated at 37 °C, 5% $CO_2$ overnight. The surfaces were washed twice with PBS and fresh DMEM supplemented with 10% FBS and 1% P/S was added. The cells were imaged in the interference reflection and SiR channels. For the cells on the GREEN-ON surface, single cells with lose initial contacts to the surface were identified and illuminated with green light at 552 nm (1% intensity) for 30 min using the FRAP function and the cells were imaged over the course of 90 min. For the GREEN-OFF surfaces, a group of adhered cells was places in the field of view and a subset of cells in a chosen area were illuminated with green light at 552 nm (1% intensity) for 20 min using the FRAP function. The surface was once washed with PBS and images in the different channels were acquired.

### 8.2.11 QCM-D measurement for the layer by layer system

All QCM-D measurements were performed on a Q-Sense E4 system (Q-Sense) with $SiO_2$ crystals (Q-sense) at room temperature with a flow rate of 300 µl/min. The $SiO_2$ crystals were cleaned with a 2% SDS solution in water over night, rinsed 3 times with Milli-Q water and dried in a $N_2$ stream. After the QCM-D crystals were cleaned with oxygen plasma (TePla 200-G, 0.2 mbar, 150 W, 10 min), the crystals were functionalized with PEG-$Ni^{2+}$-NTA as described above. These crystals were placed into the QCM-D chamber and the following solutions were passed over the crystal to form the LbL protein films: (1) Buffer A, 5 min; (2) 5 µM of 1$^{st}$ protein, 30 min; (3) Buffer A, 10 min; (4) 100 µM $NiCl_2$+25 µM 4-arm-PEG-NTA, 30 min; (5) Buffer A, 5 min; (6) 5 µM of 2$^{nd}$ protein, 30 min; (7) Buffer A, 10 min. Steps 4-7 were repeated to form additional proteins layers. To remove the protein layers a solution of 250 mM imidazole in Buffer A was passed over the QCM-D crystals for 5 min followed by a washing step with Buffer A for 5 min. Experiments which included green light illumination were performed with a window QCM-D module and a 15 W green LED lamp (Osram) was used for illumination. The 7$^{th}$ overtone of the QCM-D measurements was represented in all graphs. The QCM-D data was fitted to the Sauerbrey equation using a density of 1056 g/L to determine the film thicknesses after each step.

### 8.2.12 Functionalization of polystyrene beads with iLID

The $Ni^{2+}$-NTA functionalized polystyrene beads with a 2 μm diameter were purchased as a water suspension (50 mg/mL, 1.2 x $10^{10}$ beads/mL, stable in aqueous solutions, methanol, ethanol and DMSO). The protein was immobilized on the beads through His-tag-$Ni^{2+}$-NTA interaction by incubating 5 mg/mL of $Ni^{2+}$-NTA-functionalized beads in buffer A with 1 μM His-tagged iLID at 4 ℃ for 1 h. Then, excess protein was washed away twice by spinning down the beads (13000 rpm, 2 min) and resuspending them in buffer A. Before each experiment the protein functionalized beads were sonicated for 1 min to disperse in the buffer.

### 8.2.13 Attachment of iLID functionalized beads onto Nano immobilized substrates

To investigate the dependence of iLID functionalized bead onto Nano immobilized substrates on environmental parameters, illumination with blue light, pH as well as the presence of $H_2O_2$ and EDTA were altered in all possible combinations (16 conditions). Firstly, iLID functionalized beads was spin down (13000 rpm, 2 min) and suspended in different buffer solutions (300 mM NaCl, 50 mM Tris, at pH 7.4 or 3.5, with or without 10 mM $H_2O_2$ and/or with or without 50 mM EDTA). Then, 300 μL iLID-beads (5 mg/mL) were added on top of Nano functionalized substrates for 1 h in the dark or under blue light illumination (0.5 $mW/cm^2$, LED blue light panel (Albrillo LL-GL003, 225 LEDs, 460 nm, 14 W) with 1 neutral density filter (white polycarbonate plate with 30% transmission from Alt-Intech)). After 1 h, the substrates were washed twice with buffer A to remove beads that did not attach and incubated with 300 μL 10% (w/v) paraformaldehyde (PFA) for 15 min for fixation. Finally, the glass substrates were washed twice with buffer A and for each substrate bright field images (DMi8, Leica) were acquired through an 40x air objective using the tile scan function (at least 30 images with a total field of view of 500 μm x 500 μm). The beads on the surface were automatically counted using the particle analyzer function in Fiji ImageJ.

### 8.2.14 DTNB assay

The DTNB (5,5-dithio-bis-(2-nitrobenzoic acid) assay was used to quantify the oxidation of thiol groups in iLID. For this purpose, DTT was removed from purified iLID protein by dialysis with buffer A at 4 ℃. Subsequently, 10 mM $H_2O_2$ was added to 100 μM iLID (stock protein) and incubated for 2 h at 4 ºC. iLID (0 to 50 μM), which was either treated with $H_2O_2$ or not, was added to 100 μM DTNB in a total volume of 200 μL buffer A and the absorbance at 412 nm was measured after 5 min using a plate reader (TECAN, infinite M1000). 100 μM

DTNB in 200 µL buffer A was used as a blank sample and its absorbance at 412 nm was subtracted as background from all samples. A standardization curve for thiol concentration was establishes using mercaptoethanol (0 to 50 µM) instead of iLID in the above measurement. Based on the standardization curve the concentration thiol groups before and after $H_2O_2$ treatment was calculated.

### 8.2.15 Removal of His6-tag from His6-MBP-TEV-Nano for QCM-D measurements

The TEV cutting site was used to cleave the His6-tag from the protein Nano after $Ni^{2+}$-NTA affinity purification to yield cut-Nano.[38] For this the purified proteins were incubated with His6-TEV protease at 1:50 concentration ratio (protein: TEV protease) overnight at 4 ℃ (reaction buffer: 50 mM Tris pH 8.0, 0.5 mM EDTA, 1 mM DTT). Then, the His6-TEV protease and the cut fragment His6-MBP were removed using a $Ni^{2+}$-NTA column. The cut-Nano protein without the His6-tag was collected in the flow through and used in QCM-D measurement.

### 8.2.16 Preparation of $Ni^{2+}$-NTA liposomes

For the preparation of liposomes from DGS-NTA-$Ni^{2+}$ and PC, 200 µL 10 mg/mL PC (dissolved in chloroform) was mixed with 20 µL 10 mg/mL DGS-NTA-$Ni^{2+}$ (dissolved in chloroform) and deposited into a round bottom glass vial for solvent evaporation under a gentle stream of nitrogen. The lipid film was rehydrated with a vesicle buffer, containing 20 mM HEPES, 2.5 mM $MgSO_4$, 50 mg/mL sucrose and resuspended at a lipid concentration of 10 mg/mL by gentle vortexing. The suspension of vesicle was subjected to 5 freeze-thaw cycles (1 min in liquid nitrogen then water bath, 37 ℃, until thawed completely, followed by 30 s vortexing). Finally, the size of liposomes in the suspension was unified by the extrusion (11 times) of lipid suspension through 100 nm pores (polycarbonate membrane, Whatman).

### 8.2.17 Co-reconstitution of $EF_OF_1$-ATP synthase and bR into $Ni^{2+}$-NTA liposomes

100 µL of preformed $Ni^{2+}$-NTA liposomes were mixed with 80 µL bR and 7 µL $EF_OF_1$-ATP synthase in the presence of 0.8% Triton X-100 (the final concentration of bR and ATP synthase was 0.5 µM and 0.1 µM, respectively). To stabilize the ATP synthase, 0.5 µL 1 M $MgCl_2$ was also added to the solution. After 15 minutes of incubation in the dark under gentle shaking, 80 mg of wet SM-2 Bio-Beads were added for removal of detergent. The solution was incubated for further 60 minutes under constant shaking in the dark before the Bio-Beads were removed. The average vesicle size and dispersity were determined by dynamic light

scattering (DLS) using a Zetasizer Nano ZS (Malvern, Worcestershire, UK) with a 633 nm helium-neon laser and backscattering detection. 5 µl of vesicles were diluted in 1 ml vesicle buffer and samples were measured at a fixed 173 ° scattering angle at 25 ℃. All reported values are based on the average of three measurements. Each measurement consisted of 3x5 runs with 70s duration.

### 8.2.18 bR orientation and proton pumping activity

To assay the orientation of bR in the vesicle, proteinase K (Roche) was added to a final concentration of 2.5 mg/ml. After incubation for 2 hours at 37 ℃, the reaction was stopped by adding the protease inhibitor phenylmethanesulfonylfluoride to a concentration of 10 mM while cooling the reaction on ice for 30 minutes. The reaction products were loaded onto 4-20% Tris-HCl Criterion Precast Gels (Bio-Rad) to analysis the orientation of bR. The proton pumping activity of bR was monitored using the pH sensitive dye pyranine. Before each measurement, 0.1 µM valinomycin was added to the solution to avoid the formation of a potential gradient that counteracts the generated pH gradient. After 1 hour of equilibration in the dark, the reaction was started by illumination with a 50 W LED lamp (SMD RGB Floodlight, V-TAC). The absorption change of pyranine at 405 and 450 nm was monitored using a diode array spectrometer (QEPRO, Ocean Optics). The pH was calculated by the absorbance ratio between 450 and 405 nm (A450/A405). The proton pumping rate was the average of three independent measurements.

### 8.2.19 ATP production and determination in reconstituted liposomes

For ATP production, 25 µL of co-reconstituted $Ni^{2+}$-NTA-ATP vesicles were diluted in 250 µL measurement buffer (20 mM HEPES, 2.5 mM $MgCl_2$, 50 mg/mL sucrose, 5 mM $NaH_2PO_4$, 1 mM DTT) containing 400 µM fresh ultra-pure ADP. For measuring the ATP production under different conditions, the pH was adjusted to 7.4 or 3.5 by adding HCl and/or supplemented with 10 mM $H_2O_2$ and/or 50 mM EDTA. Then, the samples were illuminated with a 15 W blue LED lamp or kept in the dark. Every 5 minutes, 25 µL of reaction solution was taken out and mixed with 25 µL trichloroacetic acid (TCA, 40 g/L) to stop the reaction.

The ATP concentration was determined using the ATP Bioluminescence Assay Kit CLS II. The luciferase reagent was prepared as a 10 times concentrated stock solution in 1 mL water. 3 µL of the luciferase stock solution were added in 197 µL measurement buffer (20 mM HEPES, 2.5 mM $MgCl_2$, 50 mg/mL sucrose, 5 mM $NaH_2PO_4$ and 1 mM fresh DTT) and the

background luminescence signal ($I_B$) was measured using a plate reader (TECAN, infinite M1000). Subsequently, 20 µl of sample was added and the sample luminescence signal ($I_S$) was measured. Finally, 10 µL of the ATP standard (7.8 µM, provided from the ATP Bioluminescence Assay Kit CLS II) was added for calibration and the luminescence signal ($I_C$) was recorded. The ATP concentration was calculated using the following equation:

$$C_{syn} = \frac{I_S - \left(I_B \cdot \frac{V_0}{V_1}\right)}{I_C - \left(I_S \cdot \frac{V_1}{V_2}\right)} \cdot \frac{C_C \cdot V_C}{V_2} \cdot \frac{V_1}{V_S} \cdot \frac{V_{TCA}}{V_{syn}}$$

where $C_{syn}$ is the concentration of produced ATP, $I_B$ is the luminescence intensity of the blank, $I_S$ is the luminescence intensity of the sample, $I_C$ is the luminescence intensity after adding the ATP standard, $V_0$ is the volume of luciferase (200 µL), $V_1$ is the volume of luciferase plus sample (220 µL), $V_2$ is the volume of luciferase plus sample and ATP standard (230 µL), $C_C$ is the concentration of the ATP standard (7.8 µM), $V_C$ is the volume of added ATP standard (10 µL), $V_S$ is the volume of the sample (20 µL), $V_{syn}$ is the volume of the sample before stopping the reaction with TCA (25 µL) and $V_{TCA}$ is the volume of sample after addition of TCA (50 µL).

### 8.2.20 QCM-D measurements for iLID/Nano system

QCM-D measurements were performed on a Q-Sense Analyzer at room temperature equipped with either a flow module (dark sample) and window module illuminated with a 15 W blue LED lamp (blue light sample). The flow rate was kept at 1000 µL/min and $SiO_2$ crystals (Q-sense) were used in all experiments.

The $SiO_2$ crystals were cleaned with a 2% SDS solution in water over night, rinsed 3 times with Milli-Q water and dried in a $N_2$ stream. Then, the QCM-D crystals were cleaned with oxygen plasma for 10 min, the crystals were placed into the QCM-D chamber and the following solutions were passed over the crystal: (1) Buffer A, 5 min; (2) 1 mL of 0.1 mg/mL DOPC + 5 mol % DGS-NTA with 5 mM $CaCl_2$ to form a supported lipid bilayer (the pump was stopped once the lipids were on the crystal until a bilayer was formed); (3) Buffer A, 5 min; (4) 10 mM $NiCl_2$, 5 min to load the NTA-groups with $Ni^{2+}$; (5) Buffer A, 5 min; (6) 1 mL of 1 µM iLID (the flow was stopped when the frequency stabilized), 30 min; (7) Buffer A, 15 min. (8) different samples were used depending on the subsequent experiment.

To investigate the influence of $H_2O_2$ in the iLID/Nano interaction: All measurements were performed under blue light illumination. For iLID used in step (6) above was incubated with 10 mM $H_2O_2$ for 2 h at 4 ℃ before the QCM-D measurement. Then, following solutions were passed over the QCM-D crystal: (8) 600 µL 500 nM cut-Nano without His-tag (the flow was stopped when frequency stabilized), 30 min, (9) Buffer A, 15 min.

To investigate the adhesion of Nano functionalized ATP producing liposomes and their ATP production: Co-reconstituted ATP producing liposomes (DGS-NTA-$Ni^{2+}$: PC = 1:10) were functionalized with Nano by diluting 60 µL of liposomes as prepared above into 540 µL buffer A with 100 nM Nano and incubating for 2 h at 4 ℃ (Nano-ATP liposomes). QCM-D measurements in the dark and under blue light were performed in parallel and following solutions were passed over the QCM-D crystal: (8) 600 µL of Nano-ATP liposomes (the flow was stopped when the frequency stabilized), 30 min, (9) Buffer A, 15 min.

For quantifying the ATP production, after Nano-ATP vesicle had adhered to the QCM-D crystals (after step 9), the ATP measurement buffer (20 mM HEPES, 2.5 mM $MgCl_2$, 50 mg/mL sucrose, 5 mM $NaH_2PO_4$ and 1 mM fresh DTT) flushed into the chamber and crystals were incubated for 30 min under blue light. Then, the chambers were opened and 25 µL of solution above the QCM-D crystals was taken out for ATP quantification following the luminescence assay described above.

### 8.2.21 Separation of streptavidin Bio-His-Tag conjugates

A 30 µM streptavidin were mixed with 90 µM Bio-His-Tag (biotin-$(His)_6$) for 15 min at room temperature. A $Ni^{2+}$-NTA column (HisTrap™ HP, column volume 5 mL) was pre-equilibrated with 50 mL buffer A (50 mM Tris-HCl, 300 mM NaCl, pH 7.4) using a FPLC system (GE healthcare, AKTA explorer). Then, 0.5 mL streptavidin Bio-His-Tag reaction mixture was loaded on the $Ni^{2+}$-NTA column and the column was washed with 25 mL buffer A. Finally, the different streptavidin Bio-His-Tag conjugates were eluted with a linear imidazole gradient from 0 to 260 mM imidazole in buffer A over 130 mL. The elution of different species was monitored by the absorbance at 280 nm, the curves were corrected for the absorbance of imidazole and each peak was collected in a separate fraction. A flow rate of 0.5 ml/min was used throughout the experiment. The collected samples were dialyzed (10 kDa molecule weight cutoff) against 2 L of buffer A at 4 ℃ for at least 6 h to remove imidazole. Subsequently, the samples were concentrated using a centrifugal filtration device

(10 kDa molecular weight cutoff). The protein concentration was determined by UV-Vis spectroscopy.

To analyze the kinetic stability of S(Bio-His-Tag)$_2$, different samples were incubated at 4 ℃, room temperature and at 37 ℃ for one and five days and analyzed on a $Ni^{2+}$-NTA column using the same imidazole gradient as described above.

### 8.2.22 Separation of streptavidin Ibio-His-Tag conjugates

The $Cu^{2+}$-NTA column was prepared by removing $Ni^{2+}$ ion from a $Ni^{2+}$-NTA column (HisTrap$^{TM}$ HP, column volume 5 mL) with ethylenediaminetetraacetic acid (EDTA) and reloading it with $Cu^{2+}$ ions. Firstly, 30 μM streptavidin was mixed with 90 μM Ibio-His-Tag for 15 min at room temperature to assure the binding of iminobiotin to streptavidin. Then, 50 μM atto-565-biotin was added to the reaction mixture and incubated for another 15 min. 0.5 mL of the reaction mixture was loaded on a $Cu^{2+}$-NTA column, which was pre-equilibrated with 50 mL buffer A and then washed with 25 mL buffer A. At last, the different streptavidin conjugates were eluted with a linear imidazole gradient from 0 to 20 mM imidazole in buffer A over 100 mL. The elution of different species was monitored by the absorbance at 280 nm (streptavidin and atto-565-biotin) and 563 nm (atto-565-biotin), the curves were corrected for the absorbance of imidazole and different peaks were collected separately. A flow rate of 0.5 ml/min was used throughout the experiment. Each peak was first dialyzed against (10 kDa molecule weight cutoff) 2 L buffer pH=3.5, 50 mM Tris-HCl, 300 mM NaCl solution for 1 h at 4 ℃ to remove the Ibio-His-Tag and then dialyzed twice against 2 L buffer A for at least 6 h to remove the imidazole. The samples were concentrated using a centrifugal filtration devices (10 kDa molecule weight cutoff) for further studies. The protein concentration was determined by UV-Vis spectroscopy.

### 8.2.23 Determination of open biotin binding pockets

The number of open biotin binding pockets was determined using biotin-5-fluorescein, which's fluorescence is quenched upon binding to streptavidin. Typically, 200 μL of 10 nM of a streptavidin conjugate in buffer A were added in a transparent 96-well plate (Greiner bio-one, F-bottom), different concentrations (0 to 50 nM) of biotin-5-fluorescein were added to each well and the samples were incubated for 10 min at room temperature. The fluorescence intensity of each well was measured (excitation wavelength 490 nm, emission wavelength 524 nm) using a plate reader (TECAN, infinite M1000).

### 8.2.24 Mass spectrometry

MALDI-TOF was used to test the molecular weight of samples and performed on a Bruker Daltonics Reflex III spectrometer. Saturated solution of sinapinic acid dissolved in a 1:1 (water: acetonitrile) with 0.1% trifluoroacetic acid was used as the matrix solution. Typically, a sample solution (10 μM) was mixed (1:1) with the matrix solution and spotted on the steel plate. Then an additional aliquot of the matrix solution was added to dilute the sample and spotted again (repeat 3x). Spectra can be obtained in positive mode and the data was processed in mMass and Origin.

### 8.2.25 Preparation of biotinylated mOrange protein

The mOrange contains a biotinylation sequence (GLNDIFEAQKIEWHE) at its N-terminal, which is recognized by the enzyme BirA. To prepare biotinylated mOrange, 50 μM mOrange, 5 mM $MgCl_2$, 1 mM ATP, 1 μM BirA and 70 μM biotin were mixed in 1 mL buffer A and incubated at room temperature with gentle mixing (100 rpm/min) for 1 h. Then, additional 1 μM BirA and 70 μM biotin were added to the reaction mixture and incubated for 1 h. The reaction mixture was dialyzed (10 kDa molecular weight cutoff) against 2 L buffer A twice for at least 6 h at 4 ℃.

### 8.2.26 Preparation and analysis of mOrange streptavidin conjugates

Typically, 1 μM $S(Bio\text{-}His\text{-}Tag)_1$, $S(Bio\text{-}His\text{-}Tag)_2$ or $S(Bio\text{-}His\text{-}Tag)_3$ were mixed with 5 μM, 4 μM or 3 μM biotinylated mOrange, respectively, for at least 1 h at 4 ℃. Then, 400 μL of each reaction mixture was injected onto a HiLoad™ 16/600, Superdex™ 200 pg size elution column and eluted with 150 mL buffer A at a flow rate of 1 mL/min. The elution of different species was monitored through the absorbance at 280 nm. The molecule weight of the different species was determined based on a calibration curve established with five standard proteins (GE healthcare life science, 5 mg/mL thyroglobulin: MW 669 kDa, 0.3 mg/mL ferritin: MW 440 kDa, 4 mg/mL aldolase: MW 158 kDa, 3 mg/mL conalbumin: MW 75 kDa and 4 mg/mL ovalbumin: MW 44 kDa). For this, the partition coefficient ($K_{av}$) for each protein was calculated as follows:

$$K_{av} = \frac{V_e - V_0}{V_c - V_0}$$

where $V_o$ is the column void volume, $V_e$ is the elution volume and $V_c$ is the geometric column volume, which is equal to 120 mL for the HiLoad™ 16/600, Superdex™ 200 pg size

elution column. The $V_o$ was determined running blue dextran 2000 (400 µL, 1 mg/mL) (GE healthcare life science) on the same column and the first eluted peak was used as the void volume. The molecular weights of the different streptavidin mOrange (O) species (S(Bio-His-Tag)$_1$O$_3$, S(Bio-His-Tag)$_2$O$_2$ and S(Bio-His-Tag)$_3$O$_1$) was determined based on the linear fit of the $K_{av}$ versus molecule weight curve: S(Bio-His-Tag)$_1$O$_3$ (theo. 148.4 kDa, exp. 141.0 kDa), S(Bio-His-Tag)$_2$O$_2$ (theo. 118.6 kDa, exp. 108.6 kDa) and S(Bio-His-Tag)$_3$O$_1$ (theo. 88.8 kDa, exp. 81.3 kDa).

### 8.2.27 Labeling of biotinylated cell surface molecules

MDA-MB-231 cells were seeded at 3x10$^4$ cells/cm$^2$ in a 8-well cell culture plate (glass bottom, ibidi) in 300 µL Dulbecco's modified Eagle's medium (DMEM) supplemented with 10 % heat inactivated fetal bovine serum (FBS, 10%) and 1 % penicillin/streptomycin (P/S) and incubated at 37 °C, 5% $CO_2$ overnight. The next day, the cells were washed three times using cold phosphate buffer saline supplemented 1 mM $CaCl_2$ and 0.1 mM $MgCl_2$ (PBS-CM) and then the cell membrane was biotinylated using 0.25 mM sulfo-NHS-LC-biotin in PBS-CM for 30 min on ice.[10] After washing the cells twice using cold PBS-CM, the cells were incubated with 100 mM glycine in PBS-CM for 2 min on ice to stop further biotinylation. Cells were washed again twice with cold PBS-CM and then incubated with 1.5 µM $SA_1$, $SA_2$ or $SA_3$ in DMEM + 10 % FBS + 1 % P/S for 20 min on ice to label biotinylated surface molecules. The cells were washed twice with PBS, the medium was exchanged with pre-warmed DMEM + 10% FBS + 1% P/S and the cells were incubated for 0, 10 and 30 min at 37 °C in 5% $CO_2$ atmosphere. Then the cells were washed twice with PBS and fixed using 4% paraformaldehyde (PFA) in PBS and stained by 1 µg/mL TO-PRO-3. Finally, samples were washed twice with PBS and imaged in the atto-565 and far-red channels using a confocal laser scanning microscope (Leica TCS SP8) equipped with 561 nm and 633 nm laser lines and a 63x $H_2O$ objective. For live cell imaging, the cells were treated as described above and imaged in the atto-565 channel at room temperature after adding 1.5 µM $SA_1$ (Movie S1), $SA_2$ (Movie S2) or $SA_3$ (Movie S3). Images were analysed by Fiji ImageJ. For the analysis, the average fluorescence intensities of single cell in the atto-565 channel were measured by encircling single cells and measuring their average intensities. 25 cells were analysed per sample and fluorescence was corrected for the background.

### 8.2.28 Preparation of fluorescently labeled folic acid streptavidin and cellar uptake

A 10 μM of $SA_1$, $SA_2$ or $SA_3$ (A: atto-565-biotin) were mixed with 40 μM, 30 μM or 20 μM folic acid-PEG-biotin (F), respectively and incubated for 20 min at room temperature. Each reaction mixture was dialyzed (10 kDa molecule weight cutoff) against 2 L buffer A twice for at least 6 h yielding $SA_1F_3$, $SA_2F_2$ and $SA_3F_1$. The protein concentration of each conjugate and their relative fluorescence were determined by UV-Vis and fluorescence spectroscopy.

For cellular uptake studies, MDA-MB-231 or MCF-7 cells were seeded at $5x10^4$ cell/well on glass coverslips (VWR, diameter 18 mm) in 12-well cell culture plates (Greiner bio-one, F-bottom) and were cultured in RPMI-1640 medium without folic acid + 10 % FBS + 1 % P/S at 37 ℃, 5% $CO_2$ overnight. The next day, the cells were washed twice with PBS, 500 μL of RPMI-1640 medium without folic acid + 10 % FBS + 1 % P/S containing 1 μM of different streptavidin conjugates ($SA_1$, $SA_2$, $SA_3$, $SA_1F_3$, $SA_2F_2$ or $SA_3F_1$) was added to each cell type and the cells were incubated at 37 ℃, 5% $CO_2$ for 4 h. Afterward, the cells were washed twice with PBS and fixed with 4 % PFA in PBS for 15 min at room temperature. The cells were washed twice with PBS and were mounted on a glass slide (ROTH, 24x60 mm) with 40 μL Mowiol-488 containing 1 μg/ml DAPI. The cells were imaged in the atto-565 and DAPI channels using a confocal laser scanning microscope (Leica TCS SP8) equipped with 405 nm and 552 nm laser lines and a 63x $H_2O$ objective. Images were analyzed by Fiji ImageJ. For the analysis, the average fluorescence intensities of single cell in the atto-565 channel were measured by encircling single cells and measuring their average intensities. 25 cells were analyzed per sample and fluorescence was corrected for the background. Then, fluorescence intensities measured for $SA_1F_3$, $SA_2F_2$ and $SA_3F_1$ in the cells were normalized taking into account the relative fluorescence brightness's of $SA_1F_3$, $SA_2F_2$ and $SA_3F_1$ as measured in solution.

### 8.2.29 Preparation of tetrafluorophore streptavidin conjugates

The $Cu^{2+}$-NTA column was prepared by removing $Ni^{2+}$ ion from a $Ni^{2+}$-NTA column (HisTrap™ HP, column volume 5 mL) with ethylenediaminetetraacetic acid (EDTA) and reloading it with $Cu^{2+}$ ions. Firstly, 1 μM $SA_1$ (S: streptavidin, A: atto-565-biotin) prepared as previously described was mixed with 2 μM Ibio-His-tag for 15 min at room temperature to assure the binding of iminobiotin to streptavidin. Then, 2 μM B (atto-425-biotin) was added to the reaction mixture and incubated for another 15 min. 0.5 mL of the reaction mixture was loaded on a $Cu^{2+}$-NTA column, which was preequilibrated with 50 mL buffer A (50 mM

Tris-HCl, 300 mM NaCl, pH=7.4) and then washed with 25 mL buffer A. At last, the different streptavidin conjugates conjugates ($S(Ibio\text{-}His\text{-}tag)_1A_1B_2$, $S(Ibio\text{-}His\text{-}tag)_2A_1B_1$, $S(Ibio\text{-}His\text{-}tag)_3A_1$) were eluted with a linear imidazole gradient from 0 to 120 mM imidazole in buffer A over 60 mL. The elution of different species was monitored by the absorbance at 563 nm (the absorbance of atto-565), 436 nm (the absorbance of atto-425) and different peaks were collected separately. A flow rate of 0.5 ml/min was used throughout the experiment. Each peak was first dialyzed (10 kDa molecule weight cutoff) against 2 L buffer pH=3.5, 50 mM Tris-HCl, 300 mM NaCl solution for 1 h at 4 ℃ to remove the Ibio-His-tag and then dialyzed twice against 2 L buffer A for at least 6 h to remove the imidazole. The samples were concentrated using a centrifugal filtration devices (10 kDa molecule weight cutoff) for further studies. Similarly, $SA_1B_1$ (1 μM) isolated in the previous step was mixed with Ibio-His-tag (1.5 μM) and C (atto-665-biotin, 1.5 μM) to prepare $SA_1B_1C_1$, the elution of different species ($S(Ibio\text{-}His\text{-}tag)_1A_1B_1C_1$, $S(Ibio\text{-}His\text{-}tag)_2A_1B_1$) was monitored by the absorbance at 563 nm (the absorbance of atto-565), 436 nm (the absorbance of atto-425) and 663 nm (the absorbance of atto-665). After the same dialysis and concentrating steps, $SA_1B_1C_1$ was isolated. The final fluorophore biotin-5-fluorescein (D) was added stoichiometrically to $SA_1B_1C_1$ as also detailed below to yield $SA_1B_1C_1D_1$.

### 8.2.30 Förster resonance energy transfer (FRET) measurement

Sample of $SA_1B_1C_1$ (S: streptavidin, A: atto-565-biotin, B: atto-425-biotin and C: atto-665-biotin) was used to measure the FRET fluorescence. Firstly, for determination of the assembled ratio A:B:C, 100 μL 1 μM of the sample were applied into a plate reader (TECAN, infinite M1000), the absorbance spectrum (350 nm-900 nm) of the solution was measured. As control absorbance spectra of same concentration of atto-565-biotin, atto-425-biotin and atto-665-biotin were recorded and subtracted for the calculation. The ratio of A:B:C was determined from the absorption envelopes and a ratio of 0.78:1:0.81 was calculated. Then, 200 μL 1 μM of $SA_1B_1C_1$ in buffer A were added in a transparent 96-well plate (Greiner bio-one, F-bottom), the excitation wavelength was set as 400 nm and the emission spectrum was measured from 420 nm to 800 nm using a plate reader (TECAN, infinite M1000). As a control, 1 μM streptavidin was mixed with 1 μM of each of the fluorophores (atto-425-biotin, atto-565-biotin and atto-665-biotin) for 15 minutes to yield a statistical mixture of streptavidin conjugates.

### 8.2.31 Preparation of doxorubicin-biotin

Doxorubicin-biotin was synthesized according to literature.[2] Typically, to an ice cold solution of biotin-N-hydroxysuccinimide ester (0.14g, 0.41 mmmol) in DMF (10 ml) was added doxorubicin (0.3 g, 0.41 mmol) under argon atmosphere. After stirring for 30 min, triethylamine (0.5ml, 2 mmol) was added to this reaction mixture and was allowed to stir for another 12 h at room temperature. The reaction was monitored by TLC (Merck Silica 60, HF 254, 20: 80 methanoldichloromethane v/v). After completion of the reaction, excess diethyl ether (100 ml) was added to the reaction mixture. The red solid thus obtained was filtered and washed three times with diethyl ether (50 ml, three times). This red solid was then subjected to column chromatography using methanol-dichloromethane (20:80, v/v) as an eluent to obtain 0.25 g (Yield = 78%). LC-MS: $T_R$= 5.5 min, ESI m/z: calculated for. $C_{37}H_{43}N_3O_{13}S$: 769; found 792 $[M+Na]^+$ , 809 $[M+K]^+$. MALDI-ToF (DHB): m/z: calculated for. $C_{37}H_{43}N_3O_{13}S$: 769; found 792 $[M+Na]^+$ , 809 $[M+K]^+$. $^1H$ NMR (MeOD-d4, 300 MHz): 7.91 (d, 2H, aromatic), 7.50 (d, 1H, aromatic), 5.38 (brs, 1H, OH), 5.25 (brs, 1H, OH), 4.97 (s, 2H, -CH2-OH), 4.33 (brs, 2H, OH), 4.07 (m, 2H, CH, CH), 4.16-4.13 (m, 1H, CH), 3.94 (s, 3H, OCH3), 3.41 (m, 1H, CH), 3.09 (brs, 2H, OH), 3.10-3.00 (m, 4H, CH2, CH), 2.88-2.54 (m, 3H, CH2, CH), 2.20-2.00 (m, 1H, CH), 1.41-1.13 (m, 8H, CH2, CH3, CH2).

### 8.2.32 Preparation of biotin-NH-PKKKRKVC-COOH

The cell nucleus location sequence (PKKKRKVC) is a peptide derived from the simian virus 40 large tumor antigen (SV40 large T antigen), to enhance nuclear entry. For biotinylation, 5 mg (5.08 μmol, 1 mol. equiv.) of peptide was dissolved in 50 mM phosphate buffer pH 6.5 and 5 eq (13.4 mg, 25.4 μmol) Biotin-TEG-MI was added and shaken for 4h at RT. Product was subjected to reversed phase HPLC using a XDB-C18 column with the mobile phase starting from 100% solvent A (0.1% TFA in water) and 0% solvent B (0.1% TFA in acetonitrile) with a flow rate of 4 mL per minute, raising to 5% solvent B in five minutes, 15% solvent B in 10 minutes, and then reaching 100% solvent B after 29 minutes. It remained in this state for one minute. Solvent B concentration was then finally lowered to 5 % in five minutes. Absorbance was monitored at 280 nm and 254 nm. The retention time for biotin-NH–PKKKRKVC–COOH was 10.5 minutes, and 2.10 mg (1,39 μmol, 30%) of the product was obtained after lyophilization. LC-MS:$T_R$: 3.91, m/z = $[M+ H]^+$ 1511. MALDI-ToF-MS (CHCA): m/z = calculated. for $C_{67}H_{121}N_{19}O_{16}S_2$: 1511, $[M+H]^+$ 1511, $[M+Na]^+$ 1534.

### 8.2.33 Separation of tetrafunctional streptavidin conjugate ($SA_1F_1D_1C_1$)

A 10 μM $SA_1$ (S: streptavidin, A: atto-565-biotin) prepared as previously described[1] was mixed with 20 μM Ibio-His-tag for 15 min at room temperature to assure the binding of iminobiotin to streptavidin. Then, 20 μM F (folic acid-PEG-biotin) was added to the reaction mixture and incubated for another 15 min. 0.5 mL of the reaction mixture was loaded on a $Cu^{2+}$-NTA column, which was pre-equilibrated with 50 mL buffer A and then washed with 25 mL buffer A. At last, the different streptavidin conjugates ($S(Ibio\text{-}His\text{-}tag)_1A_1F_2$, $S(Ibio\text{-}His\text{-}tag)_2A_1F_1$, $S(Ibio\text{-}His\text{-}tag)_3A_1$) were eluted with a linear imidazole gradient from 0 to 120 mM imidazole in buffer A over 60 mL. The elution of different species was monitored by the absorbance at 280 nm and different peaks were collected separately. Each peak was first dialyzed against (10 kDa molecule weight cutoff) 2 L buffer pH=3.5, 50 mM Tris-HCl, 300 mM NaCl solution for 1 h at 4 ℃ to remove the Ibio-His-tag and then dialyzed twice against 2 L buffer A for at least 6 h to remove the imidazole. The samples were concentrated using a centrifugal filtration devices (10 kDa molecule weight cutoff) for further studies. Similarly, 10 μM $SA_1F_1$ was mixed with 15 μM Ibio-His-tag and 15 μM D (doxorubicin-biotin) to prepare $SA_1F_1D_1$. As described before the different species ($S(Ibio\text{-}His\text{-}tag)_1A_1F_1D_1$, $S(Ibio\text{-}His\text{-}tag)_2A_1F_1$) were separated with $Cu^{2+}$-NTA column using a linear imidazole gradient and the Ibio-His-tag was removed under acidic conditions and dialysis. Then, $SA_1F_1D_1$ (2 μM) was mixed with C (3 μM, nucleus penetration peptide: biotin-NH-PKKKRKVC-COOH) and incubated for 20 min at room temperature. $SA_1F_1D_1C_1$ was dialyzed (10 kDa molecule weight cutoff) against 2 L buffer A twice for at least 6 h to remove excess C.

### 8.2.34 Cellular uptake of streptavidin conjugates

For cellular uptake studies, MDA-MB-231 or MCF-7 cells were seeded at $5x10^4$ cell/well on glass coverslips (VWR, diameter 18 mm) in 12-well cell culture plates (Greiner bio-one, F-bottom) and were cultured in RPMI-1640 medium without folic acid supplemented with 10 % heat inactivated fetal bovine serum (FBS, 10%) and 1 % penicillin/streptomycin (P/S) at 37 ℃, 5% $CO_2$ overnight. The next day, the cells were washed twice with PBS and 500 μL of RPMI-1640 medium without folic acid + 10 % FBS + 1 % P/S containing 1 μM of different streptavidin conjugates ($SA_1$, $SA_1F_1$, $SA_1F_2$, $SA_1F_3$, $SA_1F_1D_1$ or $SA_1F_1D_1C_1$, cells without any streptavidin conjugates were set as blank) was added to each well. The cells were incubated at 37 ℃, 5% $CO_2$ for 4 h, washed twice with PBS and fixed with 4 % PFA in PBS for 15 min at room temperature. Subsequently, the cells were washed twice with PBS and

mounted on a glass slide (ROTH, 24x60 mm) with 40 µL Mowiol-488 containing 1 µg/ml DAPI. The cells were imaged in the DAPI and atto-565 channels using a confocal laser scanning microscope (Leica TCS SP8) equipped with 405 nm and 552 nm laser lines through a 63x $H_2O$ objective. Images were analyzed by Fiji ImageJ. For the analysis, the average fluorescence intensities of single cell in the atto-565 channel were measured by encircling single cells and mseasuring their average intensities. 20 cells were analyzed per sample and fluorescence intensities were background corrected.

### 8.2.35 MTT assay

MDA-MB-231 or MCF-7 cells were seeded at $5x10^3$ cell/well in 96-well cell culture plates (Greiner bio-one, F-bottom) and were cultured in RPMI-1640 medium without folic acid + 10 % FBS + 1 % P/S at 37 ℃, 5% $CO_2$ overnight. The next day, the cells were washed twice with PBS and cultured in 200 µL of RPMI-1640 without folic acid + 10 % FBS + 1 % P/S containing different concentrations (0 - 2.0 µM) of different streptavidin conjugates (D, $SA_1F_1D_1$, $SA_1F_1D_1C_1$ or statistical mixture of streptavidin conjugates) at 37 ℃, 5% $CO_2$ for 72 h. The statistical mixture of streptavidin conjugates was prepared by mixing streptavidin with A, F, D and C in a ratio of 1:1:1:1:1 for 20 minutes. Subsequently, the cells were washed twice with PBS and 200 µL of RPMI-1640 medium without folic acid + 10 % FBS + 1 % P/S containing 1.2 mM MTT was added to each well and the cells were incubated at 37 ℃, 5% $CO_2$ for 4 h. Then, the culture medium was discarded and 200 µL of DMSO was added to the cells to dissolve the dark blue formazan crystals. After 10 minutes, absorbance at 550 nm of each well was measured using a plate reader (TECAN, infinite M1000). The experiment was repeated three times. The cell viability was expressed as the percentages of viable cells compared to the survival of the control cells. The $IC_{50}$ (50% inhibitory concentration) was determined by log dosage versus concentration curve.

# Chapter 9. References


1. Schwille, P.; Spatz, J.; Landfester, K.; Bodenschatz, E.; Herminghaus, S.; Sourjik, V.; Erb, T.; Bastiaens, P.; Lipowsky, R.; Hyman, A.; Dabrock, P.; Baret, J. C.; Vidakovic-Koch, T.; Bieling, P.; Dimova, R.; Mutschler, H.; Robinson, T.; Tang, D.; Wegner, S.; Sundmacher, K., MaxSynBio - Avenues towards creating cells from the bottom up. *Angew. Chem. Int. Ed.* **2018**, *57*, 13382-13392.

2. Forster, A. C.; Church, G. M., Towards synthesis of a minimal cell. *Mol. Syst. Biol.* **2006**, *2*, 45.

3. Endy, D., Foundations for engineering biology. *Nature* **2005**, *438*, 449-453.

4. Majumder, S.; Liu, A. P., Bottom-up synthetic biology: modular design for making artificial platelets. *Phys. Biol.* **2017**, *15*, 013001.

5. Chang, T. M. S., 50th anniversary of artificial cells: Their role in biotechnology, nanomedicine, regenerative medicine, blood substitutes, bioencapsulation, cell/stem cell therapy and nanorobotics. *Artif. Cell Blood Sub.* **2007**, *35*, 545-554.

6. Saito, H.; Yamada, A.; Ohmori, R.; Kato, Y.; Yamanaka, T.; Yoshikawa, K.; Inoue, T., Towards constructing synthetic cells: RNA/RNP evolution and cell-free translational systems in giant liposomes. *Int. Sym. Micro-Nanom.* **2007**, 286-291.

7. Van Nies, P.; Westerlaken, I.; Blanken, D.; Salas, M.; Mencia, M.; Danelon, C., Self-replication of DNA by its encoded proteins in liposome-based synthetic cells. *Nat. Commun.* **2018**, *9*.

8. Tang, T. Y. D.; Cecchi, D.; Fracasso, G.; Accardi, D.; Coutable-Pennarun, A.; Mansy, S. S.; Perriman, A. W.; Anderson, J. L. R.; Mann, S., Gene-mediated chemical communication in synthetic protocell communities. *ACS Synth. Biol.* **2018**, *7*, 339-346.

9. Martino, C.; Kim, S. H.; Horsfall, L.; Abbaspourrad, A.; Rosser, S. J.; Cooper, J.; Weitz, D. A., Protein expression, aggregation, and triggered release from polymersomes as artificial cell-like structures. *Angew. Chem. Int. Ed.* **2012**, *51*, 6416-6420.

10. Choi, H. J.; Montemagno, C. D., Artificial organelle: ATP synthesis from cellular mimetic polymersomes. *Nano Lett* **2005**, *5*, 2538-2542.

11. Van Dongen, S. F. M.; de Hoog, H. P. M.; Peters, R. J. R. W.; Nallani, M.; Nolte, R. J. M.; van Hest, J. C. M., Biohybrid polymer capsules. *Chem. Rev.* **2009**, *109*, 6212-6274.

12. Holowka, E. P.; Sun, V. Z.; Kamei, D. T.; Deming, T. J., Polyarginine segments in block copolypeptides drive both vesicular assembly and intracellular delivery. *Nat. Mater.* **2007**, *6*, 52-57.

13. Bellomo, E. G.; Wyrsta, M. D.; Pakstis, L.; Pochan, D. J.; Deming, T. J., Stimuli-responsive polypeptide vesicles by conformation-specific assembly. *Nat. Mater.* **2004**, *3*, 244-248.

14. Schwille, P.; Spatz, J.; Landfester, K.; Bodenschatz, E.; Herminghaus, S.; Sourjik, V.; Erb, T. J.; Bastiaens, P.; Lipowsky, R.; Hyman, A.; Dabrock, P.; Baret, J. C.; Vidakovic-Koch, T.; Bieling, P.; Dimova, R.; Mutschler, H.; Robinson, T.; Tang, T. Y. D.; Wegner, S.; Sundmacher, K., MaxSynBio: Avenues towards creating cells from the bottom up. *Angew. Chem. Int. Ed.* **2018**, *57*, 13382-13392.

15. Long, M. S.; Jones, C. D.; Helfrich, M. R.; Mangeney-Slavin, L. K.; Keating, C. D., Dynamic microcompartmentation in synthetic cells. *Proc. Natl. Acad. Sci. USA* **2005**, *102*, 5920-5925.

16. Gobbo, P.; Patil, A. J.; Li, M.; Harniman, R.; Briscoe, W. H.; Mann, S., Programmed assembly of synthetic protocells into thermoresponsive prototissues. *Nat. Mater.* **2018**, *17*, 1145-1153.

17. Lee, E. S.; Kim, D.; Youn, Y. S.; Oh, K. T.; Bae, Y. H., A virus-mimetic nanogel vehicle. *Angew. Chem. Int. Ed.* **2008**, *47*, 2418-2421.

18. Li, M.; Harbron, R. L.; Weaver, J. V. M.; Binks, B. P.; Mann, S., Electrostatically gated membrane permeability in inorganic protocells. *Nat. Chem.* **2013**, *5*, 529-536.

19. Gardner, P. M.; Winzer, K.; Davis, B. G., Sugar synthesis in a protocellular model leads to a cell signalling response in bacteria. *Nat. Chem.* **2009**, *1*, 377-383.

20. Peters, R. J. R. W.; Nijemeisland, M.; van Hest, J. C. M., Reversibly triggered protein-ligand assemblies in giant vesicles. *Angew. Chem. Int. Ed.* **2015**, *54*, 9614-9617.

21. Martin, N.; Douliez, J. P.; Qiao, Y.; Booth, R.; Li, M.; Mann, S., Antagonistic chemical coupling in self-reconfigurable host-guest protocells. *Nat. Commun.* **2018**, *9*.

22. Adamala, K.; Szostak, J. W., Nonenzymatic template-directed RNA synthesis inside model protocells. *Science* **2013**, *342*, 1098-1100.

23. Chen, I. A.; Salehi-Ashtiani, K.; Szostak, J. W., RNA catalysis in model protocell vesicles. *J. Am. Chem. Soc.* **2005**, *127*, 13213-13219.

24. Weiss, M.; Frohnmayer, J. P.; Benk, L. T.; Haller, B.; Janiesch, J. W.; Heitkamp, T.; Borsch, M.; Lira, R. B.; Dimova, R.; Lipowsky, R.; Bodenschatz, E.; Baret, J. C.; Vidakovic-Koch, T.; Sundmacher, K.; Platzman, I.; Spatz, J. P., Sequential bottom-up assembly of mechanically stabilized synthetic cells by microfluidics. *Nat. Mater.* **2018**, *17*, 89-96.

25. Chakraborty, T.; Bartelt, S. M.; Steinkuhler, J.; Dimova, R.; Wegner, S. V., Light controlled cell-to-cell adhesion and chemical communication in minimal synthetic cells. *Chem. Commun.* **2019**, *55*, 9448-9451.

26. Huang, C.; Yang, G.; Ha, Q.; Meng, J. X.; Wang, S. T., Multifunctional "smart" particles engineered from live immunocytes: toward capture and release of cancer cells. *Adv. Mater.* **2015**, *27*, 310-313.

27. Zhang, Y.; Gal, N.; Itel, F.; Westensee, I. N.; Brodszkij, E.; Mayer, D.; Stenger, S.; Castellote-Borrell, M.; Boesen, T.; Tabaei, S. R.; Hook, F.; Stadler, B., Hybrid vesicles as intracellular reactive oxygen species and nitric oxide generators. *Nanoscale* **2019**, *11*, 11530-11541.

28. Liu, X. M.; Zhou, P.; Huang, Y. D.; Li, M.; Huang, X.; Mann, S., Hierarchical proteinosomes for programmed release of multiple components. *Angew. Chem. Int. Ed.* **2016**, *55*, 7095-7100.

29. Oberholzer, T.; Wick, R.; Luisi, P. L.; Biebricher, C. K., Enzymatic RNA replication in self-reproducing vesicles - an approach to a minimal cell. *Biochem. Bioph. Res. Co.* **1995**, *207*, 250-257.

30. Lentini, R.; Santero, S. P.; Chizzolini, F.; Cecchi, D.; Fontana, J.; Marchioretto, M.; Del Bianco, C.; Terrell, J. L.; Spencer, A. C.; Martini, L.; Forlin, M.; Assfalg, M.; Dalla Serra, M.; Bentley, W. E.; Mansy, S. S., Integrating artificial with natural cells to translate chemical messages that direct *E-coli* behaviour. *Nat. Commun.* **2014**, *5*.

31. Hanczyc, M. M.; Fujikawa, S. M.; Szostak, J. W., Experimental models of primitive cellular compartments: Encapsulation, growth, and division. *Science* **2003**, *302*, 618-622.

32. Lee, K. Y.; Park, S. J.; Lee, K. A.; Kim, S. H.; Kim, H.; Meroz, Y.; Mahadevan, L.; Jung, K. H.; Ahn, T. K.; Parker, K. K.; Shin, K., Photosynthetic artificial organelles sustain and control ATP-dependent reactions in a protocellular system. *Nat. Biotechnol.* **2018**, *36*, 530-535.

33. Feng, X. Y.; Jia, Y.; Cai, P.; Fei, J. B.; Li, J. B., Coassembly of photosystem II and ATPase as artificial chloroplast for light-driven ATP synthesis. *ACS Nano* **2016**, *10*, 556-561.

34. Bartelt, S. M.; Steinkuhler, J.; Dimova, R.; Wegner, S. V., Light-guided motility of a minimal synthetic cell. *Nano Lett.* **2018**, *18*, 7268-7274.

35. Junge, W.; Nelson, N., ATP synthase. *Annu. Rev. Biochem.* **2015**, *84*, 631-657.

36. Okuno, D.; Iino, R.; Noji, H., Rotation and structure of $F_oF_1$-ATP synthase. *J. Biochem.* **2011**, *149*, 655-664.

37. Matuschka, S.; Zwicker, K.; Nawroth, T.; Zimmer, G., ATP synthesis by purified ATP-synthase from beef-heart mitochondria after coreconstitution with bacteriorhodopsin. *Arch. Biochem. Biophys.* **1995**, *322*, 135-142.

38. Etzold, C.; DeckersHebestreit, G.; Altendorf, K., Turnover number of *Escherichia coli* $F_oF_1$ ATP synthase for ATP synthesis in membrane vesicles. *Eur. J. Biochem.* **1997**, *243*, 336-343.

39. Chen, Z. W.; Silveira, G. D.; Ma, X. D.; Xie, Y. S.; Wu, Y. M. A.; Barry, E.; Rajh, T.; Fry, H. C.; Laible, P. D.; Rozhkova, E. A., Light-gated synthetic protocells for plasmon-enhanced chemiosmotic gradient generation and ATP synthesis. *Angew. Chem. Int. Ed.* **2019**, *58*, 4896-4900.

40. Otrin, L.; Marusic, N.; Bednarz, C.; Vidakovic-Koch, T.; Lieberwirt, I.; Landfester, K.; Sundmacher, K., Toward artificial mitochondrion: mimicking oxidative phosphorylation in polymer and hybrid membranes. *Nano Lett.* **2017**, *17*, 6816-6821.

41. Kroger, D.; Hucho, F.; Vogel, H., Ligand binding to nicotinic acetylcholine receptor investigated by surface plasmon resonance. *Anal. Chem.* **1999**, *71*, 3157-3165.

42. Butterfield, D. A.; Bhattacharyya, D.; Daunert, S.; Bachas, L., Catalytic biofunctional membranes containing site-specifically immobilized enzyme arrays: a review. *J. Membrane Sci.* **2001**, *181*, 29-37.

43. Mitchell, P., A perspective on protein microarrays. *Nat. Biotechnol.* **2002**, *20*, 225-229.

44. Kroger, D.; Katerkamp, A.; Renneberg, R.; Cammann, K., Surface investigations on the development of a direct optical immunosensor. *Biosens. Bioelectron.* **1998**, *13*, 1141-1147.

45. Nishi, M.; Kobayashi, J.; Pechmann, S.; Yamato, M.; Akiyama, Y.; Kikuchi, A.; Uchida, K.; Textor, M.; Yajima, H.; Okano, T., The use of biotin-avidin binding to facilitate biomodification of thermoresponsive culture surfaces. *Biomaterials* **2007**, *28*, 5471-5476.

46. Charras, G.; Sahai, E., Physical influences of the extracellular environment on cell migration. *Nat. Rev. Mol. Cell Bio.* **2014**, *15*, 813-824.

47. Mouw, J. K.; Ou, G. Q.; Weaver, V. M., Extracellular matrix assembly: a multiscale deconstruction. *Nat. Rev. Mol. Cell Bio.* **2014**, *15*, 771-785.

48. Garcia, A. J.; Vega, M. D.; Boettiger, D., Modulation of cell proliferation and differentiation through substrate-dependent changes in fibronectin conformation. *Mol. Biol. Cell* **1999**, *10*, 785-798.

49. Paoli, P.; Giannoni, E.; Chiarugi, P., Anoikis molecular pathways and its role in cancer progression. *Bba-Mol. Cell Res.* **2013**, *1833*, 3481-3498.

50. Humphries, J. D.; Byron, A.; Humphries, M. J., Integrin ligands at a glance. *J. Cell Sci.* **2006**, *119*, 3901-3903.

51. Ricker, J.; Medda, R.; Wegner, S. V., Photo-ECM: a blue light photoswitchable synthetic extracellular matrix protein for reversible control over cell-matrix adhesion. *Adv. Biosyst.* **2019**, *3*, 1800302.

52. Lvov, Y.; Onda, M.; Ariga, K.; Kunitake, T., Ultrathin films of charged polysaccharides assembled alternately with linear polyions. *J. Biomat. Sci-Polym. E* **1998**, *9*, 345-355.

53. Moya, S.; Sukhorukov, G. B.; Auch, M.; Donath, E.; Mohwald, H., Microencapsulation of organic solvents in polyelectrolyte multilayer micrometer-sized shells. *J. Colloid Interf. Sci.* **1999**, *216*, 297-302.

54. Decher, G., Fuzzy nanoassemblies: toward layered polymeric multicomposites. *Science* **1997**, *277*, 1232-1237.

55. Richardson, J. J.; Cui, J. W.; Bjornmalm, M.; Braunger, J. A.; Ejima, H.; Caruso, F., Innovation in layer-by-layer assembly. *Chem. Rev.* **2016**, *116*, 14828-14867.

56. Zhang, X.; Chen, H.; Zhang, H. Y., Layer-by-layer assembly: from conventional to unconventional methods. *Chem. Commun.* **2007**, *14*, 1395-1405.

57. Wijeratne, S.; Liu, W. J.; Dong, J. L.; Ning, W. J.; Ratnayake, N. D.; Walker, K. D.; Bruening, M. L., Layer-by-layer deposition with polymers containing nitrilotriacetate, a convenient route to fabricate metal- and protein-binding films. *ACS Appl. Mater. Inter.* **2016**, *8*, 10164-10173.

58. Tang, Z. Y.; Kotov, N. A.; Magonov, S.; Ozturk, B., Nanostructured artificial nacre. *Nat. Mater.* **2003**, *2*, 413-418.

59. Monge, C.; Almodovar, J.; Boudou, T.; Picart, C., Spatio-temporal control of LbL films for biomedical applications: from 2D to 3D. *Adv. Healthca. Mater.* **2015**, *4*, 811-830.

60. Rivera-Gil, P.; De Koker, S.; De Geest, B. G.; Parak, W. J., Intracellular processing of proteins mediated by biodegradable polyelectrolyte capsules. *Nano Lett.* **2009**, *9*, 4398-4402.

61. Shimoni, O.; Yan, Y.; Wang, Y. J.; Caruso, F., Shape-dependent cellular processing of polyelectrolyte capsules. *ACS Nano* **2013**, *7*, 522-530.

62. Koktysh, D. S.; Kotov, N. A.; Liz-Marzan, L. M.; Yun, B. G.; Matts, R. L.; Grant, G. G. S., Layer-by-layer assembled films for biomedical applications. *Abstr. Pap. Am. Chem. S.* **2001**, *221*, 359.

63. Silva, J. M.; Georgi, N.; Costa, R.; Sher, P.; Reis, R. L.; Van Blitterswijk, C. A.; Karperien, M.; Mano, J. F., Nanostructured 3D constructs based on chitosan and chondroitin sulphate multilayers for cartilage tissue engineering. *Plos One* **2013**, *8*, e55451.

64. Lee, J.; Kotov, N. A., Notch ligand presenting acellular 3D microenvironments for *ex vivo* human hematopoietic stem-cell culture made by layer-by-layer assembly. *Small* **2009**, *5*, 1008-1013.

65. Phelps, J. A.; Morisse, S.; Hindie, M.; Degat, M. C.; Pauthe, E.; Van Tassel, P. R., Nanofilm biomaterials: localized cross-linking to optimize mechanical rigidity and bioactivity. *Langmuir* **2011**, *27*, 1123-1130.

66. Pan, Y.; Zhang, Y. Z.; Li, Y., Layer-by-layer self-assembled multilayer films of single-walled carbon nanotubes and tin disulfide nanoparticles with chitosan for the fabrication of biosensors. *J. Appl. Polym. Sci.* **2013**, *128*, 647-652.

67. Kreft, O.; Javier, A. M.; Sukhorukov, G. B.; Parak, W. J., Polymer microcapsules as mobile local pH-sensors. *J. Mater. Chem.* **2007**, *17*, 4471-4476.

68. Saito, A.; Miyazaki, H.; Fujie, T.; Ohtsubo, S.; Kinoshita, M.; Saitoh, D.; Takeoka, S., Therapeutic efficacy of an antibiotic-loaded nanosheet in a murine burn-wound infection model. *Acta. Biomater.* **2012**, *8*, 2932-2940.

69. Fujie, T.; Saito, A.; Kinoshita, M.; Miyazaki, H.; Ohtsubo, S.; Saitoh, D.; Takeoka, S., Dual therapeutic action of antibiotic-loaded nanosheets for the treatment of gastrointestinal tissue defects. *Biomaterials* **2010**, *31*, 6269-6278.

70. Costa, R. R.; Mano, J. F., Polyelectrolyte multilayered assemblies in biomedical technologies. *Chem. Soc. Rev.* **2014**, *43*, 3453-3479.

71. Elbert, D. L.; Herbert, C. B.; Hubbell, J. A., Thin polymer layers formed by polyelectrolyte multilayer techniques on biological surfaces. *Langmuir* **1999**, *15*, 5355-5362.

72. Eyckmans, J.; Boudou, T.; Yu, X.; Chen, C. S., A hitchhiker's guide to mechanobiology. *Dev. Cell* **2011**, *21*, 35-47.

73. Matsusaki, M.; Kadowaki, K.; Nakahara, Y.; Akashi, M., Fabrication of cellular multilayers with nanometer-sized extracellular matrix films. *Angew. Chem. Int. Ed.* **2007**, *46*, 4689-4692.

74. Kadowaki, K.; Matsusaki, M.; Akashi, M., Three-dimensional constructs induce high cellular activity: structural stability and the specific production of proteins and cytokines. *Biochem. Bioph. Res. Co.* **2010**, *402*, 153-157.

75. Pallarola, D.; von Bildering, C.; Pietrasanta, L. I.; Queralto, N.; Knoll, W.; Battaglini, F.; Azzaroni, O., Recognition-driven layer-by-layer construction of multiprotein assemblies on surfaces: a biomolecular toolkit for building up chemoresponsive bioelectrochemical interfaces. *Phys. Chem. Chem. Phys.* **2012**, *14*, 11027-11039.

76. Qi, W.; Yan, X. H.; Fei, J. B.; Wang, A. H.; Cui, Y.; Li, J. B., Triggered release of insulin from glucose-sensitive enzyme multilayer shells. *Biomaterials* **2009**, *30*, 2799-2806.

77. Luo, J.; Cao, S. Q.; Chen, X. Y.; Liu, S. N.; Tan, H.; Wu, W.; Li, J. S., Super long-term glycemic control in diabetic rats by glucose-sensitive LbL films constructed of supramolecular insulin assembly. *Biomaterials* **2012**, *33*, 8733-8742.

78. Borges, J.; Rodrigues, L. C.; Reis, R. L.; Mano, J. F., Layer-by-layer assembly of light-responsive polymeric multilayer systems. *Adv. Funct. Mater.* **2014**, *24*, 5624-5648.

79. Kurland, N. E.; Dey, T.; Kundu, S. C.; Yadavalli, V. K., Precise patterning of silk microstructures using photolithography. *Adv. Mater.* **2013**, *25*, 6207-6212.

80. Xin, H. B.; Li, Y. C.; Li, B. J., Controllable patterning of different cells via optical assembly of 1D periodic cell structures. *Adv. Funct. Mater.* **2015**, *25*, 2816-2823.

81. Liu, W. D.; Li, Y. F.; Wang, T. Q.; Li, D. W.; Fang, L. P.; Zhu, S. J.; Shen, H. Z.; Zhang, J. H.; Sun, H. C.; Yang, B., Elliptical polymer brush ring array mediated protein patterning and cell adhesion on patterned protein surfaces. *ACS Appl. Mater. Inter.* **2013**, *5*, 12587-12593.

82. Aslan, H.; Krissanaprasit, A.; Besenbacher, F.; Gothelf, K. V.; Dong, M. D., Protein patterning by a DNA origami framework. *Nanoscale* **2016**, *8*, 15233-15240.

83. Lee, T. T.; Garcia, J. R.; Paez, J. I.; Singh, A.; Phelps, E. A.; Weis, S.; Shafiq, Z.; Shekaran, A.; del Campo, A.; Garcia, A. J., Light-triggered *in vivo* activation of adhesive peptides regulates cell adhesion, inflammation and vascularization of biomaterials. *Nat. Mater.* **2015**, *14*, 352-360.

84. DeForest, C. A.; Tirrell, D. A., A photoreversible protein-patterning approach for guiding stem cell fate in three-dimensional gels. *Nat. Mater.* **2015**, *14*, 523-531.

85. Geiger, B.; Spatz, J. P.; Bershadsky, A. D., Environmental sensing through focal adhesions. *Nat. Rev. Mol. Cell Bio.* **2009**, *10*, 21-33.

86. Wegner, S. V.; Senturk, O. I.; Spatz, J. P., Photocleavable linker for the patterning of bioactive molecules. *Sci. Rep-Uk* **2015**, *5*.

87. Zhang, J.; Hu, T.; Liu, Y. B.; Ma, Y. X.; Dong, J.; Xu, L. P.; Zheng, Y. D.; Yang, H.; Wang, G. J., Photoswitched protein adsorption on electrostatically self-assembled azobenzene films. *Chemphyschem* **2012**, *13*, 2671-2675.

88. Wan, P. B.; Wang, Y. P.; Jiang, Y. G.; Xu, H. P.; Zhang, X., Fabrication of reactivated biointerface for dual-controlled reversible immobilization of cytochrome c. *Adv. Mater.* **2009**, *21*, 4362-4365.

89. Wang, Y. F.; Liu, Y.; Cheng, Y.; Kim, E.; Rubloff, G. W.; Bentley, W. E.; Payne, G. F., Coupling electrodeposition with layer-by-layer assembly to address proteins within microfluidic channels. *Adv. Mater.* **2011**, *23* (48), 5817-5821.

90. Madaboosi, N.; Uhlig, K.; Schmidt, S.; Jager, M. S.; Mohwald, H.; Duschl, C.; Volodkin, D. V., Microfluidics meets soft layer-by-layer films: selective cell growth in 3D polymer architectures. *Lab Chip* **2012**, *12*, 1434-1436.

91. Kim, K. S.; Zhao, Y.; Jang, H.; Lee, S. Y.; Kim, J. M.; Kim, K. S.; Ahn, J. H.; Kim, P.; Choi, J. Y.; Hong, B. H., Large-scale pattern growth of graphene films for stretchable transparent electrodes. *Nature* **2009**, *457*, 706-710.

92. Stassen, I.; Styles, M.; Grenci, G.; Van Gorp, H.; Vanderlinden, W.; De Feyter, S.; Falcaro, P.; De Vos, D.; Vereecken, P.; Ameloot, R., Chemical vapour deposition of zeolitic imidazolate framework thin films. *Nat. Mater.* **2016,** *15* (3), 304-310.

93. Filipponi, L.; Livingston, P.; Kaspar, O.; Tokarova, V.; Nicolau, D. V., Protein patterning by microcontact printing using pyramidal PDMS stamps. *Biomed. Microdevices* **2016**, *18*, 1-7.

94. Hoeppener, S.; Maoz, R.; Sagiv, J., Constructive microlithography: electrochemical printing of monolayer template patterns extends constructive nanolithography to the micrometer-millimeter dimension range. *Nano Lett.* **2003**, *3*, 761-767.

95. Childs, W. R.; Nuzzo, R. G., Decal transfer microlithography: A new soft-lithographic patterning method. *J. Am. Chem. Soc.* **2002**, *124*, 13583-13596.

96. Ginger, D. S.; Zhang, H.; Mirkin, C. A., The evolution of dip-pen nanolithography. *Angew. Chem. Int. Ed.* **2004**, *43*, 30-45.

97. Lee, K. B.; Park, S. J.; Mirkin, C. A.; Smith, J. C.; Mrksich, M., Protein nanoarrays generated by dip-pen nanolithography. *Science* **2002**, *295*, 1702-1705.

98. Salaita, K.; Wang, Y. H.; Mirkin, C. A., Applications of dip-pen nanolithography. *Nat. Nanotechnol.* **2007**, *2*, 145-155.

99. Bat, E.; Lee, J.; Lau, U. Y.; Maynard, H. D., Trehalose glycopolymer resists allow direct writing of protein patterns by electron-beam lithography. *Nat. Commun.* **2015**, *6*.

100. Lau, U. Y.; Saxer, S. S.; Lee, J.; Bat, E.; Maynard, H. D., Direct write protein patterns for multiplexed cytokine detection from live cells using electron beam lithography. *ACS Nano* **2016**, *10*, 723-729.

101. Rudd, A. K.; Cuevas, J. M. V.; Devaraj, N. K., SNAP-tag-reactive lipid anchors enable aargeted and spatiotemporally controlled localization of proteins to phospholipid membranes. *J. Am. Chem. Soc.* **2015**, *137*, 4884-4887.

102. Laboria, N.; Wieneke, R.; Tampe, R., Control of nanomolar interaction and in situ assembly of proteins in four dimensions by light. *Angew. Chem. Int. Ed.* **2013**, *52*, 848-853.

103. Rolli, C. G.; Nakayama, H.; Yamaguchi, K.; Spatz, J. P.; Kemkemer, R.; Nakanishi, J., Switchable adhesive substrates: Revealing geometry dependence in collective cell behavior. *Biomaterials* **2012**, *33*, 2409-2418.

104. Bamford, C. H.; Norrish, R. G. W., Primary photochemical reactions. Part VII. Photochemical decomposition of isovaleraldehyde and di-n-propyl ketone. *J. Chem. Soc.* **1935**, 1504-1511.

105. Setlow, R. B., The wavelengths in sunlight effective in producing skin cancer: a theoretical analysis. *Proc. Natl. Acad. Sci. USA* **1974**, *71*, 3363-6.

106. Gatterdam, V.; Ramadass, R.; Stoess, T.; Fichte, M. A. H.; Wachtveitl, J.; Heckel, A.; Tampe, R., Three-dimensional protein networks assembled by two-photon activation. *Angew. Chem. Int. Ed.* **2014**, *53*, 5680-5684.

107. Chen, Z. J.; He, S. Q.; Butt, H. J.; Wu, S., Photon upconversion lithography: patterning of biomaterials using near-infrared light. *Adv. Mater.* **2015**, *27* (13), 2203-2206.

108. Bartelt, S. M.; Chervyachkova, E.; Steinkuhler, J.; Ricken, J.; Wieneke, R.; Tampe, R.; Dimova, R.; Wegner, S. V., Dynamic blue light-switchable protein patterns on giant unilamellar vesicles. *Chem. Commun.* **2018**, *54*, 948-951.

109. Jia, H. Y.; Kai, L.; Heymann, M.; Garcia-Soriano, D. A.; Hartel, T.; Schwille, P., Light-induced printing of protein structures on membranes *in vitro*. *Nano Lett.* **2018**, *18*, 7133-7140.

110. Reuther, C.; Tucker, R.; Ionov, L.; Diez, S., Programmable patterning of protein bioactivity by visible light. *Nano Lett.* **2014**, *14*, 4050-4057.

111. Deisseroth, K.; Feng, G. P.; Majewska, A. K.; Miesenbock, G.; Ting, A.; Schnitzer, M. J., Next-generation optical technologies for illuminating genetically targeted brain circuits. *J. Neurosci.* **2006**, *26*, 10380-10386.

112. Muhlhauser, W. W.; Fischer, A.; Weber, W.; Radziwill, G., Optogenetics - Bringing light into the darkness of mammalian signal transduction. *Biochimica et biophysica acta. (BBA) Molecular cell research* **2017**, *1864*, 280-292.

113. Baaske, J.; Gonschorek, P.; Engesser, R.; Dominguez-Monedero, A.; Raute, K.; Fischbach, P.; Müller, K.; Cachat, E.; Schamel, W. W. A.; Minguet, S.; Davies, J. A.; Timmer, J.; Weber, W.; Zurbriggen, M. D., Dual-controlled optogenetic system for the rapid down-regulation of protein levels in mammalian cells. *Sci. Rep-Uk* **2018**, *8*, 15024.

114. Müller, K.; Weber, W., Optogenetic tools for mammalian systems. *Mol. BioSyst.* **2013**, *9*, 596-608.

115. Tischer, D.; Weiner, O. D., Illuminating cell signalling with optogenetic tools. *Nat. Rev.Mol. Cell Bio.* **2014**, *15*, 551-558.

116. Deisseroth, K., Optogenetics. *Nat. Methods* **2010**, *8*, 26.

117. Muller, K.; Weber, W., Optogenetic tools for mammalian systems. *Mol. Biosyst.* **2013**, *9*, 596-608.

118. Klug, G., Beyond catalysis: vitamin $B_{12}$ as a cofactor in gene regulation. *Mol. Microbiol.* **2014**, *91*, 635-640.

119. Cheng, Z.; Yamamoto, H.; Bauer, C. E., Cobalamin's (vitamin $B_{12}$) surprising function as a photoreceptor. *Trends Biochem. Sci.* **2016**, *41*, 647-650.

120. Jost, M.; Simpson, J. H.; Drennan, C. L., The transcription factor CarH safeguards use of adenosylcobalamin as a light sensor by altering the photolysis products. *Biochemistry-Us* **2015**, *54*, 3231-3234.

121. Jost, M.; Fernandez-Zapata, J.; Polanco, M. C.; Ortiz-Guerrero, J. M.; Chen, P. Y. T.; Kang, G.; Padmanabhan, S.; Elias-Arnanz, M.; Drennan, C. L., Structural basis for gene regulation by a $B_{12}$-dependent photoreceptor. *Nature* **2015**, *526*, 536-541.

122. Kutta, R. J.; Hardman, S. J. O.; Johannissen, L. O.; Bellina, B.; Messiha, H. L.; Ortiz-Guerrero, J. M.; Elias-Arnanz, M.; Padmanabhan, S.; Barran, P.; Scrutton, N. S.; Jones, A. R., The photochemical mechanism of a $B_{12}$-dependent photoreceptor protein. *Nat. Commun.* **2015,** *6*.

123. Marques, H. M.; Marsh, J. H.; Mellor, J. R.; Munro, O. Q., The coordination of imidazole and its derivatives by aquocobalamin. *Inorg. Chim. Acta* **1990**, *170*, 259-269.

124. Perez-Marin, M. C.; Padmanabhan, S.; Polanco, M. C.; Murillo, F. J.; Elias-Arnanz, M., Vitamin $B_{12}$ partners the CarH repressor to downregulate a photoinducible promoter in *Myxococcus xanthus*. *Mol. Microbiol.* **2008**, *67*, 804-819.

125. Ortiz-Guerrero, J. M.; Polanco, M. C.; Murillo, F. J.; Padmanabhan, S.; Elias-Arnanz, M., Light-dependent gene regulation by a coenzyme $B_{12}$-based photoreceptor. *Proc. Natl. Acad. Sci. USA* **2011**, *108*, 7565-7570.

126. Wang, R.; Yang, Z. G.; Luo, J. R.; Hsing, I. M.; Sun, F., $B_{12}$-dependent photoresponsive protein hydrogels for controlled stem cell/protein release. *Proc. Natl. Acad. Sci. USA* **2017**, *114*, 5912-5917.

127. Kainrath, S.; Stadler, M.; Reichhart, E.; Distel, M.; Janovjak, H., Green light induced inactivation of receptor signaling using cobalamin-binding domains. *Angew. Chem. Int. Ed.* **2017**, *56*, 4608-4611.

128. Gruber, K.; Krautler, B., Coenzyme $B_{12}$ repurposed for photoregulation of gene expression. *Angew. Chem. Int. Ed.* **2016**, *55*, 5638-5640.

129. Muller, K.; Weber, W., Optogenetic tools for mammalian systems. *Mol. Biosyst.* **2013**, *9*, 596-608.

130. Pudasaini, A.; El-Arab, K. K.; Zoltowski, B. D., LOV-based optogenetic devices: light-driven modules to impart photoregulated control of cellular signaling. *Front. Mol. Biosci.* **2015**, *2*, 18.

131. Kennis, J. T. M., van Stokkum, I. H. M., Crosson, S., Gauden, M., Moffat, K. and van Grondelle, R., The LOV2 domain of phototropin: a reversible photochromic switch. *J. Am. Chem. Soc.* **2004**, *126*, 4512-4513.

132. Seifert, S.; Brakmann, S., LOV domains in the design of photoresponsive enzymes. *ACS Chem. Biol.* **2018**, *13*, 1914-1920.

133. Moglich, A.; Ayers, R. A.; Moffat, K., Structure and signaling mechanism of Per-ARNT-Sim domains. *Structure* **2009**, *17*, 1282-1294.

134. Kritsky, M. S.; Telegina, T. A.; Vechtomova, Y. L.; Buglak, A. A., Why flavins are not competitors of chlorophyll in the evolution of biological converters of solar energy. *Int. J. Mol. Sci.* **2013**, *14*, 575-593.

135. Pudasaini, A.; El-Arab, K. K.; Zoltowski, B. D., LOV-based optogenetic devices: light-driven modules to impart photoregulated control of cellular signaling. *Front. Mol. Biosci.* **2015**, *2*, 18.

136. Zoltowski, B. D.; Gardner, K. H., Tripping the light fantastic: blue-light photoreceptors as examples of environmentally modulated protein-protein interactions. *Biochemistry-Us* **2011**, *50*, 4-16.

137. Zimmerman, S. P.; Hallett, R. A.; Bourke, A. M.; Bear, J. E.; Kennedy, M. J.; Kuhlman, B., Tuning the binding affinities and reversion kinetics of a light inducible dimer allows control of transmembrane protein localization. *Biochemistry* **2016**, *55*, 5264-5271.

138. Zimmerman, S. P.; Asokan, S. B.; Kuhlman, B.; Bear, J. E., Cells lay their own tracks - optogenetic Cdc42 activation stimulates fibronectin deposition supporting directed migration. *J. Cell Sci.* **2017**, *130*, 2971-2983.

139. Yumerefendi, H.; Lerner, A. M.; Zimmerman, S. P.; Hahn, K.; Bear, J. E.; Strahl, B. D.; Kuhlman, B., Light-induced nuclear export reveals rapid dynamics of epigenetic modifications. *Nat. Chem. Biol.* **2016**, *12*, 399-401.

140. Adikes, R. C.; Hallett, R. A.; Saway, B. F.; Kuhlman, B.; Slep, K. C., Control of microtubule dynamics using an optogenetic microtubule plus end-F-actin cross-linker. *J. Cell Biol.* **2017**, *217*, 779-793.

141. Guntas, G.; Hallett, R. A.; Zimmerman, S. P.; Williams, T.; Yumerefendi, H.; Bear, J. E.; Kuhlman, B., Engineering an improved light-induced dimer (iLID) for controlling the localization and activity of signaling proteins. *Proc. Natl. Acad. Sci. USA* **2015**, *112*, 112-117.

142. Johnson, H. E.; Goyal, Y.; Pannucci, N. L.; Schupbach, T.; Shvartsman, S. Y.; Toettcher, J. E., The spatiotemporal limits of developmental erk signaling. *Dev. Cell* **2017**, *40*, 185-192.

143. Hallett, R. A.; Zimmerman, S. P.; Yumerefendi, H.; Bear, J. E.; Kuhlman, B., Correlating *in vitro* and *in vivo* activities of light-inducible dimers: a cellular optogenetics guide. *ACS Synth. Biol.* **2016**, *5*, 53-64.

144. O'Neill, P. R.; Kalyanaraman, V.; Gautam, N., Subcellular optogenetic activation of Cdc42 controls local and distal signaling to drive immune cell migration. *Mol. Biol. Cell* **2016**, *27*, 1442-1450.

145. O'Neill, P. R.; Castillo-Badillo, J. A.; Meshik, X.; Kalyanaraman, V.; Melgarejo, K.; Gautam, N., Membrane flow drives an adhesion-independent amoeboid cell migration mode. *Dev. Cell* **2018**, *46*, 9-22.

146. Yu, Q.; Wang, Y.; Zhao, S.; Ren, Y., Photocontrolled reversible self-assembly of dodecamer nitrilase. *Bioresour. Bioprocess* **2017**, *4*, 36.

147. Nakamura, H.; Lee, A. A.; Afshar, A. S.; Watanabe, S.; Rho, E.; Razavi, S.; Suarez, A.; Lin, Y. C.; Tanigawa, M.; Huang, B.; DeRose, R.; Bobb, D.; Hong, W.; Gabelli, S. B.; Goutsias, J.; Inoue, T., Intracellular production of hydrogels and synthetic RNA granules by multivalent molecular interactions. *Nat. Mater.* **2018**, *17*, 79-89.

148. Green, N. M., Avidin and streptavidin. *Method Enzym.* **1990**, *184*, 51-67.

149. Liu, F. J.; Zhang, J. Z. H.; Mei, Y., The origin of the cooperativity in the streptavidin-biotin system: A computational investigation through molecular dynamics simulations. *Sci. Rep-Uk* **2016**, *6*.

150. DeChancie, J.; Houk, K. N., The origins of femtomolar protein-ligand binding: Hydrogen-bond cooperativity and desolvation energetics in the biotin-(strept)avidin binding site. *J. Am. Chem. Soc.* **2007**, *129*, 5419-5429.

151. Goujon, A.; Strakova, K.; Sakai, N.; Matile, S., Streptavidin interfacing as a general strategy to localize fluorescent membrane tension probes in cells. *Chem. Sci.* **2019**, *10*, 310-319.

152. Wu, Y. P.; Chew, C. Y.; Li, T. N.; Chung, T. H.; Chang, E. H.; Lam, C. H.; Tan, K. T., Target-activated streptavidin-biotin controlled binding probe. *Chem. Sci.* **2018**, *9*, 770-776.

153. Pollheimer, P.; Taskinen, B.; Scherfler, A.; Gusenkov, S.; Creus, M.; Wiesauer, P.; Zauner, D.; Schotherger, W.; Schwarzinger, C.; Ebner, A.; Tampe, R.; Stutz, H.; Hytonen, V. P.; Gruber, H. J., Reversible biofunctionalization of surfaces with a switchable mutant of avidin. *Bioconjugate Chem.* **2013**, *24*, 1656-1668.

154. Dundas, C. M.; Demonte, D.; Park, S., Streptavidin-biotin technology: improvements and innovations in chemical and biological applications. *Appl. Microbiol. Biot.* **2013**, *97*, 9343-9353.

155. Migliorini, E.; Horn, P.; Haraszti, T.; Wegner, S. V.; Hiepen, C.; Knaus, P.; Richter, R. P.; Cavalcanti-Adam, E. A., Enhanced biological activity of BMP-2 bound to surface-grafted heparan sulfate. *Adv. Biosyst.* **2017**, *1*, 1600041.

156. Mann, J. K.; Demonte, D.; Dundas, C. M.; Park, S., Cell labeling and proximity dependent biotinylation with engineered monomeric streptavidin. *Technology* **2016**, *4*, 152-158.

157. Liang, A. D.; Serrano-Plana, J.; Peterson, R. L.; Ward, T. R., Artificial metalloenzymes based on the biotin-streptavidin technology: enzymatic cascades and directed evolution. *Acc. Chem. Res.* **2019**, *52*, 585-595.

158. Kim, M.; Wang, C. C.; Benedetti, F.; Marszalek, P. E., A nanoscale force probe for gauging intermolecular interactions. *Angew. Chem. Int. Ed.* **2012**, *51*, 1903-1906.

159. Kuan, S. L.; Ng, D. Y. W.; Wu, Y. Z.; Fortsch, C.; Barth, H.; Doroshenko, M.; Koynov, K.; Meier, C.; Weil, T., pH responsive janus-like supramolecular fusion proteins for functional protein delivery. *J. Am. Chem. Soc.* **2013**, *135*, 17254-17257.

160. Kurdekar, A. D.; Chunduri, L. A. A.; Manohar, C. S.; Haleyurgirisetty, M. K.; Hewlett, I. K.; Venkataramaniah, K., Streptavidin-conjugated gold nanoclusters as ultrasensitive fluorescent sensors for early diagnosis of HIV infection. *Sci. Adv.* **2018**, *4*.

161. Howarth, M.; Chinnapen, D. J. F.; Gerrow, K.; Dorrestein, P. C.; Grandy, M. R.; Kelleher, N. L.; El-Husseini, A.; Ting, A. Y., A monovalent streptavidin with a single femtomolar biotin binding site. *Nat. Methods* **2006**, *3*, 267-273.

162. Lemercier, G.; Johnsson, K., Chimeric streptavidins with reduced valencies. *Nat. Methods* **2006**, *3*, 247-248.

163. Lee, J. M.; Kim, J. A.; Yen, T. C.; Lee, I. H.; Ahn, B.; Lee, Y.; Hsieh, C. L.; Kim, H. M.; Jung, Y., A rhizavidin monomer with nearly multimeric avidin-like binding stability against biotin conjugates. *Angew. Chem. Int. Ed.* **2016**, *55*, 3393-3397.

164. Chamma, I.; Letellier, M.; Butler, C.; Tessier, B.; Lim, K. H.; Gauthereau, I.; Choquet, D.; Sibarita, J. B.; Park, S.; Sainlos, M.; Thoumine, O., Mapping the dynamics and nanoscale organization of synaptic adhesion proteins using monomeric streptavidin. *Nat Commun* **2016**, *7*.

165. Howarth, M.; Ting, A. Y., Imaging proteins in live mammalian cells with biotin ligase and monovalent streptavidin. *Nat. Protoc.* **2008**, *3*, 534-545.

166. Howarth, M.; Liu, W. H.; Puthenveetil, S.; Zheng, Y.; Marshall, L. F.; Schmidt, M. M.; Wittrup, K. D.; Bawendi, M. G.; Ting, A. Y., Monovalent, reduced-size quantum dots for imaging receptors on living cells. *Nat. Methods* **2008**, *5*, 397-399.

167. Pasqualini, R.; Ruoslahti, E., Organ targeting *in vivo* using phage display peptide libraries. *Nature* **1996**, *380*, 364-366.

168. Oh, I. K.; Mok, H.; Park, T. G., Folate immobilized and PEGylated adenovirus for retargeting to tumor cells. *Bioconjugate Chem.* **2006**, *17*, 721-727.

169. Heck, A. J.; Ostertag, T.; Schnell, L.; Fischer, S.; Agrawalla, B. K.; Winterwerber, P.; Wirsching, E.; Fauler, M.; Frick, M.; Kuan, S. L.; Weil, T.; Barth, H., Supramolecular toxin complexes for targeted pharmacological modulation of polymorphonuclear leukocyte functions. *Adv. Healthca. Mater.* **2019**, *8*, 1900665.

170. Kim, Y. Y.; Bang, Y.; Lee, A. H.; Song, Y. K., Multivalent traptavidin-DNA conjugates for the programmable assembly of nanostructures. *ACS Nano* **2019**, *13*, 1183-1194.

171. Porath, J.; Carlsson, J.; Olsson, I.; Belfrage, G., Metal chelate affinity chromatography, a new approach to protein fractionation. *Nature* **1975**, *258*, 598-599.

172. Hochuli, E.; Dobeli, H.; Schacher, A., New metal chelate adsorbent selective for proteins and peptides containing neighboring histidine-residues. *J. Chromatogr.* **1987**, *411*, 177-184.

173. Hochuli, E.; Bannwarth, W.; Dobeli, H.; Gentz, R.; Stuber, D., Genetic approach to facilitate purification of recombinant proteins with a novel metal chelate adsorbent. *Bio-Technol.* **1988**, *6*, 1321-1325.

174. Gautrot, J. E.; Huck, W. T. S.; Welch, M.; Ramstedt, M., Protein-resistant NTA-functionalized polymer brushes for selective and stable immobilization of histidine-tagged proteins. *ACS Appl. Mater. Inter.* **2010**, *2*, 193-202.

175. Kim, M. J.; Park, H. Y.; Kim, J.; Ryu, J.; Hong, S.; Han, S. J.; Song, R., Western blot analysis using metal-nitrilotriacetate conjugated CdSe/ZnS quantum dots. *Anal. Biochem.* **2008**, *379*, 124-126.

176. Boeneman, K.; Delehanty, J. B.; Susumu, K.; Stewart, M. H.; Medintz, I. L., Intracellular bioconjugation of targeted proteins with semiconductor quantum dots. *J. Am. Chem. Soc.* **2010**, *132*, 5975-5977.

177. Chen, F.; Wegner, S. V., Blue light switchable bacterial adhesion as a key step toward the design of biofilms. *ACS Synth. Biol.* **2017**, *6*, 2170-2174.

178. Kang, E.; Park, J. W.; McClellan, S. J.; Kim, J. M.; Holland, D. P.; Lee, G. U.; Franses, E. I.; Park, K.; Thompson, D. H., Specific adsorption of histidine-tagged proteins on silica surfaces modified with $Ni^{2+}$/NTA-derivatized poly(ethylene glycol). *Langmuir* **2007**, *23*, 6281-6288.

179. Grunwald, C.; Schulze, K.; Reichel, A.; Weiss, V. U.; Blaas, D.; Piehler, J.; Wiesmuller, K. H.; Tampe, R., In situ assembly of macromolecular complexes triggered by light. *Proc. Natl. Acad. Sci. USA* **2010**, *107*, 6146-6151.

180. Xu, D. D.; Bartelt, S. M.; Rasoulinejad, S.; Chen, F.; Wegner, S. V., Green light lithography: a general strategy to create active protein and cell micropatterns. *Mater. Horiz.* **2019**, *6*, 1222-1229.

181. Chervyachkova, E.; Wegner, S. V., Reversible social self-sorting of colloidal cell-mimics with blue Light switchable proteins. *ACS Synth. Biol.* **2018**, *7*, 1817-1824.

182. Valiokas, R.; Klenkar, G.; Tinazli, A.; Tampe, R.; Liedberg, B.; Piehler, J., Differential protein assembly on micropatterned surfaces with tailored molecular and surface multivalency. *Chembiochem* **2006**, *7*, 1325-1329.

183. Rusmini, F.; Zhong, Z. Y.; Feijen, J., Protein immobilization strategies for protein biochips. *Biomacromolecules* **2007**, *8*, 1775-1789.

184. Kamoto, M.; Umezawa, N.; Kato, N.; Higuchi, T., Novel probes showing specific fluorescence enhancement on binding to a hexahistidine tag. *Chem-Eur. J.* **2008**, *14*, 8004-8012.

185. Soh, N., Selective chemical labeling of proteins with small fluorescent molecules based on metal-chelation methodology. *Sensors-Basel.* **2008**, *8*, 1004-1024.

186. Goldsmith, C. R.; Jaworski, J.; Sheng, M.; Lippard, S. J., Selective labeling of extracellular proteins containing polyhistidine sequences by a fluorescein - Nitrilotriacetic acid conjugate. *J. Am. Chem. Soc.* **2006**, *128*, 418-419.

187. Guignet, E. G.; Hovius, R.; Vogel, H., Reversible site-selective labeling of membrane proteins in live cells. *Nat. Biotechnol.* **2004**, *22* (4), 440-444.

188. Wegner, S. V.; Schenk, F. C.; Witzel, S.; Bialas, F.; Spatz, J. P., Cobalt cross-linked redox-responsive PEG hydrogels: from viscoelastic liquids to elastic solids. *Macromolecules* **2016**, *49*, 4229-4235.

189. Pires, M. M.; Ernenwein, D.; Chmielewski, J., Selective decoration and release of his-tagged proteins from metal-assembled collagen peptide microflorettes. *Biomacromolecules* **2011**, *12*, 2429-2433.

190. Schmitt, L.; Dietrich, C.; Tampe, R., Synthesis and characterization of chelator-lipids for reversible immobilization of engineered proteins at self-assembled lipid interfaces. *J. Am. Chem. Soc.* **1994**, *116*, 8485-8491.

191. Gavutis, M.; Lata, S.; Piehler, J., Probing 2-dimensional protein-protein interactions on model membranes. *Nat. Protoc.* **2006**, *1*, 2091-2103.

192. Mirkovic, T.; Ostroumov, E. E.; Anna, J. M.; van Grondelle, R.; Govindjee; Scholes, G. D., Light absorption and energy transfer in the antenna complexes of photosynthetic organisms. *Chem. Rev.* **2017**, *117*, 249-293.

193. Burn, R.; Misson, L.; Meury, M.; Seebeck, F. P., Anaerobic origin of ergothioneine. *Angew. Chem. Int. Ed.* **2017**, *56*, 12508-12511.

194. Schwille, P., Bottom-up synthetic biology: engineering in a tinkerer's world. *Science* **2011**, *333*, 1252-1254.

195. Trantidou, T.; Friddin, M.; Elani, Y.; Brooks, N. J.; Law, R. V.; Seddon, J. M.; Ces, O., Engineering compartmentalized biomimetic micro- and nanocontainers. *ACS Nano* **2017**, *11*, 6549-6565.

196. Sikkema, H. R.; Gaastra, B. F.; Pols, T.; Poolman, B., Cell fuelling and metabolic energy conservation in synthetic cells. *Chembiochem* **2019**, *20*, 2581-2592.

197. Berhanu, S.; Ueda, T.; Kuruma, Y., Artificial photosynthetic cell producing energy for protein synthesis. *Nat. Commun.* **2019**, *10*.

198. Kurihara, K.; Okura, Y.; Matsuo, M.; Toyota, T.; Suzuki, K.; Sugawara, T., A recursive vesicle-based model protocell with a primitive model cell cycle. *Nat. Commun.* **2015**, *6*.

199. Li, M.; Huang, X.; Mann, S., Spontaneous growth and division in self-reproducing inorganic colloidosomes. *Small* **2014**, *10*, 3291-3298.

200. Krinsky, N.; Kaduri, M.; Zinger, A.; Shainsky-Roitman, J.; Goldfeder, M.; Benhar, I.; Hershkovitz, D.; Schroeder, A., Synthetic cells synthesize therapeutic proteins inside tumors. *Adv. Healthca. Mater.* **2018**, *7*, 1701163.

201. Broz, P.; Driamov, S.; Ziegler, J.; Ben-Haim, N.; Marsch, S.; Meier, W.; Hunziker, P., Toward intelligent nanosize bioreactors: A pH-switchable, channel-equipped, functional polymer nanocontainer. *Nano Lett.* **2006**, *6*, 2349-2353.

202. Garamella, J.; Majumder, S.; Liu, A. P.; Noireaux, V., An adaptive synthetic cell based on mechanosensing, biosensing, and inducible gene circuits. *ACS Synth. Biol.* **2019**, *8*, 1913-1920.

203. Karig, D. K., Cell-free synthetic biology for environmental sensing and remediation. *Curr. Opin. Biotech.* **2017**, *45*, 69-75.

204. Ruprecht, V.; Monzo, P.; Ravasio, A.; Yue, Z.; Makhija, E.; Strale, P. O.; Gauthier, N.; Shivashankar, G. V.; Studer, V.; Albiges-Rizo, C.; Viasnoff, V., How cells respond to environmental cues- insights from bio-functionalized substrates. *J. Cell Sci.* **2017**, *130*, 51-61.

205. Bartelt, S. M.; Chervyachkova, E.; Ricken, J.; Wegner, S. V., Mimicking adhesion in minimal synthetic cells. *Adv. Biosyst.* **2019**, *3*, 1800333.

206. Ko, Y. H.; Hong, S. J.; Pedersen, P. L., Chemical mechanism of ATP synthase - magnesium plays a pivotal role in formation of the transition state where ATP is synthesized from ADP and inorganic phosphate. *J. Biol. Chem.* **1999**, *274*, 28853-28856.

207. Guntas, G.; Hallett, R. A.; Zimmerman, S. P.; Williams, T.; Yumerefendi, H.; Bear, J. E.; Kuhlman, B., Engineering an improved light-induced dimer (iLID) for controlling the localization and activity of signaling proteins. *Proc. Natl. Acad. Sci. USA* **2015**, *112*, 112-117.

208. Lungu, O. I.; Hallett, R. A.; Choi, E. J.; Aiken, M. J.; Hahn, K. M.; Kuhlman, B., Designing photoswitchable peptides ssing the AsLOV2 domain. *Chem. Biol.* **2012**, *19*, 507-517.

209. Wegner, S. V.; Schenk, F. C.; Spatz, J. P., Cobalt(III)-mediated permanent and stable immobilization of histidine-tagged proteins on NTA-functionalized surfaces. *Chem-Eur. J.* **2016**, *22*, 3156-3162.

210. Wagner, N.; Gutweiler, M.; Pabst, R.; Dose, K., Coreconstitution of bacterial ATP synthase with monomeric bacteriorhodopsin into liposomes - a comparison between the efficiency of monomeric bacteriorhodopsin and purple membrane patches in coreconstitution experiments. *Eur. J. Biochem.* **1987**, *165*, 177-183.

211. Richard, P.; Graber, P., Kinetics of ATP synthesis catalyzed by the $H^+$-ATPase from chloroplasts ($Cf_of_1$) reconstituted into liposomes and coreconstituted with bacteriorhodopsin. *Eur. J. Biochem.* **1992**, *210*, 287-291.

212. Wu, J.; Liow, C.; Tao, K.; Guo, Y. Y.; Wang, X. T.; Miao, J. M., Large-area sub-wavelength optical patterning via long-range ordered polymer lens array. *ACS Appl. Mater. Inter.* **2016**, *8*, 16368-16378.

213. Wu, J.; Miao, J. M., Production of centimeter-scale gradient patterns by graded elastomeric tip array. *ACS Appl. Mater. Inter.* **2015**, *7*, 6991-7000.

214. Wu, J.; Yu, C. H.; Li, S. Z.; Zou, B. H.; Liu, Y. Y.; Zhu, X. Q.; Guo, Y. Y.; Xu, H. B.; Zhang, W. N.; Zhang, L. P.; Liu, B.; Tian, D. B.; Huang, W.; Sheetz, M. P.; Huo, F. W., Parallel near-field photolithography with metal-coated elastomeric masks. *Langmuir* **2015**, *31*, 1210-1217.

215. Mironi-Harpaz, I.; Hazanov, L.; Engel, G.; Yelin, D.; Seliktar, D., In-situ architectures designed in 3D cell-laden hydrogels using microscopic laser photolithography. *Adv. Mater.* **2015**, *27*, 1933-1938.

216. Lee, E. K.; Park, C. H.; Lee, J.; Lee, H. R.; Yang, C.; Oh, J. H., Chemically robust ambipolar organic transistor array directly patterned by photolithography. *Adv. Mater.* **2017**, *29*, 1605282.

217. Choe, J. H.; Park, Q. H.; You, E. A., Rational and facile construction of 3D annular nanostructures with tunable layers by exploiting the diffraction and interference of light. *Adv. Funct. Mater.* **2016**, *26*, 5203-5210.

218. Yamaguchi, M.; Nishimura, O.; Lim, S. H.; Shimokawa, K.; Tamura, T.; Suzuki, M., Protein patterning using a microstructured organosilane layer fabricated by VUV light lithography as a template. *Colloid Surf. A* **2006**, *284*, 532-534.

219. Allen, R. D., Trends in patterning materials for advanced lithography. *J. Photopolym. Sci. Tec.* **2007**, *20*, 453-455.

220. Bhagawati, M.; Lata, S.; Tampe, R.; Piehler, J., Native laser lithography of his-tagged proteins by uncaging of multivalent chelators. *J. Am. Chem. Soc.* **2010**, *132*, 5932-5933.

221. Terai, T.; Maki, E.; Sugiyama, S.; Takahashi, Y.; Matsumura, H.; Mori, Y.; Nagano, T., Rational development of caged-biotin protein-labeling agents and some applications in live cells. *Chem. Biol.* **2011**, *18*, 1261-1272.

222. Chen, X.; Venkatachalapathy, M.; Kamps, D.; Weigel, S.; Kumar, R.; Orlich, M.; Garrecht, R.; Hirtz, M.; Niemeyer, C. M.; Wu, Y. W.; Dehmelt, L., "Molecular activity painting": Switch-like, light-controlled perturbations inside living cells. *Angew. Chem. Int. Ed.* **2017**, *56*, 5916-5920.

223. Auernheimer, J.; Dahmen, C.; Hersel, U.; Bausch, A.; Kessler, H., Photoswitched cell adhesion on surfaces with RGD peptides. *J. Am. Chem. Soc.* **2005**, *127*, 16107-16110.

224. Kadem, L. F.; Holz, M.; Suana, K. G.; Li, Q.; Lamprecht, C.; Herges, R.; Selhuber-Unkel, C., Rapid reversible photoswitching of integrin-mediated adhesion at the single-cell level. *Adv. Mater.* **2016**, *28*, 1799-1802.

225. Tischer, D.; Weiner, O. D., Illuminating cell signalling with optogenetic tools. *Nat. Rev. Mol. Cell Bio.* **2014**, *15*, 551-558.

226. Liu, X. T.; Yang, X.; Yang, Z. G.; Luo, J. R.; Tian, X. Z.; Liu, K.; Kou, S. Z.; Sun, F., Versatile engineered protein hydrogels enabling decoupled mechanical and biochemical tuning for cell adhesion and neurite growth. *ACS Appl. Nano Mater.* **2018**, *1*, 1579-1585.

227. Lyu, S. S.; Fang, J.; Duan, T. Y.; Fu, L. L.; Liu, J. Q.; Li, H. B., Optically controlled reversible protein hydrogels based on photoswitchable fluorescent protein Dronpa. *Chem. Commun.* **2017**, *53*, 13375-13378.

228. Richardson, J. J.; Bjornmalm, M.; Caruso, F., Technology-driven layer-by-layer assembly of nanofilms. *Science* **2015**, *348*.

229. Deshmukh, P. K.; Ramani, K. P.; Singh, S. S.; Tekade, A. R.; Chatap, V. K.; Patil, G. B.; Bari, S. B., Stimuli-sensitive layer-by-layer (LbL) self-assembly systems: Targeting and biosensory applications. *J. Control. Release* **2013**, *166*, 294-306.

230. Pires, M. M.; Chmielewski, J., Self-assembly of collagen peptides into microflorettes via metal coordination. *J. Am. Chem. Soc.* **2009**, *131*, 2706-2712.

231. Hernandez-Gordillo, V.; Chmielewski, J., Mimicking the extracellular matrix with functionalized, metal-assembled collagen peptide scaffolds. *Biomaterials* **2014**, *35*, 7363-7373.

232. Kubow, K. E.; Vukmirovic, R.; Zhe, L.; Klotzsch, E.; Smith, M. L.; Gourdon, D.; Luna, S.; Vogel, V., Mechanical forces regulate the interactions of fibronectin and collagen I in extracellular matrix. *Nat. Commun.* **2015**, *6*.

233. Iskratsch, T.; Wolfenson, H.; Sheetz, M. P., Appreciating force and shape - the rise of mechanotransduction in cell biology. *Nat. Rev. Mol. Cell Bio.* **2014**, *15*, 825-833.

234. Dix, C. L.; Matthews, H. K.; Uroz, M.; McLaren, S.; Wolf, L.; Heatley, N.; Win, Z.; Almada, P.; Henriques, R.; Boutros, M.; Trepat, X.; Baum, B., The role of mitotic cell-substrate adhesion re-modeling in animal cell division. *Dev. Cell* **2018**, *45*, 132-145.

235. Tjong, W. Y.; Lin, H. H., The RGD motif is involved in CD97/ADGRE5-promoted cell adhesion and viability of HT1080 cells. *Sci. Rep-Uk* **2019**, *9*.

236. Cui, J. X.; San Miguel, V.; del Campo, A., Light-triggered multifunctionality at surfaces mediated by photolabile protecting groups. *Macromol. Rapid Commun.* **2013**, *34*, 310-329.

237. Matsuda, N.; Shimizu, T.; Yamato, M.; Okano, T., Tissue engineering based on cell sheet technology. *Adv. Mater.* **2007**, *19* (20), 3089-3099.

238. Li, W.; Wang, J. S.; Ren, J. S.; Qu, X. G., Near-infrared and pH-responsive system for reversible cell adhesion using graphene/gold Nanorods functionalized with i-Motif DNA. *Angew. Chem. Int. Ed.* **2013**, *52*, 6726-6730.

239. Ng, C. C. A.; Magenau, A.; Ngalim, S. H.; Ciampi, S.; Chockalingham, M.; Harper, J. B.; Gaus, K.; Gooding, J. J., Using an electrical potential to reversibly switch surfaces between two states for dynamically controlling cell adhesion. *Angew. Chem. Int. Ed.* **2012**, *51*, 7706-7710.

240. Ren, T. C.; Ni, Y. L.; Du, W.; Yu, S.; Mao, Z. W.; Gao, C. Y., Dual responsive surfaces based on host-guest interaction for dynamic mediation of cell-substrate interaction and cell migration. *Adv. Mater. Interfaces* **2017**, *4*, 1500865.

241. Shi, P.; Ju, E. G.; Wang, J. S.; Yan, Z. Q.; Ren, J. S.; Qu, X. G., Host-guest recognition on photo-responsive cell surfaces directs cell-cell contacts. *Mater. Today* **2017**, *20*, 16-21.

242. Bian, Q.; Wang, W. S.; Wang, S. T.; Wang, G. J., Light-triggered specific cancer cell release from cyclodextrin/azobenzene and aptamer-modified substrate. *ACS Appl. Mater. Inter.* **2016**, *8*, 27360-27367.

243. Lee, I. N.; Dobre, O.; Richards, D.; Ballestrem, C.; Curran, J. M.; Hunt, J. A.; Richardson, S. M.; Swift, J.; Wong, L. S., Photoresponsive hydrogels with photoswitchable mechanical properties allow time-resolved analysis of cellular responses to matrix stiffening. *ACS Appl. Mater. Inter.* **2018**, *10*, 7765-7776.

244. Farrukh, A.; Fan, W. Q.; Zhao, S. F.; Salierno, M.; Paez, J. I.; del Campo, A., Photoactivatable adhesive ligands for light-guided neuronal growth. *Chembiochem* **2018**, *19*, 1271-1279.

245. Han, K.; Yin, W. N.; Fan, J. X.; Cao, F. Y.; Zhang, X. Z., Photo-activatable substrates for site-specific differentiation of stem cells. *ACS Appl. Mater. Inter.* **2015**, *7*, 23679-23684.

246. Weis, S.; Lee, T. T.; del Campo, A.; Garcia, A. J., Dynamic cell-adhesive microenvironments and their effect on myogenic differentiation. *Acta Biomater.* **2013**, *9*, 8059-8066.

247. Nakanishi, J.; Kikuchi, Y.; Takarada, T.; Nakayama, H.; Yamaguchi, K.; Maeda, M., Photoactivation of a substrate for cell adhesion under standard fluorescence microscopes. *J. Am. Chem. Soc.* **2004**, *126*, 16314-16315.

248. Li, W.; Wang, J. S.; Ren, J. S.; Qu, X. G., Near-infrared upconversion controls photocaged cell adhesion. *J. Am. Chem. Soc.* **2014**, *136*, 2248-2251.

249. Li, W.; Chen, Z. W.; Zhou, L.; Li, Z. H.; Ren, J. S.; Qu, X. G., Noninvasive and reversible cell adhesion and detachment via single-wavelength near-infrared laser mediated photoisomerization. *J. Am. Chem. Soc.* **2015**, *137*, 8199-8205.

250. Liu, D. B.; Xie, Y. Y.; Shao, H. W.; Jiang, X. Y., Using azobenzene-embedded self-assembled monolayers to photochemically control cell adhesion reversibly. *Angew. Chem. Int. Ed.* **2009**, *48*, 4406-4408.

251. Goulet-Hanssens, A.; Sun, K. L. W.; Kennedy, T. E.; Barrettt, C. J., Photoreversible surfaces to regulate cell adhesion. *Biomacromolecules* **2012**, *13*, 2958-2963.

252. Wu, X.; Huang, W. M.; Wu, W. H.; Xue, B.; Xiang, D. F.; Li, Y.; Qin, M.; Sun, F.; Wang, W.; Zhang, W. B.; Cao, Y., Reversible hydrogels with tunable mechanical properties for optically controlling cell migration. *Nano Res.* **2018**, *11*, 5556-5565.

253. Yang, Z.; Yang, Y.; Wang, M.; Wang, T.; Fok, H. K. F.; Jiang, B.; Xiao, W.; Kou, S.; Guo, Y.; Yan, Y.; Deng, X.; Zhang, W.-B.; Sun, F., Dynamically tunable, macroscopic molecular networks enabled by cellular synthesis of 4-arm star-like proteins. *Matter* **2020**, *2*, 233-249.

254. Horner, M.; Raute, K.; Hummel, B.; Madl, J.; Creusen, G.; Thomas, O. S.; Christen, E. H.; Hotz, N.; Gubeli, R. J.; Engesser, R.; Rebmann, B.; Lauer, J.; Rolauffs, B.; Timmer, J.; Schamel, W. W. A.; Pruszak, J.; Romer, W.; Zurbriggen, M. D.; Friedrich, C.; Walther, A.; Minguet, S.; Sawarkar, R.; Weber, W., Phytochrome-based extracellular matrix with reversibly tunable mechanical properties. *Adv. Mater.* **2019**, *31*, 1806727.

255. Baaske, J.; Muhlhauser, W. W. D.; Yousefi, O. S.; Zanner, S.; Radziwill, G.; Horner, M.; Schamel, W. W. A.; Weber, W., Optogenetic control of integrin-matrix interaction. *Commun. Biol.* **2019**, *2*, 1-8.

256. Yuz, S. G.; Ricken, J.; Wegner, S. V., Independent control over multiple cell types in space and time using orthogonal blue and red light switchable cell interactions. *Adv. Sci.* **2018,** *5*, 1800446.

257. Hytonen, V. P.; Nordlund, H. R.; Horha, J.; Nyholm, T. K. M.; Hyre, D. E.; Kulomaa, H.; Porkka, N. J.; Marttila, A. T.; Stayton, P. S.; Laitinen, O. H.; Kulomaa, M. S., Dual-affinity avidin molecules. *Proteins* **2005**, *61*, 597-607.

258. Leppiniemi, J.; Maatta, J. A. E.; Hammaren, H.; Soikkeli, M.; Laitaoja, M.; Janis, J.; Kulomaa, M. S.; Hytonen, V. P., Bifunctional avidin with covalently modifiable ligand binding site. *Plos One* **2011**, *6*.

259. Gruber, H. J.; Kada, G.; Marek, M.; Kaiser, K., Accurate titration of avidin and streptavidin with biotin-fluorophore conjugates in complex, colored biofluids. *Bba-Gen Subjects* **1998**, *1381*, 203-212.

260. Mittal, R.; Bruchez, M. P., Biotin-4-fluorescein based fluorescence quenching assay for determination of biotin binding capacity of streptavidin conjugated quantum dots. *Bioconjugate Chem.* **2011**, *22*, 362-368.

261. Reznik, G. O.; Vajda, S.; Sano, T.; Cantor, C. R., A streptavidin mutant with altered ligand-binding specificity. *Proc. Natl. Acad. Sci. USA* **1998**, *95*, 13525-13530.

262. Gaberc-Porekar, V.; Menart, V., Potential for using histidine tags in purification of proteins at large scale. *Chem. Eng. Technol.* **2005**, *28*, 1306-1314.

263. Chen, Y.; Cao, W. B.; Zhou, J. L.; Pidhatika, B.; Xiong, B.; Huang, L.; Tian, Q.; Shu, Y. W.; Wen, W. J.; Hsing, I. M.; Wu, H. K., Poly(L-lysine)-graft-folic acid-coupled poly(2-methyl-2-oxazoline) (PLL-g-PMOXA-c-FA): A bioactive copolymer for specific targeting to folate receptor-positive cancer cells. *ACS Appl. Mater. Inter.* **2015**, *7*, 2919-2930.

264. Park, Y. H.; Park, S. Y.; In, I., Direct noncovalent conjugation of folic acid on reduced graphene oxide as anticancer drug carrier. *J. Ind. Eng. Chem.* **2015**, *30*, 190-196.

265. Ma, Y.; Sadoqi, M.; Shao, J., Biodistribution of indocyanine green-loaded nanoparticles with surface modifications of PEG and folic acid. *Int. J. Pharmaceut* **2012**, *436*, 25-31.

266. Fairhead, M.; Veggiani, G.; Lever, M.; Yan, J.; Mesner, D.; Robinson, C. V.; Dushek, O.; van der Merwe, P. A.; Howarth, M., SpyAvidin hubs enable precise and ultrastable orthogonal nanoassembly. *J. Am. Chem. Soc.* **2014**, *136*, 12355-12363.

267. Dubacheva, G. V.; Araya-Callis, C.; Volbeda, A. G.; Fairhead, M.; Codee, J.; Howarth, M.; Richter, R. P., Controlling multivalent binding through surface chemistry: model study on streptavidin. *J. Am. Chem. Soc.* **2017**, *139*, 4157-4167.

268. Destito, G.; Yeh, R.; Rae, C. S.; Finn, M. G.; Manchester, M., Folic acid-mediated targeting of cowpea mosaic virus particles to tumor cells. *Chem. Biol.* **2007**, *14*, 1152-1162.

269. Xue, X. D.; Jin, S. B.; Zhang, C. Q.; Yang, K. N.; Huo, S. D.; Chen, F.; Zou, G. Z.; Liang, X. J., Probe-inspired nano-prodrug with dual-color fluorogenic property reveals spatiotemporal drug release in living cells. *ACS Nano* **2015**, *9*, 2729-2739.

270. Maruani, A.; Smith, M. E. B.; Miranda, E.; Chester, K. A.; Chudasama, V.; Caddick, S., A plug-and-play approach to antibody-based therapeutics via a chemoselective dual click strategy. *Nat. Commun.* **2015**, *6*.

271. Boutureira, O.; Bernardes, G. J. L., Advances in chemical protein modification. *Chem. Rev.* **2015**, *115*, 2174-2195.

272. Santos, F. M. F.; Matos, A. I.; Ventura, A. E.; Goncalves, J.; Veiros, L. F.; Florindo, H. F.; Gois, P. M. P., Modular assembly of reversible multivalent cancer-cell-targeting drug conjugates. *Angew. Chem. Int. Ed.* **2017**, *56*, 9346-9350.

273. Santos, F. M. F.; Rosa, J. N.; Candeias, N. R.; Carvalho, C. P.; Matos, A. I.; Ventura, A. E.; Florindo, H. F.; Silva, L. C.; Pischel, U.; Gois, P. M. P., A three-component assembly promoted by boronic acids delivers a modular fluorophore platform (BASHY dyes). *Chem-Eur. J.* **2016**, *22*, 1631-1637.

274. Piffoux, M.; Silva, A. K. A.; Wilhelm, C.; Gazeau, F.; Tareste, D., Modification of extracellular vesicles by fusion with liposomes for the design of personalized biogenic drug delivery systems. *ACS Nano* **2018**, *12*, 6830-6842.

275. Srinivasarao, M.; Low, P. S., Ligand-targeted drug delivery. *Chem. Rev.* **2017**, *117*, 12133-12164.

276. Habibi, N.; Kamaly, N.; Memic, A.; Shafiee, H., Self-assembled peptide-based nanostructures: Smart nanomaterials toward targeted drug delivery. *Nano Today* **2016**, *11*, 41-60.

277. Xue, L.; Yu, Q. L. Y.; Griss, R.; Schena, A.; Johnsson, K., Bioluminescent antibodies for point-of-care diagnostics. *Angew. Chem. Int. Ed.* **2017**, *56* (25), 7112-7116.

278. Scarabelli, S.; Tan, K. T.; Griss, R.; Hovius, R.; D'Alessandro, P. L.; Vorherr, T.; Johnsson, K., Evaluating cellular drug uptake with fluorescent sensor proteins. *ACS Sensors* **2017**, *2*, 1191-1197.

279. Kalderon, D.; Roberts, B. L.; Richardson, W. D.; Smith, A. E., A short amino-acid sequence able to specify nuclear location. *Cell* **1984**, *39*, 499-509.

280. Xu, D. D.; Wegner, S. V., Multifunctional streptavidin-biotin conjugates with precise stoichiometries. *Chem. Sci.* **2020**, *11*, 4422-4429.

281. Eguchi, A.; Furusawa, H.; Yamamoto, A.; Akuta, T.; Hasegawa, M.; Okahata, Y.; Nakanishi, M., Optimization of nuclear localization signal for nuclear transport of DNA-encapsulating particles. *J. Control. Release.* **2005**, *104*, 507-519.

282. Pommier, Y.; Leo, E.; Zhang, H. L.; Marchand, C., DNA Topoisomerases and their poisoning by anticancer and antibacterial drugs. *Chem. Biol.* **2010**, *17*, 421-433.